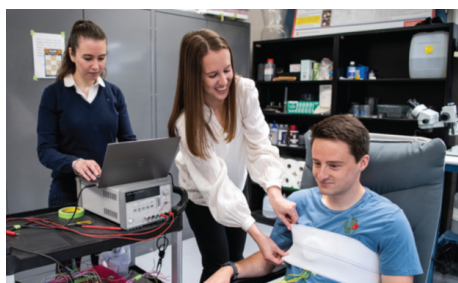
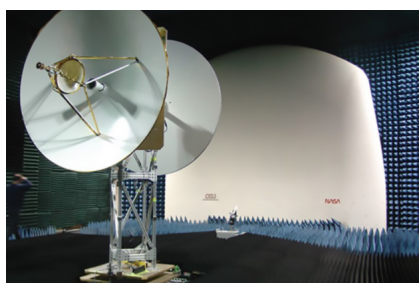


# 2022 Project Report

## ElectroScience Laboratory

Consortium on Electromagnetics and Radio Frequencies



THE OHIO STATE UNIVERSITY

# Quantum Microwave Photonics

A Final Report for the Consortium on Electromagnetics and Radio Frequencies (CERF)

Submitted by David W. Nippa, Ph.D., [nippa.2@osu.edu](mailto:nippa.2@osu.edu)

## Introduction

The goal of this effort is to pursue research that exploits recent advances in quantum technologies in the context of engineering problems that are relevant to OSU's ElectroScience Laboratory. In recent decades, quantum entanglement [1, 2] has been applied to advance fields such as secure telecommunications, high speed computing and metrology. Entangled particle sources are fundamental building blocks for realizing quantum memories, quantum key distribution and groundbreaking experiments [3]. Engineering researchers have not historically applied quantum entanglement in their work due, in-part, to the need for multi-disciplinary skills in quantum mechanics, photonics and RF technologies. Fortunately, such capabilities and experience exist today at ESL. For example, ESL researchers are skilled in applying quantum mechanics in the areas of spectroscopy and chemical sensing [4, 5]. One research group is developing computer simulation techniques that exploit existing commercial software tools to make the investigation of quantum phenomena more accessible to engineers and scientists [6]. In addition, quantum technologies often exploit planar lightwave circuits and operating wavelengths common to the telecommunications industry as well as the field of microwave photonics [7]. In particular, lithium niobate, a workhorse for high-speed optical modulation, is used to generate entangled photons at optical wavelengths near 1550 nm by exploiting the non-linear phenomena of spontaneous parametric down-conversion (SPDC) [3, 8]. Researchers at ESL have created devices that exploit the non-linear properties of lithium niobate [9] and have fabricated packaged devices, with optical fiber connectivity, specifically designed to be entangled photon sources for other research groups [10, 11]. These capabilities and experiences can be harnessed and focused on solving problems that exploit quantum phenomena for application areas that are relevant to ESL's research initiatives.

## Background

The hardware needed to perform quantum photonic experiments provides the ability to detect the individual photons and know, within a high probability, that they were formed at the same time. Figure 1 shows ESL's quantum photonic testbed with the fundamental components for such an experiment. A tunable laser source operating at visible wavelengths provides a pump source. Wavelength tunability allows the pump wavelength to match the operating wavelength of the device under test (DUT). Because the DUT is polarization sensitive and the lensed fiber is single-mode, a polarization controller needs to be located before the DUT. A bandpass filter is placed after the DUT to remove the pump wavelength. The 1550 nm light encounters a non-polarizing 50-50 fiber optic splitter and is then directed to a single-photon avalanche diode (SPAD). In one scenario, one SPAD runs in free-running mode, and the other detector runs in gated mode. The free-running SPAD detects the heralding photon (or signal) and triggers the

gated SPC to observe photons at a specified time and time window using a time controller. The optical path length prior to the gated detector is extended by a known time-delay. When a photon is detected by the gated SPAD, the probability of it being the photon pair caused by SPDC is much higher than the detection coming from a dark-count or a random photon detection event.

The quantum photonic testbed, shown in Figure 2, also includes an entangled photon source (EPS) procured from a commercial vendor. This SPDC device can serve as the DUT and it includes the polarization control and band-pass filter.

## Project Progress

With CERF funding we employed Mr. Ben Hughes, an undergraduate physics major, to learn about quantum photonics, how to operate the testbed equipment, and to perform fundamental experiments using the commercial EPS. The following research activities were performed:

- Developed software to interface with lab devices,
- Conducted measurements using the SPADs,
- Measured the output power of the EPS with respect to input power (Figure 3).
- Performed photon counting experiments (photon statistics) (Figure 4).
- Performed coincidence counting experiments (Figure 5), and
- Performed quantum tomography for the 1 and 2 qubit case with the EPS.

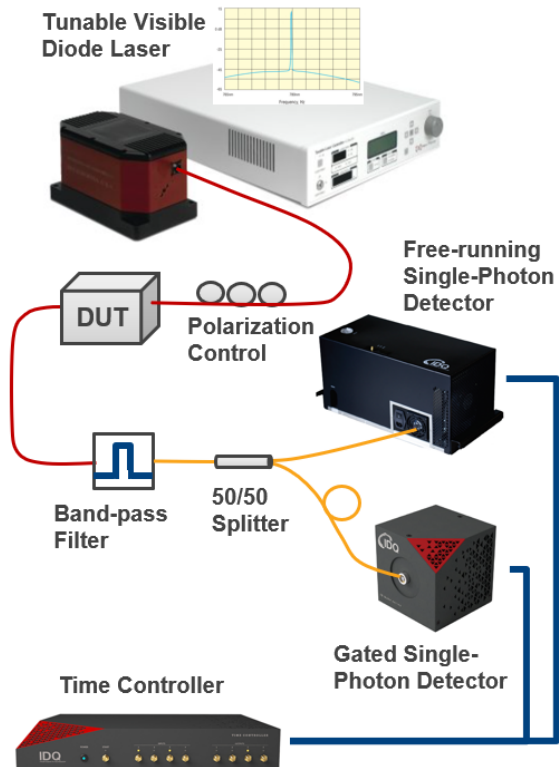


**Figure 1. Experimental setup and hardware procured for the characterization of entangled photons emanating from the device under test (DUT).**

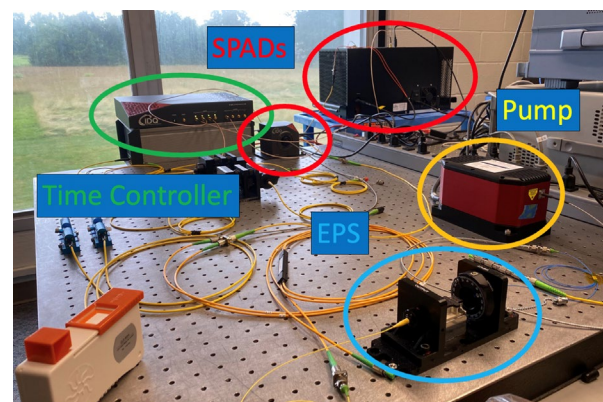


**Figure 2. Quantum photonic testbed with commercial EPS.**

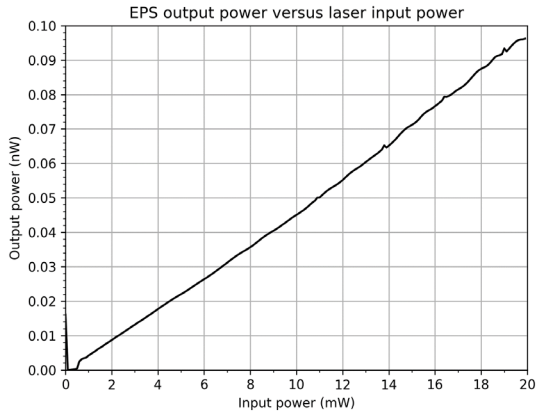


**Figure 3. Power response of commercial EPS.**

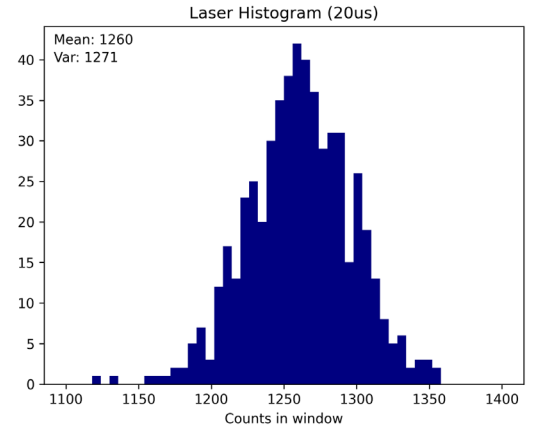


**Figure 4. Photon statistics of 1550 nm laser.**

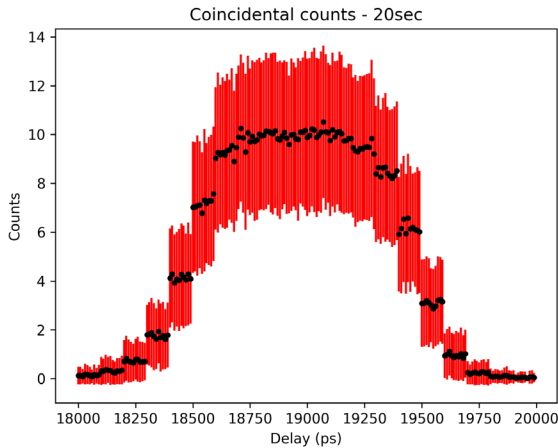


**Figure 5. Coincidence counts of photon pairs at 1550 nm using the commercial EPS.**

Prof. Ron Reano's research group used the quantum photonics testbed to characterize a photonic device they fabricated to generate entangled photons. Their EPS is formed in lithium niobate on insulator (LNOI) doped with magnesium oxide (MgO) [11]. The MgO doping reduces the poling voltage as well as reduces optical absorption and optical damage. Guiding is facilitated by a silicon nitride (SiN) strip on the surface of the LNOI. Phase matching of the pump with the idler and signal photons is provided through periodically poling the lithium niobate (PPLN). This device was originally designed to perform wavelength conversion with an infrared (near 1550 nm) pump to create the second harmonic (near 775 nm) using the phenomena of second harmonic generation (SHG). So, two 1550 nm photons combine to form a single 775 nm photon. However,



the process can be reversed using a 775 nm input (as the pump photon) to form the 1550 nm photon pairs (as the signal and idler photons). This reversal is SPDC. This device exhibits Type-O SPDC since the polarization of the pump is the same as the signal and idler photons.

## Conclusions

This effort has allowed ESL to grow capabilities in quantum photonics but there is much work yet to be done. This work will continue with progressively increased complexity to gain proficiency in performing quantum measurements. By developing this seed effort, we can plan for future research, continue to provide hands-on experience to future quantum engineers, and pursue external funding in this exciting area of study.

## Bibliography

- [1] Einstein, Albert, Boris Podolsky, and Nathan Rosen. "Can quantum-mechanical description of physical reality be considered complete?" *Physical review* 47, no. 10 (1935): 777.
- [2] Bell, John S. "On the Einstein Podolsky Rosen paradox." *Physics Physique Fizika* 1, no. 3 (1964): 195.
- [3] Alibart, Olivier, Virginia D'Auria, Marc De Micheli, Florent Doutre, Florian Kaiser, Laurent Labonté, Tommaso Lunghi, Éric Picholle, and Sébastien Tanzilli. "Quantum photonics at telecom wavelengths based on lithium niobate waveguides." *Journal of Optics* 18, no. 10 (2016): 104001.
- [4] Neese, Christopher F., Ivan R. Medvedev, Grant M. Plummer, Aaron J. Frank, Christopher D. Ball, and Frank C. De Lucia. "Compact submillimeter/terahertz gas sensor with efficient gas collection, preconcentration, and ppt sensitivity." *IEEE Sensors Journal* 12, no. 8 (2012): 2565-2574.
- [5] Ball, Christopher D., and Frank C. De Lucia. "Direct measurement of rotationally inelastic cross sections at astrophysical and quantum collisional temperatures." *Physical review letters* 81, no. 2 (1998): 305.
- [6] Na, Dong-Yeop, Jie Zhu, Weng C. Chew, and Fernando L. Teixeira. "Quantum information preserving computational electromagnetics." *Physical Review A* 102, no. 1 (2020): 013711.
- [7] Urick, Vincent Jude, Keith J. Williams, and Jason D. McKinney. *Fundamentals of microwave photonics*. John Wiley & Sons, 2015.
- [8] Saleh, Bahaa EA, and Malvin Carl Teich. *Fundamentals of photonics*. John Wiley & Sons, 2019.
- [9] Nagy, Jonathan Tyler, and Ronald M. Reano. "Reducing leakage current during periodic poling of ion-sliced x-cut MgO doped lithium niobate thin films." *Optical Materials Express* 9, no. 7 (2019): 3146-3155.

[10] Saglamyurek, Erhan, Marcelli Grima Puigibert, Qiang Zhou, Lambert Giner, Francesco Marsili, Varun B. Verma, Sae Woo Nam, Lee Oesterling, David Nippa, et al. "A multiplexed light-matter interface for fibre-based quantum networks." *Nature communications* 7 (2016): 11202.

[11] Oesterling, Lee, Fernando Monteiro, Sean Krupa, David Nippa, Richard Wolterman, Donald Hayford, Eric Stinaff, Bruno Sanguinetti, Hugo Zbinden, and Rob Thew. "Development of photon pair sources using periodically poled lithium niobate waveguide technology and fiber optic components." *Journal of modern optics* 62, no. 20 (2015): 1722-1731.

## CERF Project 2022 Report

### Sensing Bio-Magnetic Fields in Non-Shielded Environments

PI: Asimina Kiourti

#### Project Overview

Currents flow naturally through the human body generating magnetic fields. Sensing these bio-magnetic fields is of utmost significance for the diagnosis and treatment of diverse conditions related to the heart, nervous system, brain, and beyond. However, clinical practices in this regard are extremely limited, mainly due to the lack of adequate sensing technologies. Specifically, these naturally emanated bio-magnetic fields are much weaker than the Earth's magnetic field, necessitating shielded rooms and expensive superconductor-based devices to be retrieved. To overcome limitations in the state-of-the-art, we recently reported new classes of low-cost and unshielded sensors that rely on miniature coil arrays to sense the magnetic fields of the heart. A major limitation, however, is that the heart generates the strongest magnetic field from across the human body ( $\sim 100$  pT), implying that our sensor does not have the sensitivity suitable to detect other magnetic fields, such as those generated by compound action potentials or the brain (down to  $\sim 100$  fT). This project aims to explore the feasibility of improving our sensor's sensitivity via advances in hardware and digital signal processing.

#### Main results

We previously reported a fully-passive, miniaturized and light-weight sensor that can detect magnetocardiography (MCG) signals in non-shielded environments, as validated upon phantoms. The sensor operates on the principle of Faraday's law where alternating magnetic flux from the heart interacts with induction coils placed upon the chest to induce voltages upon them. Through theoretical optimization of the coil geometry and advanced digital signal process (DSP), the final MCG signal can be retrieved in earth ambient field. However, three limitations of our prior work are that (a) the MCG sensor relies on extensive averaging over a long period of time (i.e., 15 minutes) that may be unsuitable for certain clinical applications, (b) the MCG sensor only operates in the presence of an ECG sensor (or equivalent) that is used to identify the cardiac cycles for averaging, and (c) performance has only been validated *in vitro* using a function generator and an 8-shaped loop to emulate MCG activity.

In a major step forward, we herewith expanded upon our previous work to demonstrate (a) monitoring of the full spectrum of MCG activity with: i. clear R-peaks in real-time and ii. clear P, T, QRS, and U waves over  $\sim 4.5$  minutes of averaging, (b) stand-alone operation of the MCG sensor without the need for an accompanying ECG sensor, and (c) *in vivo* validation on human subjects. In brief, seven (7) coil sensors were integrated into a coil array and their signals were averaged in real-time and post-processed via advanced Digital Signal Processing (DSP) to generate a single MCG plot, Figure 1. As a proof-of-concept, we recruited 11 healthy subjects (36% female and 64% male) and recorded MCG and ECG activity using our MCG sensor and a commercial 3-lead ECG system, respectively. The latter was used as a gold-standard to evaluate the MCG sensor's detection accuracy and is not required for the MCG sensor to detect the full MCG spectrum. Experiments were carried out under two scenarios, viz. no body movement and minimal body movement, to assess the sensor's tolerance to subject movement.

Our results confirmed that real-time MCG can be retrieved with clear R-peaks that are synchronized with gold-standard ECG peaks in earth ambient noise for the entire test duration ( $\sim 5$  minutes), Figure 2. With averaging over 313 cycles or  $\sim 4.5$  minutes using the MCG-derived R-peaks as trigger, P, T, QRS, and U waves can all be clearly identified. Repeatability tests confirm that our sensor's performance is robust within and

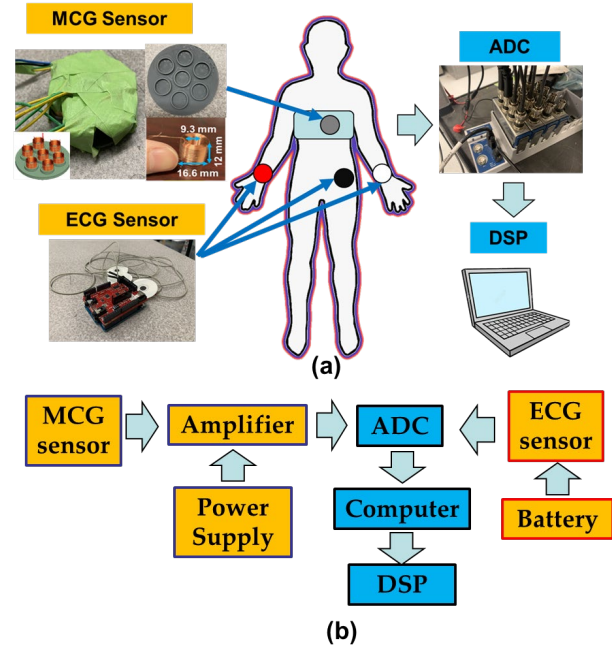


Fig. 1. (a) Overview of the recording system. (b) Block diagram of the sensor and electronics connections.

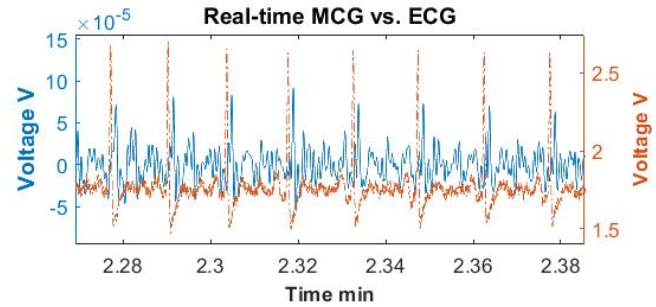


Fig. 2. Validation test: Real-time MCG (blue solid line) vs. ECG (red dash line) in earth ambient noise.

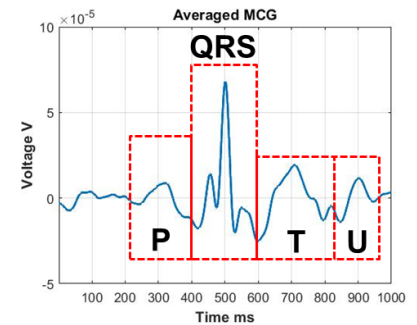


Fig. 3. Validation test: Cycle-averaged MCG over  $\sim 4.5$  minutes.

across subjects with similar detection accuracy as the gold-standard ECG, and tolerant to body movements.

### **Publications**

K. Zhu and A. Kiourti, "Real-Time MagnetoCardiography with Passive Miniaturized Coil Array in Earth Ambient Field," *IEEE Transactions on Biomedical Engineering*. [under review]

# Electromagnetic Tomography Imaging with Explicit Uncertainty Estimates

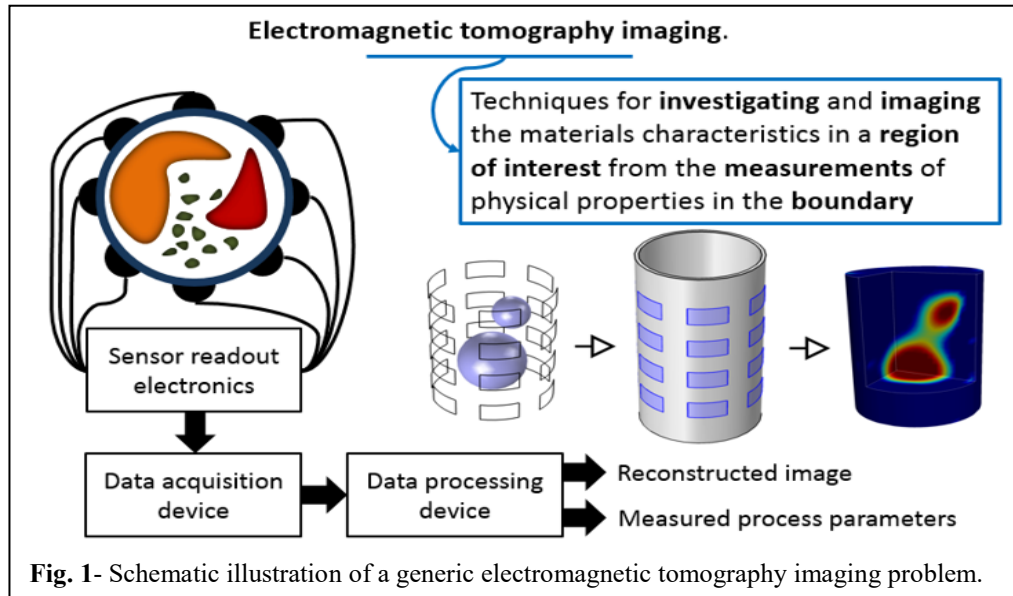
## CERF Project Report

PI: Fernando L. Teixeira

**Abstract:** In this research effort, we developed a new electromagnetic tomography imaging reconstruction algorithms based on a probabilistic Bayesian methodology that provides explicit uncertainty estimates about the reconstructed images. The approach leverages the Relevance Vector Machine (RVM) framework to efficiently obtain image reconstruction and uncertainty level estimates from explicit analytical formulas based on successive minimization updates of the differential entropy of the image vector. The proposed formulation has the following beneficial features: (i) explicitly incorporate prior information about the problem, (ii) explicitly insert randomness/uncertainty source (such as measurement noise) models, (iii) incorporates its own regularization mechanisms, and (iv) yield performance criteria about uncertainty estimates or information content.

### 1. Introduction and Motivation

The general problem of image reconstruction in electromagnetic tomography (see Fig. 1) has several challenges. One key challenge is that it constitutes a nonlinear and ill-posed inverse problem [Tar05, Stu10]. A salient feature of ill-posed inverse problems is the fact that they do not have a unique solution. For example, in the case of microwave tomography or capacitance tomography, this means that the reconstruction of the permittivity and conductivity distributions in the region of interest (RoI) is a severely underdetermined problem: the amount of information provided by the set of measurements is insufficient to effectively and completely describe the unknown permittivity/conductivity distributions in the RoI. In addition



to this, inverse problems are ill-conditioned, which translates into the solution being highly sensitive to noise in practice.

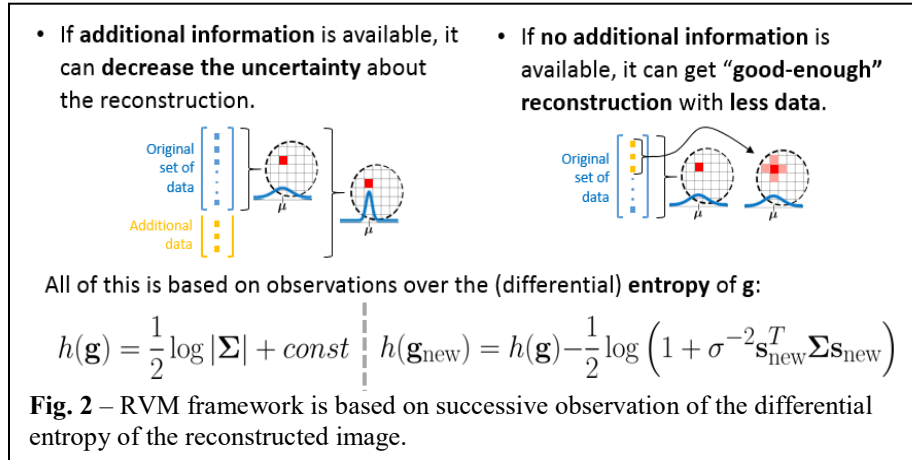


In addition to conventional regularization techniques, an effective way to address an ill-posed inverse problem is to re-formulate it as an inference or an estimation problem with a probabilistic description. This probabilistic or *Bayesian* formulation [Fou14, Roc18, Sal19] (i) allows to explicitly incorporate prior information about the problem, (ii) provides ways to explicitly insert randomness/uncertainty source (such as measurement noise) models, (iii) incorporates its own regularization mechanisms, and (iv) *directly offers the possibility of obtaining performance criteria about uncertainty estimates or information content*. Most of previous approaches have focused on capturing the right structure of the particular problem through a prior distribution modeling and/or the image reconstruction from the resulting posterior distribution, usually via Markov chain Monte Carlo methods or Monte Carlo integration procedures [Gir10]. A few of these works perform uncertainty quantification for the reconstructed image (posterior distribution); however, the need to address uncertainty in the image reconstruction process and its relationship to a pixel-based image reconstruction has not been addressed in the past.

## 2. Technical approach

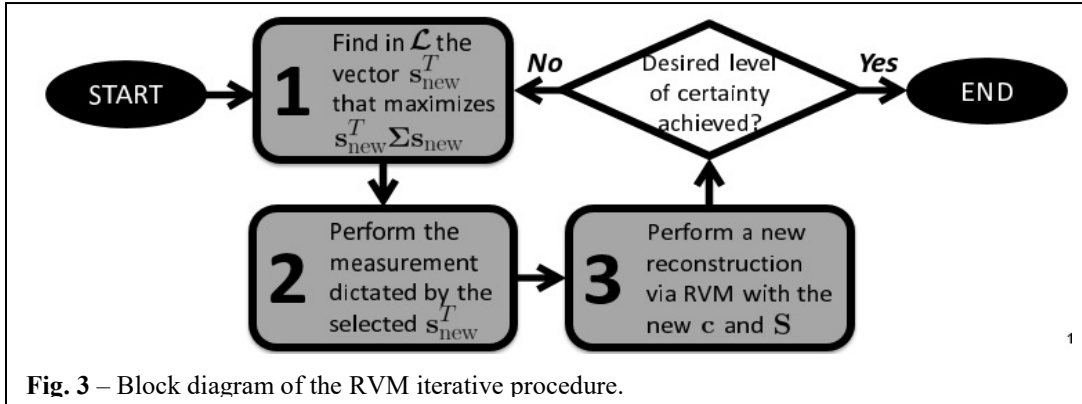
The ability to efficiently obtain uncertainty estimates about the reconstructed images is of great practical value in assessing the quality of any electromagnetic tomography imaging algorithm. Additionally, these estimates may serve as a starting point for developing adaptive measurement strategies to decrease the uncertainty through additional, sequential measurements. In this research effort, we have developed a new electromagnetic tomography imaging reconstruction algorithms with a Bayesian methodology that provides explicit uncertainty estimates about the obtained images.

The technical approach leverages the Relevance Vector Machine (RVM) framework [Tip01] to perform uncertainty analysis of the estimated image pixel or voxel values from the variance of the reconstructed images. Instead of relying on averaging several



samples of the posterior distribution (which represent the reconstructed images), the RVM framework allows us to efficiently obtain image reconstruction and uncertainty level estimates from explicit analytical formulas. In brief, the RVM is based on successive minimization updates on the differential entropy  $h$  of the image vector  $\mathbf{g}$  (treated as a probability distribution), as illustrated in Fig. 2. Minimization of the entropy is obtained by maximization of the argument of the log factor in Fig. 2 where the vector  $\mathbf{s}_{\text{new}}$  is comes from the information provided by a

new measurement and  $\Sigma$  is the covariance matrix, which provides the uncertainty estimate. The resulting iterative procedure is illustrated in Fig. 3. In this figure,  $\mathbf{c}$  represents the measurement vector,  $\mathbf{S}$  is the sensitivity matrix (that represent the forward model of the problem) and  $\mathcal{L}$  is a dictionary of a small number of initial measurements upon which new sequential measurements are added in an adaptive fashion by the RVM process.



### 3. Results

In this section we present the application of the Reduced ARVM applied to three different scenarios involving an adaptive electrical capacitance volume tomography (AECVT) sensor. These scenarios comprise flow types typically encountered in industrial practice: two bubbly flows and one columnar flow, as illustrated Fig. 4. In all cases, the AECVT sensor is placed around a cylindrical plastic pipe of thickness 2 mm. The AECVT sensor is composed of 192 electrode segments arranged in a  $8 \times 24$  configuration, and has a height of 75 mm. The vertical gap between adjacent electrode segments is 1/2 the height of each electrode segment, and the horizontal gap is 1/2.5 the arclength of each electrode segment. For the scanning process, the electrode segments are excited with a time-harmonic voltage signal of 1 MHz.

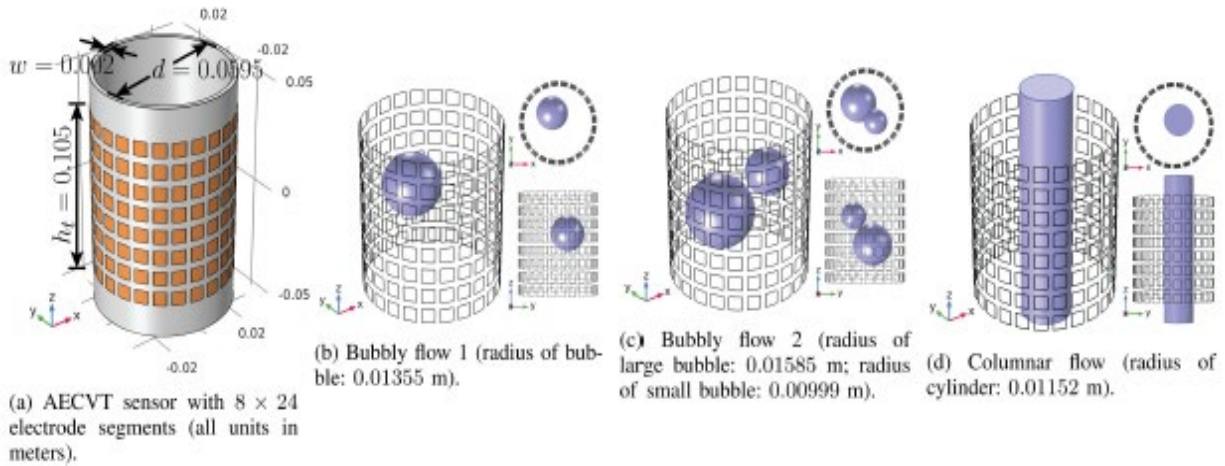


**Fig. 4.** AECVT sensor geometry and flow types considered.

Fig. 5 presents image reconstruction results and corresponding standard deviation plots obtained by AECVT sensors based on the traditional RVM method (employing all available measurements) and the Reduced ARVM method with a smaller percentage of measurements. The reconstruction and standard deviation estimates are obtained through RVM after the last measurement-insertion step. The number of measurements in each case is indicated in the captions of Fig. 5(g)–(i). The Reduced ARVM process in these cases is initiated from an initial set of 276 measurements. This initial set of measurements corresponds to all the measurements from the largest synthetic electrodes (i.e.,  $4 \times 6$ ) considered here. The results in Fig. 5 show good reconstruction performance both from RVM with all available measurements and from the Reduced ARVM with fewer measurements [see Fig. 5(a)–(c) and (g) and (i)]. The image reconstruction results from the Reduced ARVM method are very similar to those from RVM, despite the fact that they are obtained with significantly fewer measurements. This clearly demonstrates that good image reconstruction performance can be obtained with a reduced set of measurements if the latter are properly selected.

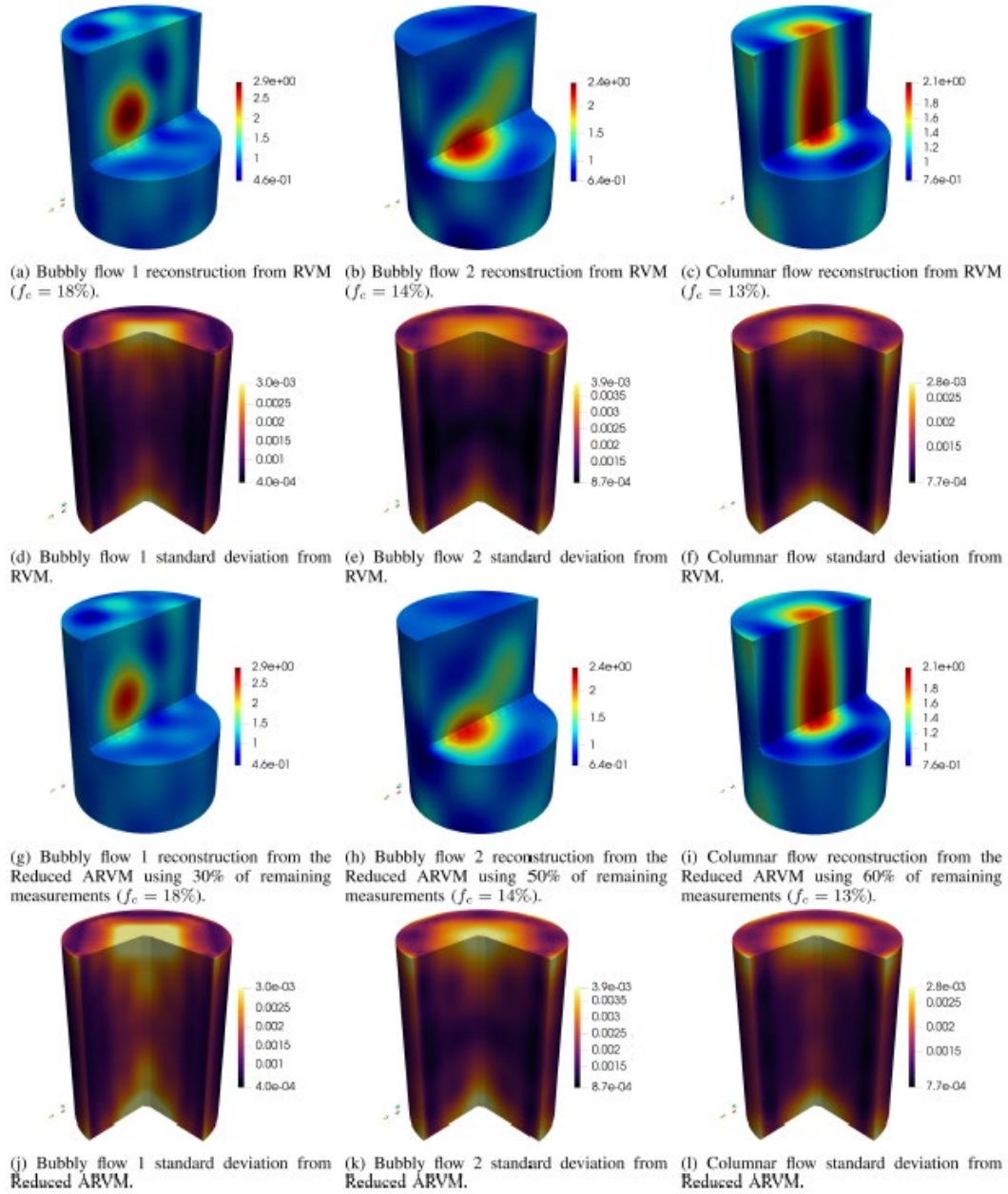


**Fig. 5.** Traditional RVM (considering all available measurements) and Reduced ARVM results for the scenarios shown in Fig. 4.

## 5. References cited

- [Tar05] A. Tarantola, *Inverse Problem Theory and Methods for Model Parameter Estimation*, vol. 89, SIAM Press, 2005.
- [Stu10] A. M. Stuart, "Inverse problems: A Bayesian perspective," *Acta Numerica*, vol. 19, pp. 451–559, 05 2010.
- [Fou14] A. E. Fouda and F. L. Teixeira, "Bayesian compressive sensing for ultrawideband inverse scattering in random media," *Inverse Problems*, vol. 30, no. 11, 114017, 2014.
- [Roc18] P. Rocca, G. Gottardi, M. Bertolli, F. Robol, T. Moriyama, and T. Takenaka, "Processing GPR data with 2d Bayesian compressive sensing inverse scattering approaches," *Journal of Physics: Conference Series*, vol. 1131, 012006, 2018.

## CERF: Electromagnetic Tomography Imaging with Explicit Uncertainty Estimates

- [Sal19] M. Salucci, L. Poli, and G. Oliveri, “Full-vectorial 3D microwave imaging of sparse scatterers through a multi-task Bayesian compressive sensing approach,” *Journal of Imaging*, vol. 5, no. 1, 2019.
- [Gha14] L. Gharsalli, H. Ayasso, B. Duchêne, and A. Mohammad-Djafari, “Inverse scattering in a Bayesian framework: application to microwave imaging for breast cancer detection,” *Inverse Problems*, vol. 30, no. 11, p. 114011, 2014.
- [Gir10] F. Giraud, P. Minvielle, and P. D. Moral, “Advanced interacting sequential Monte Carlo sampling for inverse scattering,” *Inverse Problems*, vol. 29, no. 9, 095014, 2013.
- [Tip01] M. E. Tipping, “Sparse bayesian learning and the relevance vector machine,” *Journal of Machine Learning Research*, vol. 1, pp. 211–244, Sept. 2001.

## Measurement of single photon coincidence events from lithium niobate on insulator optical waveguides

Karan Prabhakar, PhD Graduate Student

Ronald M. Reano, Professor

reano.1@osu.edu

### Abstract

The objective of this research is measure single photon coincidence events from chip-scale heralded single photon source on lithium niobate on insulator (LNOI) platform. The ability to measure single photon coincidence events is important for a variety of protocols in quantum information science and technology (QIST). QIST involves harnessing the superposition and entanglement of quantum mechanical objects, such as photons, for applications that include quantum computing, sensing, communications, and metrology. Photons are particularly efficient carriers of quantum information because they travel at the speed of light, interact weakly with their environment over long distances, and can be manipulated with linear and nonlinear optics. In our research project, we focus on the measurement of single photon coincidence events from a commercial entangled photon pair source at the ElectroScience Laboratory (ESL) and make progress towards low loss LNOI waveguides which can be used as single photon sources that rely on spontaneous parametric down conversion (SPDC).

### A. Project Description

Single photon sources can be fabricated using lithium niobate which is a nonlinear optical material. Optical nonlinearity can give rise to spontaneous parametric down conversion (SPDC) which is noticeable at high pump powers. During SPDC, a pump photon is down converted to two signal photons of lower energies, also referred to as the signal photon. The two down converted photons are said to constitute an entangled photon pair. An efficient SPDC process requires phase matching between the pump and the signal photons, along with a high field overlap between the participating photons. We conduct coincidental counts measurements of down conversion using a commercially available periodically poled lithium niobate device from OZ Optics. We also develop low loss LNOI waveguides as a platform of our choice due to the high optical nonlinearity of LN and large field overlaps obtained by design of the waveguide cross-section. Mode field diameters, on the order of  $1\text{ }\mu\text{m}$ , in the fabricated devices allow high optical intensities to be achieved with low input powers while allowing phase matching via poling using patterned metal electrodes.

### B. Project Results

We have conducted fabrication of low loss lithium niobate waveguide devices which can find use in future single photon sources that rely on SPDC. Losses down to 0.14 dB/cm have been measured on these waveguides [1]. We have also conducted coincidental counts measurements of down converted photons using a commercially available periodically poled lithium niobate device from OZ Optics. Details of device operation can be found in [2].

To conduct the coincidental counts measurement, the measurement setup shown in Fig. 1 was used. At the output, a wavelength division multiplexer (WDM) is utilized to reject the pump and transmit down converted photons at infrared wavelengths to a single photon detector (SPD). The output from the WDM



is then sent to a Y-splitter which routes the entangled photons to two single photon detectors (SPDs). For one of the SPDs, the output is delayed with the use of excess fiber. The excess fiber length is 13 meters resulting in a delay of about 63 ns. The delayed SPD is operated in gated mode, while the other SPD is operated in free running mode. The SPDs are connected to a digital time controller which precisely measures the arrival times of the photons. The free running SPD produces a gating pulse which is fed to the gated SPD. The measurement setup is shown in Fig. 1.

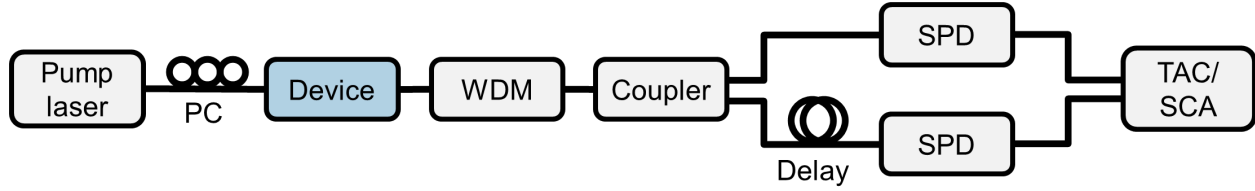


Figure 1. Measurement setup to measure pair generation rate. b) Measurement setup to measure heralding rate. SPD: single photon detector, TAC: time to amplitude converter, SCA: Single channel analyzer.

Using this setup, the device was pumped with 773 nm pump light from a continuous wave laser. Data from the time controller is set to a PC for analysis. The result of the coincidence counts measurement is shown in Fig. 2. A coincidence between the arrival times of the photons occurs at 63 ns, consistent with the applied excess optical delay in the measurement setup. The laser power was maintained at 10 mW and data was collected for 30 minutes. Four coincidences per second were observed for a total of 7178 coincidental counts in 30 minutes.

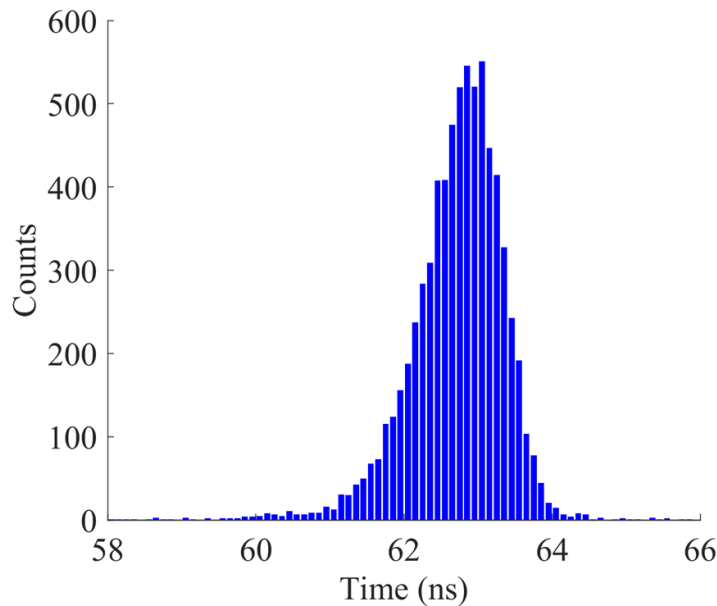
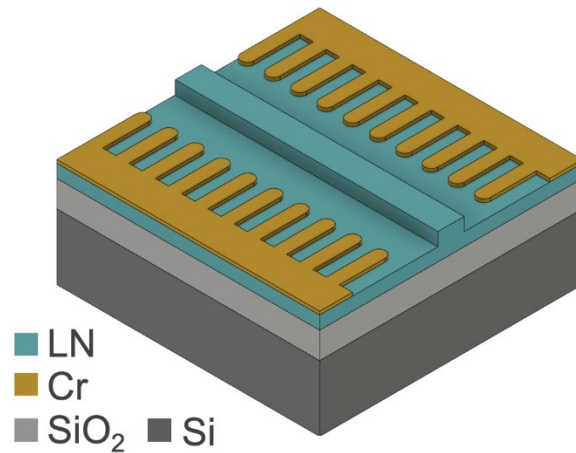


Figure 2. a) Measured coincidence counts. A delay of 63 ns was observed since a fiber excess length of 13 m was used to delay the gated SPD.

Progress towards the fabrication of low-loss LN rib structures has also been made. Etched rib structures on LN with smooth sidewall surfaces can lead to higher SPDC efficiencies and lower loss. To fabricate LN rib waveguides, we have employed plasma etching and a high temperature resist reflow method [1]. The proposed device structure with an etched LN rib is shown in Fig. 3. This device is proposed on LNOI on a Si handle substrate.



*Figure 3. Device structure with etched LN rib and chromium poling electrodes.*

Results of the process optimization are shown in the SEM images in Fig. 4. The optimized process can produce rib waveguides with smooth sidewalls which will be employed for the fabrication of an optimized heralded single photon source.

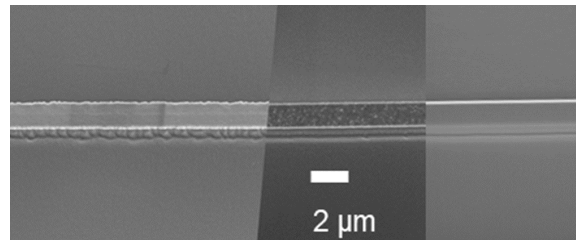


*Figure 4. Optimization and control of fabrication process to obtain smooth etched LN ribs.*

Future fabrication steps include definition of chromium electrodes and high voltage ferroelectric domain inversion to pole the LN thin film followed by optical characterization of (degenerate) photon pair generation rate and photon heralding efficiencies.

## References

- [1] K. Prabhakar and R. M. Reano, "Fabrication of Low Loss Lithium Niobate Rib Waveguides Through Photoresist Reflow," in *IEEE Photonics Journal*, vol. 14, no. 6, pp. 1-8, Dec. 2022, Art no. 6660808, doi: 10.1109/JPHOT.2022.3222184.
- [2] R. Horn and T. Jennewein, "Auto-balancing and robust interferometer designs for polarization entangled photon sources," *Opt. Express*, OE, vol. 27, no. 12, pp. 17369–17376, Jun. 2019, doi: 10.1364/OE.27.017369.

# Development of a VHF to C-band Reprogrammable Radiometer (VCRRAD)

Personnel: Mark Andrews (PI) and Shane Smith

## Abstract

Radiometry is typically performed in narrow portions of the spectrum protected from radio transmissions. This is done in order to have low levels of radio frequency interference (RFI) and ensure the accuracy of radiometric measurements. The ElectroScience Laboratory (ESL) is a leading figure in the development of algorithms that can detect the presence of RFI in radiometric data, enabling opportunistic operation in unprotected bandwidths and the creation of wideband radiometers. The VHF to C-band Reprogrammable Radiometer (VCRRAD) aims to extend the wideband radiometry developed at ESL to be operable with a commercially available software defined radio (SDR) backend while being small enough to be mounted on an unmanned aerial vehicle (UAV, or drone) platform. This report summarizes the design of VCRRAD, as well as the production and testing status of the hardware.

## Introduction

VCRRAD is a radiometer frontend designed to operate from 70 MHz – 6 GHz, matching the input bandwidth of an Ettus embedded software defined radio (E310/E312/E320). Combining VCRRAD with this SDR will result in a portable and adaptable radiometer design suitable for use on platforms as small as commercially available drones. Radiometric measurements at these frequencies can be used in remote sensing, biosensing, spectrum analysis, and other fields. Using a software defined radio as the backend of the radiometer allows for the instrument to measure any frequency desired and to perform RFI mitigation if needed as well. The adaptability of the design allows for fast and inexpensive experiments to be conducted for new or changing mission requirements, and enable this technology to reach wider audiences and applications.

## Design

A key challenge facing wideband radiometers is the calibration problem presented by poorly matched components. In narrowband applications, component return losses of  $< -30$  dB can be achieved, allowing radiometer operation to ignore multiple reflections within a system. However, wideband operation often requires accepting return losses of up to  $-10$  dB, which can result in interference patterns visible in the calibrated data. The VCRRAD architecture is designed to address this issue by enabling up to 8 targets (7 for calibration) to be viewed through an 8:1 switch network, as well as having an injectable coupled external calibration

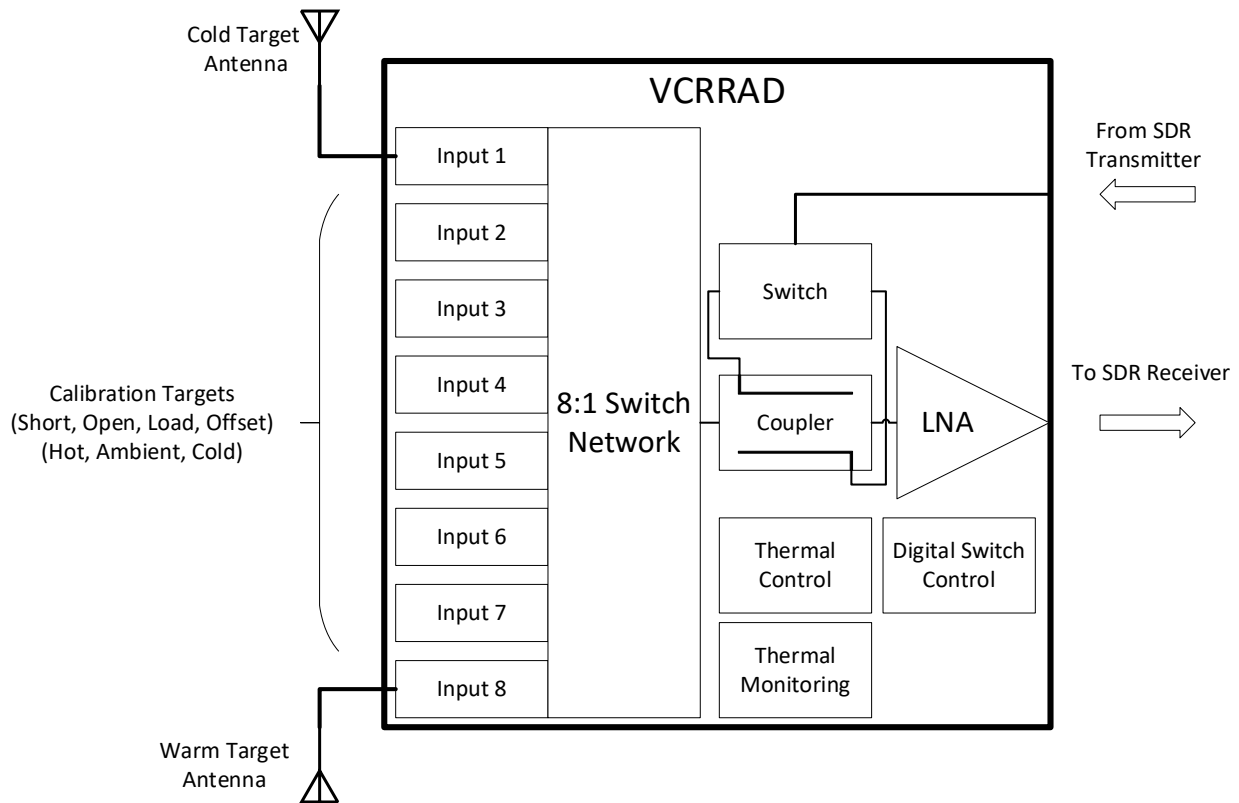


Figure 1: VCRRAD Block Diagram

signal to characterize the input impedance of the system and antenna. A block diagram of the system is in Figure 1.

VCRRAD is designed to operate over the entire spectrum available to the Ettus E320 Universal Software Radio Peripheral (USRP) SDR. The E320 operates from 70 MHz to 6 GHz, with an 8 dB noise figure. VCRRAD must be a PCB design so that it can be a lightweight and low power instrument used in conjunction with the E320 in a drone-mounted application. The E320 has limited functionality in its ability to control a peripheral. Eight general purpose input/output pins are available on the mini-HDMI port and must be capable of controlling the radiometer states and thermistor multiplexing. Key specifications of the E320 and design parameters for VCRRAD are summarized in Tables 1 and 2 respectively.

Table 1: Key E320 Specifications

<b><u>Parameter</u></b>	<b><u>Specification</u></b>
Frequency Range	70 MHz - 6 GHz
Instantaneous Bandwidth	56 MHz
Noise Figure	< 8 dB
Dimensions	175 x 106 x 38 mm
Weight	.86 kg
Power Consumption	12V, up to 7.5 A
Interfaces	SMA - 2 RX, 2 TX USB - 5V, 500 mA Mini-HDMI - 3V 500 mA, 8 GPIO pins

Table 2: Target VCRRAD Requirements

<b><u>Parameter</u></b>	<b><u>Specification</u></b>
Gain	25 dB at 6 GHz
Noise Figure	4 dB at 6 GHz
Dimensions	< 175 x 106 mm area
PCB layers	6
Power Consumption	5V < 500 mA 3V < 500 mA
Interfaces	8 SMA target ports 1 SMA calibration signal port 8 GPIO pins to control and monitor system

## Schematic Design

The system design can be split into four primary subsystems: the input network, the output amplifier, the digital control subsystem, and the thermal subsystem. The input network design is fairly straightforward and is pictured in Figure 2. The design is based on the Mini-Circuits JSW2-63DR+ RF switch. Seven switches are arranged in an 8:1 multiplexer arrangement to allow for a single RF channel to be observed. The output of the multiplexer network becomes the input to the output amplifier subsystem.

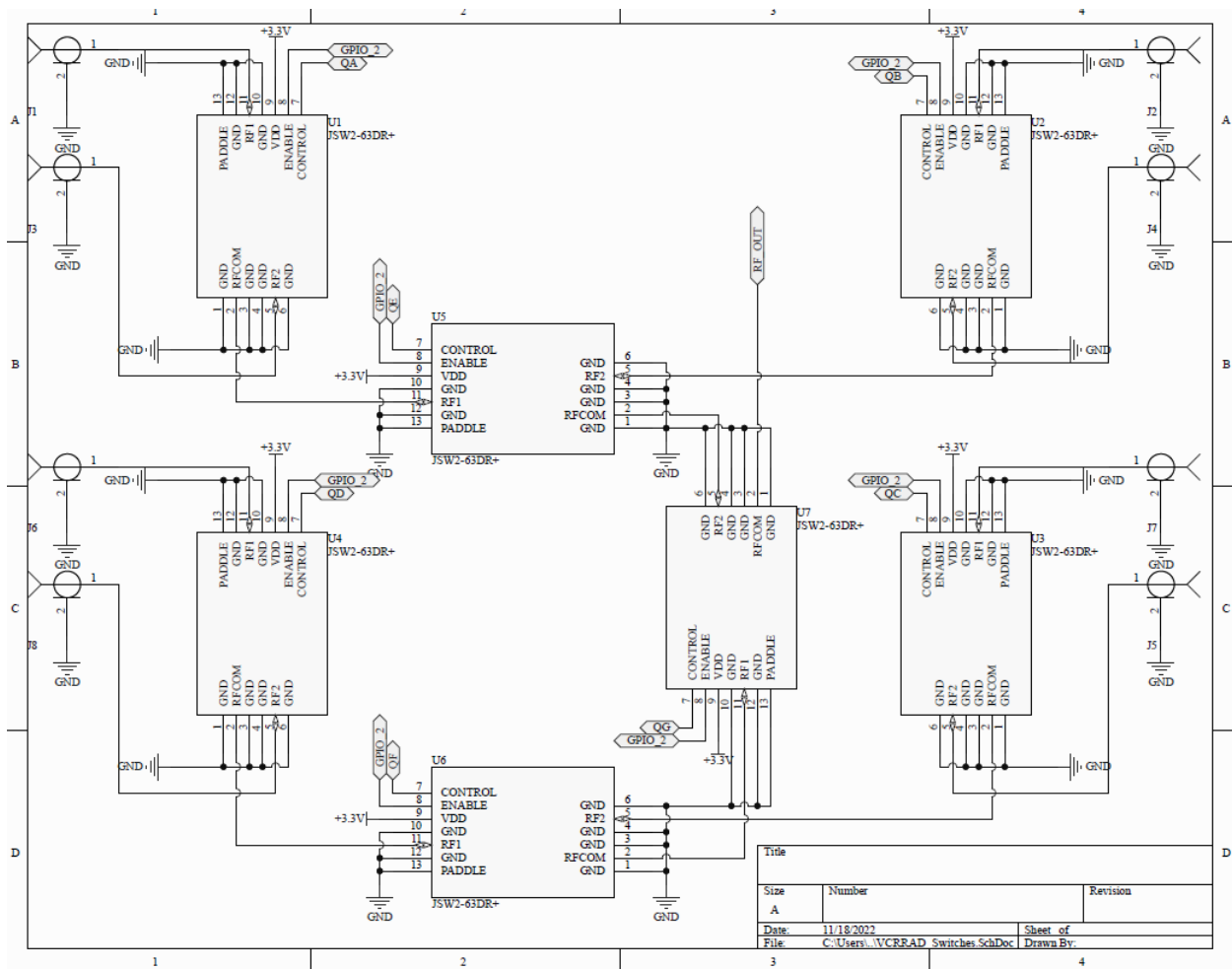


Figure 2: Input Network Schematic

The output amplifier subsystem is pictured in Figure 3. This subsystem includes a coupler and switch to allow a signal from the SDR to be directed towards the amplifiers for additional radiometer characterization capability, or towards the load to allow for input impedance characterization capability. The amplification is accomplished through the Mini-Circuits LHA-1H+, which advertises operation from 50-6000 MHz without the need for external matching components. The typical gain performance ranges from 17.7 dB at 50 MHz to 8.6 dB at 6 GHz. Three amplifiers are cascaded to achieve 25.8 dB gain at 6 GHz and 53.1 dB gain at 50 MHz.





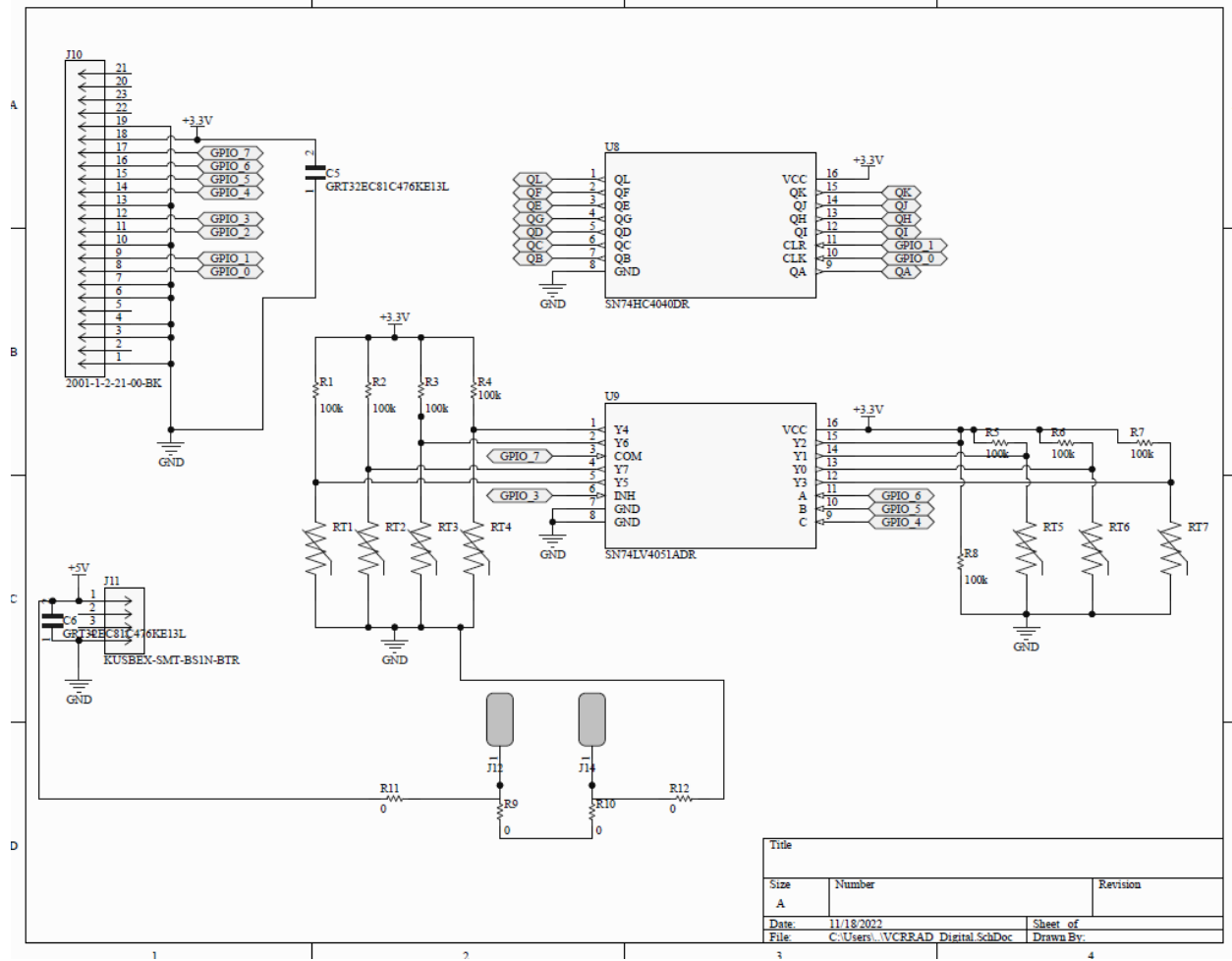


Figure 4: Digital Subsystem Schematic

## PCB Design

The VCRRAD PCB is designed to stack with the Ettus E320 for compact packaging. The current dimensions are 130 mm x 91 mm, which allows for an enclosure with 7 mm thick walls without exceeding the E320 envelope. The PCB contains 6 layers for signal routing. The top two layers are used for the RF paths. The RF path is designed with grounded coplanar waveguide traces on the top layer (with the second layer as the ground plane) and is impedance controlled to 50 ohms on RF traces. The bottom layer is where the digital devices and connectors are located. Layers 4 and 5 are used for routing signals between components on the board. Lastly, a narrow trace was routed throughout the third layer of the PCB to act as an onboard heater. The current flowing through this layer would have to be supplied and controlled externally, but would provide direct uniform heating to the radiometer electronics without the need for fans or sealed enclosures. A summary of how each layer is being used is available in Table 3. A rendering of the PCB is pictured in Figure 2 and the heating layer is pictured in Figure 3.

*Table 3: VCRRAD PCB Layer Descriptions*

Layer	Description
1 (Top)	RF Layer
	Grounded Coplanar Waveguide Design (GPCWG), contains all of the RF components of VCRRAD
2	Ground Plane Layer
	Used for GPCWG and convenient ground access anywhere on the board
3	Heating Layer
	Traces are routed on this layer to allow for uniform heating of the entire board. This feature may not be used depending on the thermal requirements of the system.
4	Signal Layer 1
	One of two layers for routing control and temperature signals
5	Signal Layer 2
	Second of two layers for routing control and temperature signals
6 (Bottom)	Interface and Control Layer
	Layer for USB and HDMI input connectors, digital control signals, and thermistor value multiplexing

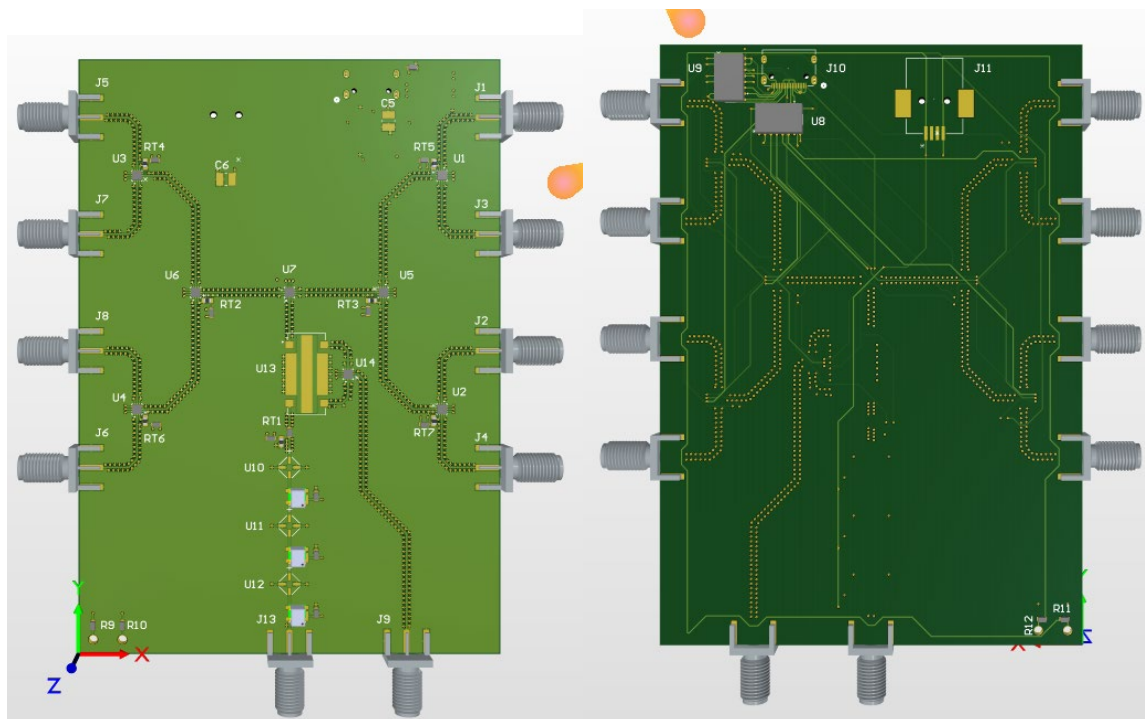


Figure 5: Rendering of VCRRAD PCB

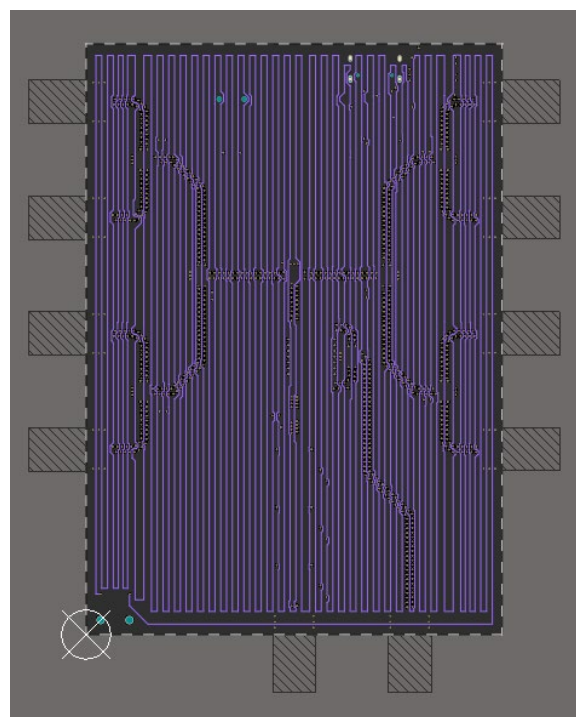


Figure 6: Heating layer

## Results

Multiple challenges were encountered during the development of VCRRAD. Parts availability issues and unexpected delays resulted in the prototype board arriving several months later than expected, limiting



the amount of testing that has been performed to date. The completed PCB is pictured in Figure 7 and the populated board is pictured in Figure 8.

Upon receipt and population of the board, all connections appeared to be as expected, but the s-parameters showed high noise and low gain on the output. Troubleshooting to date points to a possible

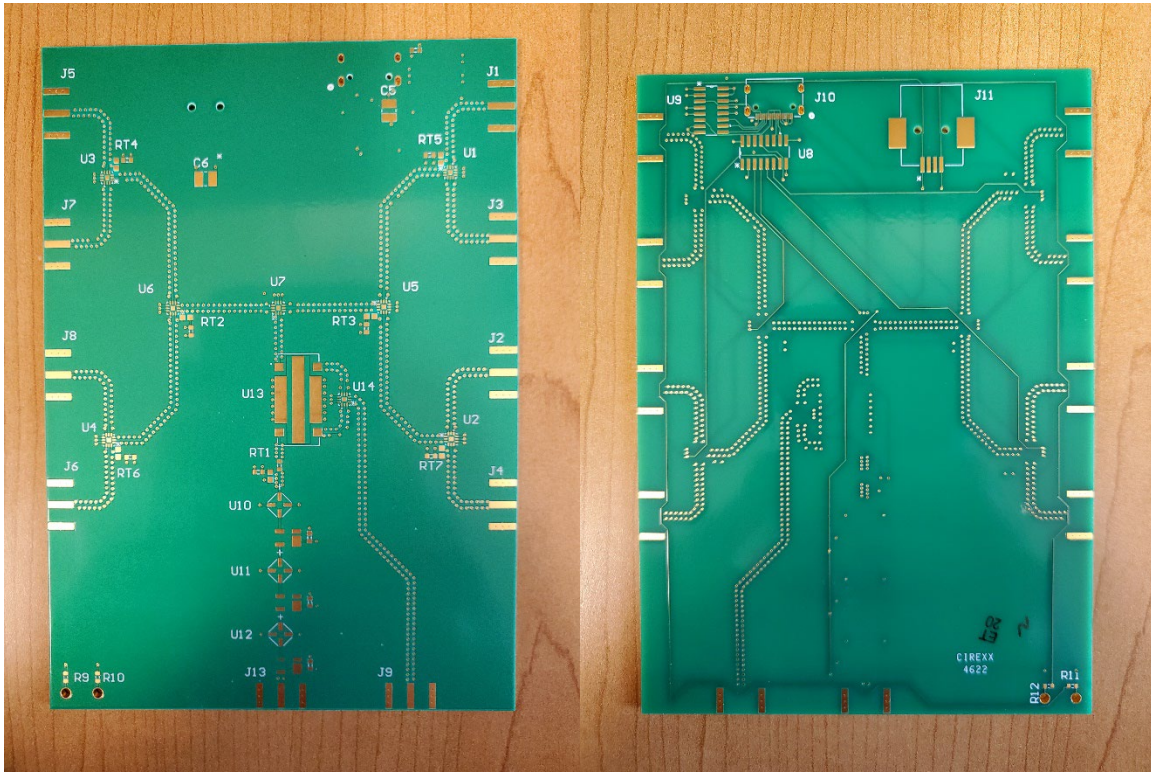


Figure 7: Unpopulated VCRRAD PCBs

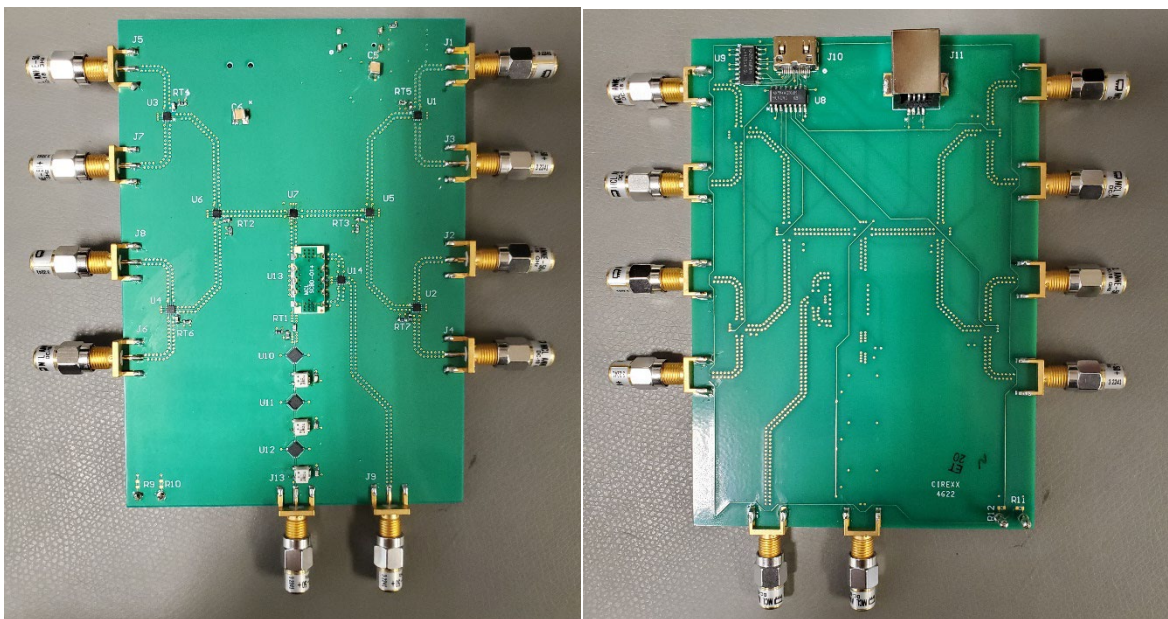


Figure 8: Populated VCRRAD PCBs

oscillation occurring in the output amplifier section. Tests to operate the output section with one amplifier instead of three are in progress at the time of this report. If the oscillation turns out to be the root cause, adding attenuation between amplifiers should solve the issue at the cost of some of the overall gain. To test this, the second amplifier in the chain can be removed and replaced with a T-configuration of resistors that provides attenuation while maintaining the 50 ohm characteristic impedance of the RF path. Another problem encountered was that the numbering convention the SDR manufacturer uses for the mini-HDMI connector does not match the convention used by the connector manufacturer, resulting in the pin numbering on VCRRAD being the reverse of what is expected. This can be corrected by cutting the HDMI cable and reconnecting the wires in reverse order or soldering the wires directly to the correct pads on the PCB.

If a second iteration of the PCB were to be pursued, improvements to the design itself could also be implemented. Currently, the thermistor voltage is returned on one of the GPIO lines, which cannot be read by the SDR and would need to be routed to another system to be interpreted and acted upon. This line should be routed to a completely different connector so that the HDMI connection does not need to be spliced, or conditioned into a control signal that can operate an external thermal control system. Additional test points, provisions for pads on the RF paths and select resistors should also be added to improve the ability to identify and respond to problems in the system.

## Conclusions

Although the first iteration of the VCRRAD PCB has encountered some problems, the project has shown that development of a compact radiometer compatible with drone-mounted software defined radios is very achievable. The size, weight and power constraints necessary to work on a drone mounted platform were easily met, and the performance issues should be correctable with repairs or a second iteration of the PCB design. VCRRAD will enable the groundbreaking field of wideband radiometry developed at ESL to be more accessible to new audiences and environments for a fraction of the time and cost that it would take to develop an instrument for specific bands.



# **Using a Structure from Motion Technique to Derive In-situ Surface Roughness**

## **CERF 2022 Final Report**

**Team: Tianlin Wang, Alexandra Bringer, Joel Johnson, and Mohammad M. Al-Khaldi**

### **Abstract**

Analysis of GNSS-Reflectometry data sets from satellite missions, such as TDS-1 and CYGNSS, reveals the presence of coherent reflected signals over land. Many investigations have been conducted to model land coherent returns using classic scattering theories. These theories use several parameters as inputs such as the geometry, the frequency, and surface descriptions. The surface is usually characterized by a root mean square (RMS) height of surface roughness.

The Shuttle Radar Topography Mission (SRTM) DEM is currently a standard product used for describing the surface in scattering theories. However, its spatial resolution (30 m) is insufficient to derive surface roughness that is associated with coherent scattering in GNSS-R measurements. More accurate measurements of the land surface RMS height can be achieved using a local airborne lidar survey. Lidar measurements provide surface information with a 5 cm vertical accuracy and a 30 cm spatial resolution. To fully characterize the surface roughness, in-situ measurements at a higher vertical accuracy and horizontal spatial resolution are needed and complement the lidar measurements.

The objective of this project is to assemble a system using structure from motion technique to infer in-situ surface roughness down to the millimeter scale. This method is based on stereo photogrammetry which consists in taking a series of convergent pictures of a scene and then using image processing tools to infer topography for instance. Lidar-based range measurement are also used for the structure from motion processing to produce surface topography. The resulting surface roughness measurements have higher vertical accuracy than the current available surface roughness measurements. These measurements complement surface roughness measurements derived from the lidar measurements that were acquired over CYGNSS calibration/validation (Cal/Val) sites in 2020 and 2021. The stereo vision system developed in this project will be used for the next CYGNSS Cal/Val campaigns scheduled for 2023.

### **Background and Motivation**

In the past decade, interest in GNSS-Reflectometry has significantly grown following the launch of TDS-1 [1] in 2014 and the 8 small-satellite constellation of the CYGNSS [2] in 2016. Analysis of data sets from these missions reveals the presence of coherent reflected signals over both land and ocean scenes in some cases [3]-[5]. A coherent return occurs when contributions from many points on Earth's surface arrive with similar phases and therefore add constructively. Many investigations have been conducted to model land coherent returns using classic scattering theories such as Physical Optics. These theories consider several parameters as inputs such as

the geometry, the frequency used, and surface descriptions. The surface is usually characterized by a root mean square (RMS) height of surface roughness that is derived in some studies using Digital Elevation Models (DEMs). The Shuttle Radar Topography Mission (SRTM) DEM [6] is currently a standard DEM used for describing the surface in scattering modeling theories, as the SRTM provides a global DEM with a spatial resolution of 30 m in the  $\pm 60$  degree latitude range.

The GNSS wavelength measured is 19 cm and coherent returns are expected to be significant only over very flat areas where the RMS height is of the order of a few centimeters (for example over inland water bodies) [7]-[8]. Analyses of the SRTM DEM demonstrate that such flat areas do not exist over typical land surfaces. However, this conclusion is impacted by the coarse horizontal and vertical resolution of the SRTM DEM, as clear coherent returns have been observed in CYGNSS reflected signals in a small set of inland locations that do not appear to be associated with inland water bodies. This demonstrates the need to obtain more accurate measurements of the land surface RMS height, which can be achieved using a local airborne Lidar survey. Two airborne campaigns were performed at the San Luis Valley and White Sands in 2020 and 2021, respectively. These lidar measurements provide information about the surface roughness with a 5 cm vertical accuracy and a 30 cm spatial resolution over large spatial areas with low vegetation. However, these data remain insufficient to resolve electromagnetic (EM) scale roughness on horizontal and vertical length scales finer than  $\sim 1$  m and  $\sim 5$  cm, respectively.

In-situ surface roughness measurements at a higher vertical and horizontal spatial resolution are needed to complement the lidar measurements. Traditional techniques for in-situ surface roughness measurements, including pin board, grid board, laser profilers, are shown in Figure 1. It is noted that these techniques have their own limitations: 1) coarse spatial resolution (cm level), 2) high uncertainty in vertical accuracy, 3) time-consuming for setup, measurement, and post-processing; 4) only providing 1-D cuts of the surface profile. Thus, an accurate, robust, and automated method that characterizes 2-D surface structure is needed for in-situ roughness measurement. It should provide higher vertical and horizontal spatial resolution to complement the airborne lidar measurements over moderately sized regions.

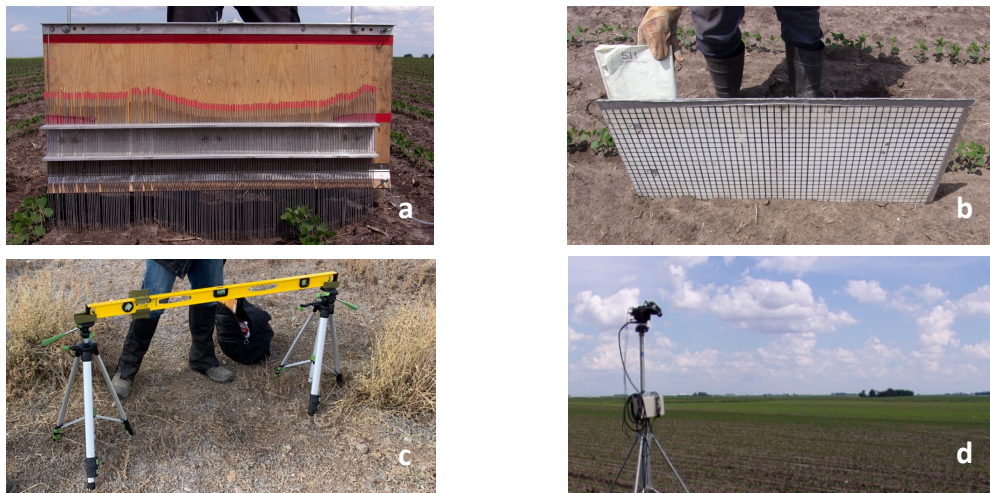


**Figure 1 Traditional approaches: (a) pin board, (b) grid board, (c) & (d) laser profiler [9, 10]**

## Project Overview

This project examined techniques to measure surface roughness at high vertical and horizontal resolution with high accuracy. One technique is based on stereo photogrammetry which consists in taking several pictures of the same object at different view angles and then using some image processing tools in order to reconstruct the 3D object (Figure 2). In our case, multiple convergent images of the soil surface were made at different view angles. Those multiple images are then fed into a dedicated software along with information about the geometry and the position of the camera. The software then performs image processing to reconstruct the 3D image and finally retrieve the surface roughness.

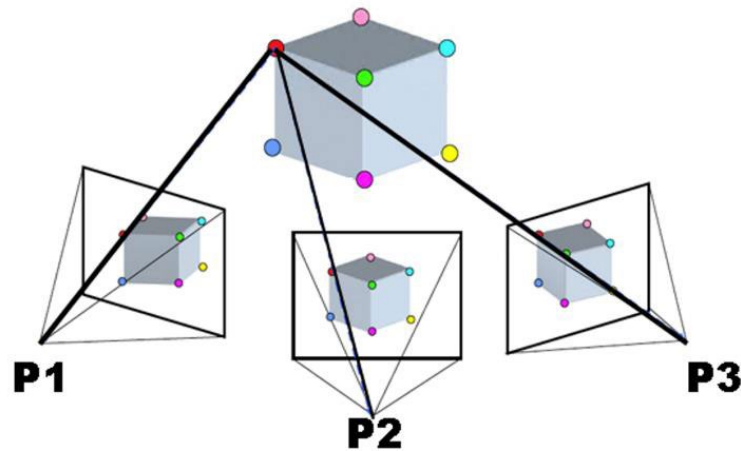


**Figure 2 Illustration of the stereo photogrammetry principle**

A second technique uses similar processing to infer surface topography by using the range information that can be directly measured by the lidar sensor on iPhone or iPad.

One step further is to conduct the photogrammetry and lidar measurements using a drone that can cover a larger region than in-situ measurements. This is expected to reveal more information about the surface spectrum.

A list of equipment and software is shown in Table 1. The iPad is used to do both photogrammetry and lidar measurements. A picture of the drone, extra batteries, and extra SD cards is shown in Figure 3. These allow us to fly the drone for more than a half day during a field campaign.

**Table 1 List of equipment and software**

Equipment	iPad Pro 12.9 Cellular 512 GB
	Autel Robotics Evo II Rtk Rugged Bundle
	Extra Batteries *3
	Extra SD Card * 2
Software	Agisoft MetaShape Professional Edition (Educational License)
	PolyCam Pro



**Figure 3 Autel Robotics Evo II Rtk Rugged Bundle with extra batteries and SD cards**

## **Experiment and Preliminary Results**

### **A. Experiment 1: Photogrammetry of a Bare Soil Surface**

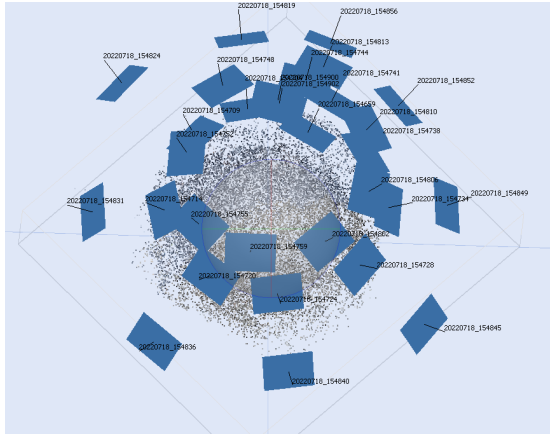
A test was completed over a bare soil surface in July 2022. 30 photos were taken at different viewing angles and input to the Agisoft Metashape for photogrammetry processing. Sample photos are shown in Figure 4.



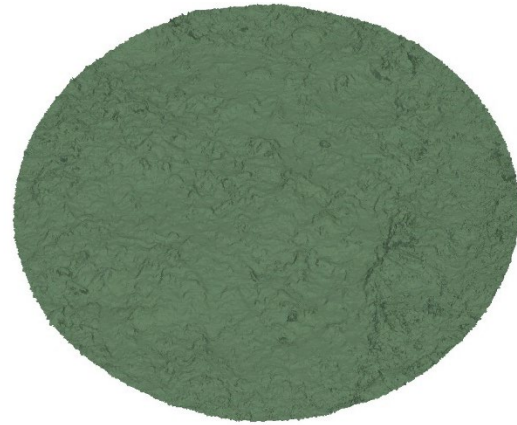
**Figure 4 Examples of the photos taken at the test site**

Figure 5(a) shows the computed point cloud and the locations of the aligned cameras. Figure 5(b) shows the reconstructed 3D model. These results demonstrate that this technique successfully captures the 3D structure of a bare soil surface.





(a)



(b)

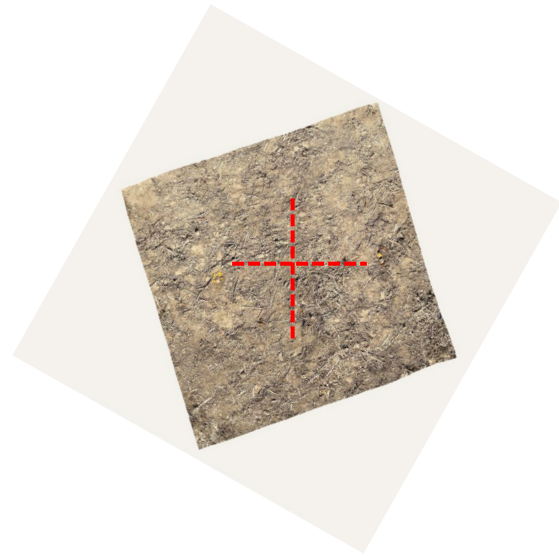
Figure 5 (a). Point cloud and aligned cameras. (b) 3D model

## B. Experiment 2: Lidar Measurement vs. Laser Profiler Measurement

An experiment using the iPad lidar was conducted in October at the farm site near ESL. We also use a laser profiler system to measure the surface profile. Figure 6(a) shows a picture of the laser profiler, and Figure 6(b) shows the site and two cuts of the two orthogonal profiles.



(a)



(b)

Figure 6 (a). Laser profiler (b) Cuts of profiles over surface

The two measured profiles are shown in Figure 7. It is noted that the spatial resolution is 2 cm.

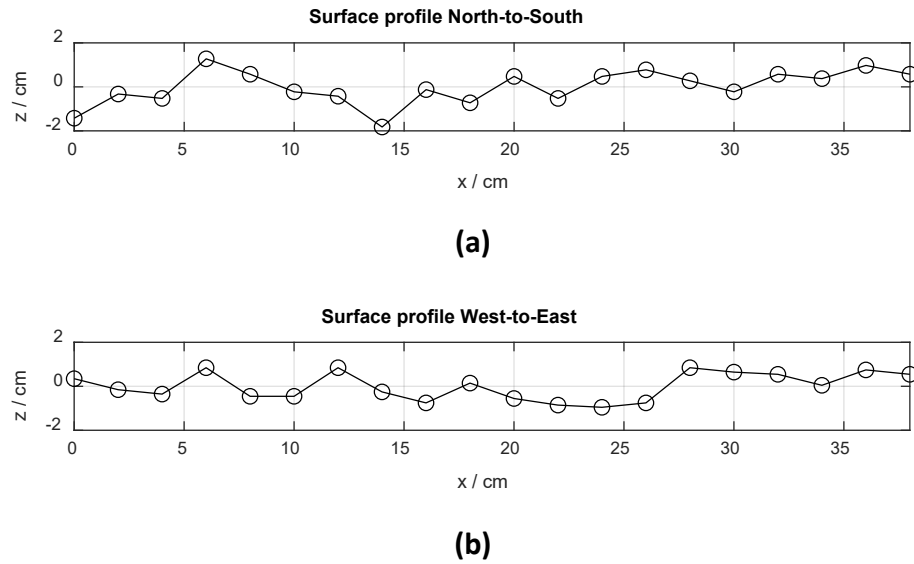


**Figure 7 Surface profile (a). North-to-South (b) West-to-East**

The iPad lidar, along with the PolyCam Pro, was then used to reconstruct the 3-D structure, as shown in Figure 8. The results not only has a much higher spatial resolution but also reveal a much finer structure of the surface. The dataset also provides a 2-D structure rather than only 2 cuts. In addition, this approach takes much less time to set up the system, conduct measurements, and post-process the data.

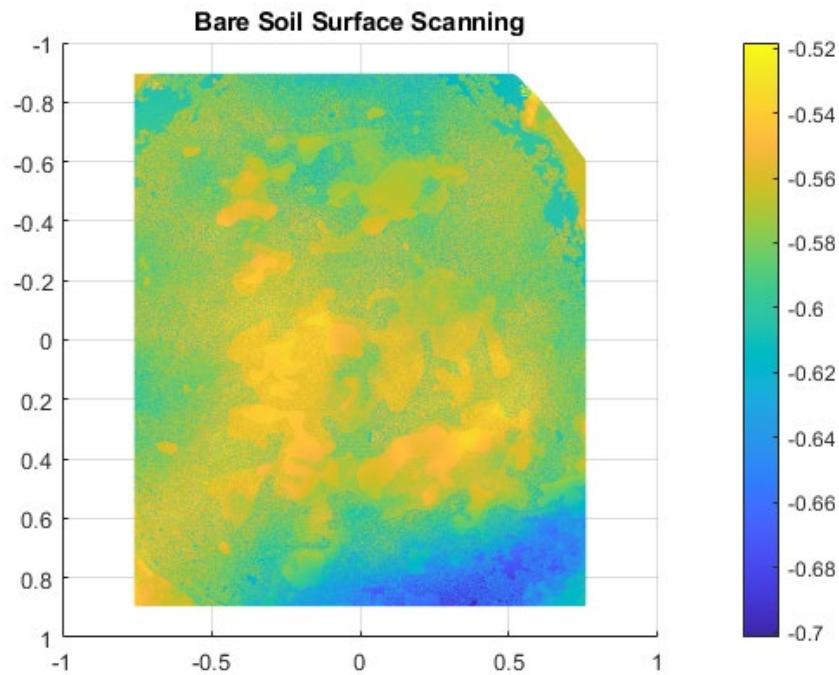


**Figure 8 Reconstructed structure of bare soil surface at ESL site**

### C. Experiment 3: Lidar Measurement of Known Structure

A DEM with a known structure [11] was printed out using a 3-D printer, as shown in Figure 9. The scaling factor between the input DEM and the printed model is 1000 AU / 1m. The size of the model was 16 cm in length, 11.6 cm in width, and 4.1 cm in height.



**Figure 9 The 3-D printed DEM with known structure**

The DEM was then scanned by the iPad and then processed by PolyCam Pro. The output point cloud data was then processed to reconstruct the surface topography. Then the difference between the input DEM data and the reconstructed structure is computed. The raw DEM, rescaled DEM, reconstructed DEM, and the difference map are shown in Figure 10. The root mean square deviation (RMSD) between the rescaled and reconstructed DEMs is 0.0016 m. This successfully demonstrated that both the spatial resolution and vertical accuracy can be at the millimeter level when in-situ lidar measurements are performed.

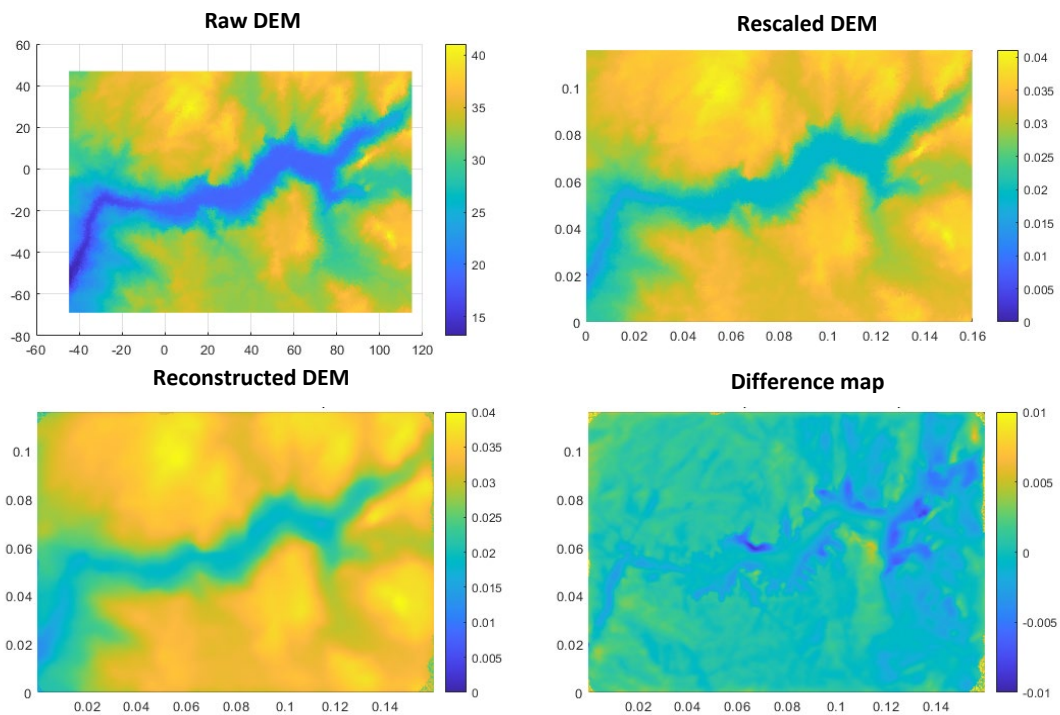


**Figure 10 Raw DEM, re-scaled DEM, reconstructed DEM, and difference map**

## Summary and Ongoing Work

A stereo vision system using the structure from motion technique is being developed to make accurate surface roughness measurements. Preliminary results show that this technique can capture the 3D structure of bare soil surfaces and reconstruct the 2-D surface topography on millimeter-scale spatial resolution and vertical accuracy. This technique will be used for NASA CYGNSS's Cal/Val campaigns planned in Spring 2023.

Our ongoing work includes 1) Camera calibration and alignment; 2) Advanced post-processing of surface structure; 3) Validation with roughness measurement made by other techniques; 4) Implementing this technique on a drone for roughness measurement over a large area.

Drone photogrammetry with professional, high-resolution cameras can cost-effectively generate surveys with absolute accuracies down to 1 cm rms horizontally and 3 cm rms vertically [12]. This technique will potentially fill the gap between airborne lidar and in-situ roughness measurements and reveal additional information on 'intermediate' scale roughness. It will complement 'topographic' and 'microwave' scale information to derive a full spectrum of surface roughness.

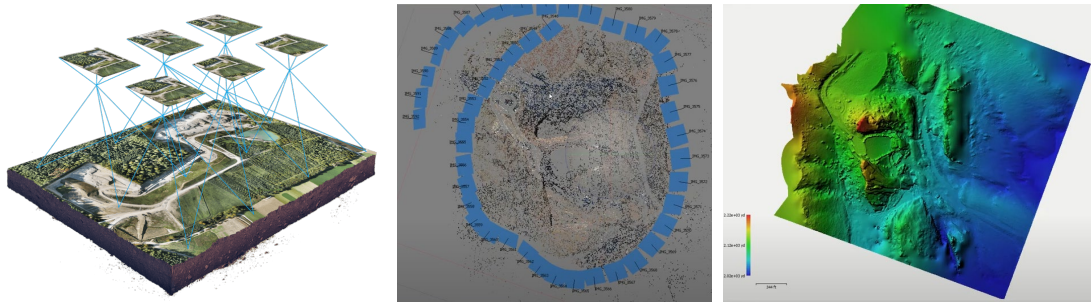


**Figure 11 Demo of drone photogrammetry [12], [13]**

## Broader Impact

Accurately modeling the GPS-reflected signal over land is critical for many GNSS-R applications over land, such as soil moisture estimation. Surface roughness is one of the key input parameters of the scattering theories and one of the main unknowns, as no system can measure surface roughness at a very fine scale globally. A stereo photogrammetry/lidar system enables us to estimate surface roughness on a millimeter scale. Combining it with an airborne lidar dataset can provide a complete description of the spectrum of land surface roughness impacting GNSS-R reflections. These results will serve as critical inputs to electromagnetic wave scattering models and play a significant role in the Cal/Val of GNSS-R land surface measurements. This project will be beneficial for ESL as it will improve the modeling of reflected GPS and other scattered or emitted microwave signals, and it also allows the team to continue their effort in the CYGNSS Cal/Val activities.



## **Publication**

A conference abstract based on this work will be presented at the 2022 American Geophysical Union (AGU) Fall Meeting (Dec. 12-16, 2022): T. Wang, A. Bringer, and J. Johnson, "Land Surface Roughness Investigations Using Airborne Lidar and Stereo Photogrammetry," 2022 American Geophysical Union (AGU) Fall Meeting, Chicago, IL and Online Everywhere, Dec. 12-16, 2022.

The team is also considering submitting abstracts to the 2023 IEEE Specialist Meeting on Reflectometry using GNSS and other Signals of Opportunity, Boulder, CO, and the 2023 IEEE International Geoscience and Remote Sensing Symposium (IGARSS), Pasadena, CA.

1 journal paper is also planned.

## **Acknowledgment**

The authors would like to acknowledge the Consortium on Electromagnetics and Radio Frequencies (CERF) for supporting this research project and thank the Ohio State University Digital Union for the free 3-D printing service.

## **References**

- [1] Unwin, M., Duncan, S., Jales, P., Blunt, P. and Tye, J., 2014, September. Implementing GNSS-reflectometry in space on the TechDemoSat-1 mission. In Proceedings of the 27th International Technical Meeting of the Satellite Division of The Institute of Navigation (ION GNSS+ 2014) (pp. 1222-1235).
- [2] Ruf, C.S., Gleason, S., Jelenak, Z., Katzberg, S., Ridley, A., Rose, R., Scherrer, J. and Zavorotny, V., 2012, July. The CYGNSS nanosatellite constellation hurricane mission. In 2012 IEEE Intl. Geoscience and Remote Sensing Symposium (pp. 214-216).
- [3] Park, J., Johnson, J.T. and O'Brien, A., 2017, May. TDS-1 coherent returns over sea ice and land surfaces. In GNSS+ R 2017: Specialist Meeting on Reflectometry using GNSS and other Signals of Opportunity.
- [4] Loria, E., O'Brien, A. and Gupta, I.J., 2018, July. Detection & separation of coherent reflections in GNSS-R measurements using CYGNSS data. In IGARSS 2018-2018 IEEE International Geoscience and Remote Sensing Symposium (pp. 3995-3998).
- [5] Gleason, S., O'Brien, A., Russel, A., Al-Khaldi, M.M. and Johnson, J.T., 2020. Geolocation, calibration and surface resolution of CYGNSS GNSS-R land observations. Remote Sensing, 12(8), p.1317.

- [6] Rodriguez, E., C.S. Morris, J.E. Belz, E.C. Chapin, J.M. Martin, W. Daffer, S. Hensley, 2005, An assessment of the SRTM topographic products, Technical Report JPL D-31639, Jet Propulsion Laboratory, Pasadena, California, 143 pp.
- [7] Gleason, S., O'Brien, A., Russel, A., Al-Khaldi, M.M. and Johnson, J.T., 2020. Geolocation, calibration and surface resolution of CYGNSS GNSS-R land observations. Remote Sensing, 12(8), p.1317.
- [8] Rodriguez, E., C.S. Morris, J.E. Belz, E.C. Chapin, J.M. Martin, W. Daffer, S. Hensley, 2005, An assessment of the SRTM topographic products, Technical Report JPL D-31639, Jet Propulsion Laboratory, Pasadena, California, 143 pp.
- [9] Hornbuckle, B., Walker, V., Wallace, V., Eichinger, B., and Yildirim, E., 2017. Soil surface roughness measurements during SMAPVEX16-IA. SMAP Cal/Val Workshop, June 2017, Amherst, MA.
- [10] Akbar, R., Silva, A. R., Chen R., Entekhabi D., and Moghaddam M., 2020. SoilSCAPE in situ soil moisture networks for CYGNSS land applications. CYGNSS Science Team Meeting Jan. 2020, Pasadena, CA.
- [11] California Science Teacher. Physical Modeling using 3D Printing. Online Materials: <https://sites.google.com/site/cascienceteacher/cscs-activites/cscs-earth-science/physical-modeling-using-3d-printing>.
- [12] Torres, G., 2021. Drone know-how Drone photogrammetry vs. LIDAR: what sensor to choose for a given application. Online: <https://wingtra.com/drone-photogrammetry-vs-lidar/>.
- [13] Hunnicutt, R., 2018. Agisoft Photoscan Professional Tutorial: Creating a DEM without GCPs. Online: <https://www.youtube.com/watch?v=McMGyo98Ffw>.

# **X-Ray Communications Testbed**

Christopher Ball (PI), Pietro Lavezzo, ElectroScience Laboratory  
Ibrahim Oksuz, Vasil Hlinka, AwareAbility Technologies

## **Abstract**

Researchers at the ElectroScience Laboratory (ESL) are collaborating with AwareAbility Technologies (AAT) to develop X-Ray communication (XCOM) technologies for spaceborne applications. XCOM offers unprecedented potential for high data rates, long range, low probability of intercept, and penetration through ionized regions associated with spacecraft re-entry or hypersonic vehicles. Our team's long-term goal is to demonstrate an XCOM link in space on CubeSat platforms. AAT has licensed a miniaturized high-speed modulated X-Ray source (MXS) technology from NASA as the foundation for an XCOM link. Previously, we developed a MATLAB simulation tool to explore XCOM link performance metrics (e.g., bit error rate, link margin, transmitted beam width) based on the MXS technology using amplitude shift keying (ASK) modulation to increase data rates at a fixed modulation frequency. In the current study, we have implemented a laboratory testbed based on the MXS to demonstrate simple propagation and modulation of an X-ray source. This report summarizes a variety of diagnostic tests and outlines next steps toward development of an XCOM system.

## **Introduction**

State-of-the-art spaceborne communication systems use radiofrequency (RF) or free-space optical (FSO) technology, which has been matured over decades of research and commercial development. Recent examples of NASA-funded spaceborne optical communications projects include the Lunar Laser Communication Demonstration (2013-14), which observed 622 Mb/s moon-to-Earth data transfer,<sup>1</sup> and the Laser Communications Relay Demonstration, which targets 1.244 Gb/s.<sup>2</sup> However, general performance characteristics of RF and FSO links, such as data capacity, beam divergence, etc., are fundamentally limited by the carrier frequency. XCOM, however, offers the potential to exceed the performance of current spaceborne communications technology by providing increased data rates, high gain, reduced probability of intercept, smaller size and weight, and operability in ionized environments.<sup>3</sup>

Successful testing of an XCOM link in a space environment is of strong interest for civilian entities (NASA) and military/intelligence agencies (NRO, DARPA, USAF, USSF) with needs for high bandwidth, secure inter-satellite communications. For example, NASA recently developed a miniaturized X-Ray source<sup>4</sup> as part of an effort to develop a capability to communicate with space vehicles during re-entry blackout periods. Although the near-term use case for XCOM technology is focused on inter-satellite communications, the long-term uses are far more extensive and deal with a multitude of near and deep space communication applications. XCOM could also support communications for hypersonic vehicles in the upper atmosphere or Low Earth Orbit and during certain other critical events such as Electromagnetic Pulse induced by nuclear detonation or meteor strike.<sup>5</sup>

Researchers at ESL and AAT are developing XCOM concepts as a compelling alternative to spaceborne communications systems based on RF and FSO technologies. Our long-term goal is to mature and integrate component technologies, including the MXS technology licensed from NASA's Goddard Spaceflight Center<sup>6</sup> and a high efficiency, wide-bandgap detector technology licensed from OSU,<sup>7</sup> to produce a space-qualified XCOM link suitable for test on small satellite (e.g., CubeSat) platforms. ESL is

focusing on a system-level approach for integrating and testing an XCOM link. Our baseline concept is to use simple on-off keying (OOK), which we estimate can provide ~350 Mb/s based on the ~1 ns risetime limitation of the X-Ray source. Although NASA and AAT believe this risetime can be reduced to increase data rate, ESL researchers are investigating additional data rate gains achieved through higher order modulation, for which preliminary estimates suggest data rates >10 Gb/s. Ultimately, our goal is to produce an XCOM link that exceeds the performance of state-of-the-art spaceborne FSO systems.

Under CERF funding in 2021, we initiated development of a MATLAB-based simulation tool to explore XCOM link performance metrics (e.g., bit error rate, link margin, transmitted beam width) based on the MXS technology. This study focused specifically on the use of amplitude shift keying (ASK) modulation that can increase data rates of an XCOM link for a fixed modulation frequency. A final report on this study provides detail on our accomplishments with the simulation tool.<sup>8</sup>

## Objectives

For the 2022 CERF project, our primary objective was to develop a laboratory XCOM capability at ESL and to demonstrate simple X-ray propagation and modulation. This would involve setting up the MXS and other necessary electronics, performing tests of individual components, and then testing performance of a simple XCOM configuration. A secondary objective was to continue to enhance the MATLAB simulation tool, ultimately to enable validation of the simulation based on lab-acquired data.

## XCOM Laboratory Setup

The XCOM test system is built around NASA's MXS technology, shown schematically in Fig. 1. This source generates radiation by converting ultraviolet (UV) photons into high energy electrons, which strike a target material to produce X-ray photons. Both the multiplier and target require DC high voltage (~3kV, 10kV respectively). The X-ray beam is modulated by varying the LED drive voltage that produces the UV photons. For test purposes, this modulation is a simple square wave from a standard function generator. Future studies will investigate more sophisticated amplitude modulation (e.g., ASK) using time-varying analog

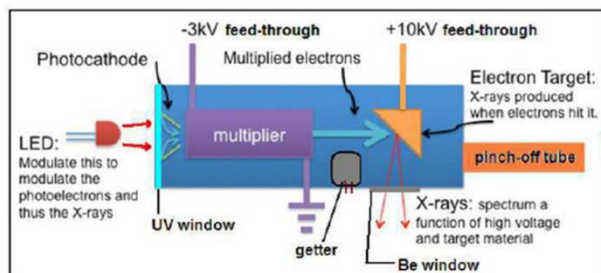


Figure 1. Schematic diagram of the MXS system showing conversion of UV photons to X-rays using a multiplier and electron target.<sup>4</sup>

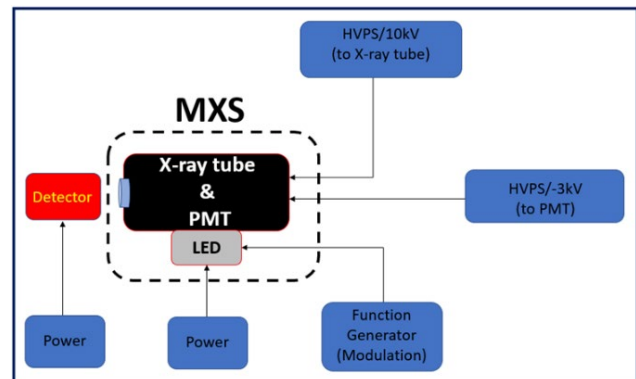


Figure 2. Block diagram testbed layout of the MXS, function generator, X-ray detector, and associated power supplies.

signals. The modulated X-ray beam is propagated across a very short distance (on the scale of cm) toward a Lanthanum-Yttrium Oxyorthosilicate (LYSO) crystal, which converts the X-ray photons to optical via scintillation. This scintillation signal is then detected by a Silicon Photomultiplier (SiPM). The LYSO crystal is wrapped in Teflon tape, which is semitransparent to X-rays, to confine the scintillation signal. Fig. 2 shows a block diagram of the MXS, function generator, detector, and power supplies, and Fig. 3 shows photographs of the configuration of the MXS and LYSO/SiPM detector as installed in the laboratory.

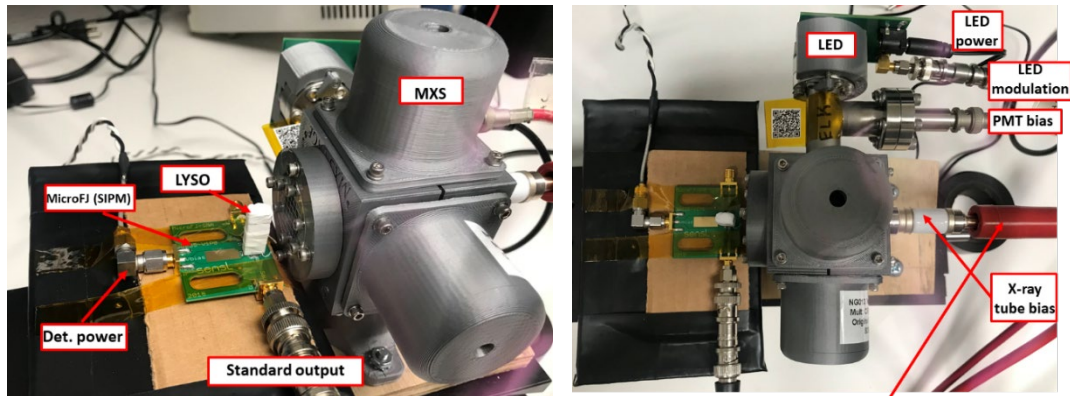


Figure 3. Laboratory implementation of the XCOM test system, showing the configuration of the LYSO/SIPM detector relative to the MXS (left) and a top view of the MXS showing various electrical connections (right).

## Diagnostic Test Results

After installing and testing each component of the XCOM test system, we performed several diagnostic tests, ostensibly to increase the signal-to-noise ratio (SNR) of the detected X-ray signals as well as understand the overall operation and idiosyncrasies of the setup.

### *Teflon tape thickness*

It is common practice to wrap the LYSO scintillation material in Teflon tape to prevent optical photons from escaping the LYSO material, thereby maximizing the number of photons incident on the SIPM detector. However, Teflon is not perfectly transmissive to low energy X-ray photons, and if the Teflon tape is too thick, it can reduce the number of X-ray photons reaching the LYSO material. After observing relatively weak signals from the detected X-rays, we investigated the impact of the Teflon tape thickness on measured SNR. For a first test, we removed the Teflon tape from the LYSO surface through which the X-rays propagate, keeping the rest of the LYSO material wrapped. We took a series of measurements of the X-ray signal, and then covered the unwrapped surface with a single layer of Teflon tape (0.01 cm thickness). Adding the Teflon tape reduced the X-ray signal by 40%. Then a second layer of Teflon tape was added, further reducing the X-ray signal by more than 50%. Fig. 4 shows the difference in measured signals between one layer and two layers of Teflon tape.

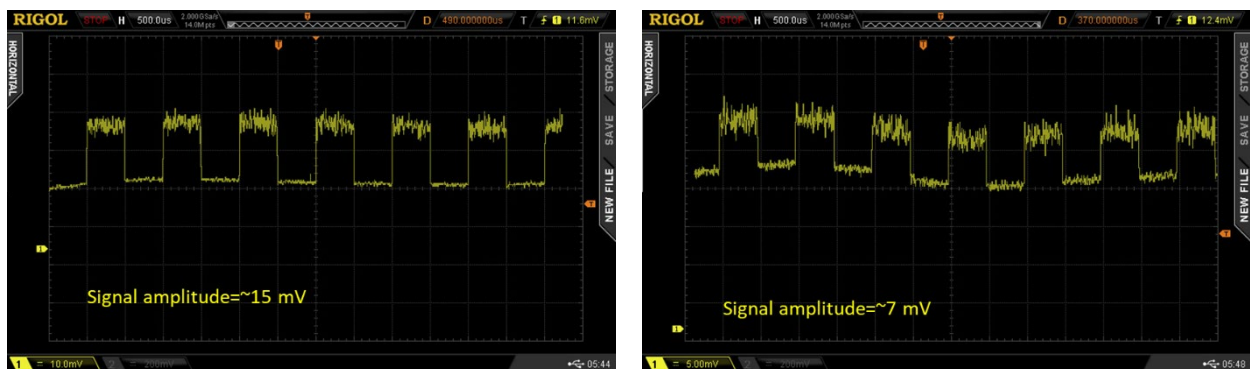


Figure 4. Measured square wave modulated X-ray signals propagating through one layer of Teflon tape (left) and two layers (right), indicated more than 50% signal loss with the addition of the second layer.

These results are consistent with calculated X-ray transmission losses through Teflon, assuming Teflon density of  $2.2 \text{ g/cm}^3$  and low energy X-rays ranging from 5-10 keV. Fig. 5 shows predicted transmission losses as a function of Teflon thickness, indicating that the incident X-rays in our experiments have energy of approximately 5.5 keV (consistent with 10 kV applied to the X-ray target, factoring in resistive losses in the cable connecting the high voltage supply to the MXS).

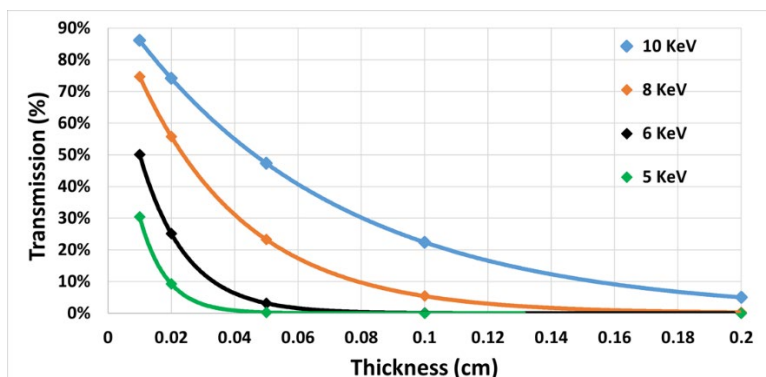


Figure 5. Predicted X-ray transmission loss as a function of Teflon thickness for low energy X-rays (5-10 keV).

### *Multiplier voltage*

To gain familiarity with the operation of the MXS, we investigated how the X-ray output was affected by the high voltage applied to the photomultiplier inside the MXS housing. The hypothesis is that, for a fixed target voltage (10 kV), the intensity of the X-ray beam should increase as the multiplier voltage is increased. As shown in Fig. 6, we did in fact observe significant X-ray signal increases (by more than a factor of 5) as the multiplier voltage was increased from 2.5 to 3.0 kV. Fig. 7 shows that the signal increase is non-linear over the 2.5-3 kV range.

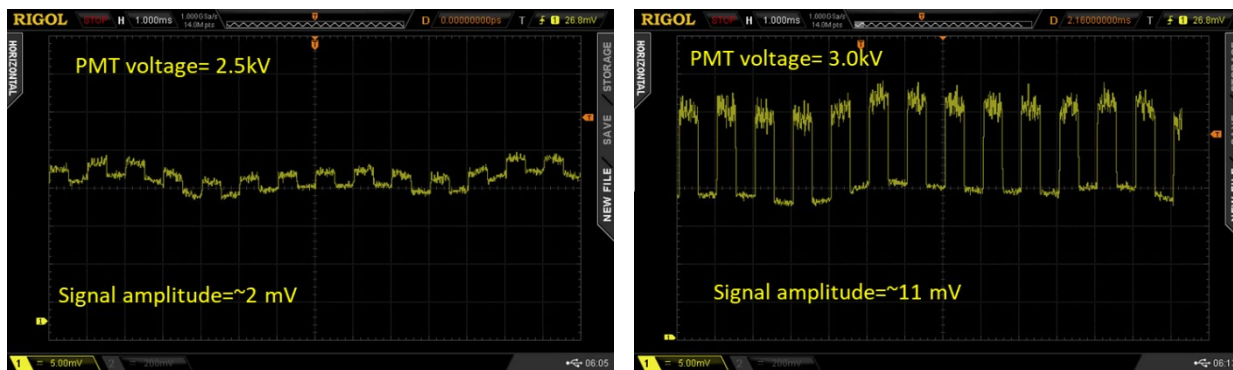


Figure 6. Measured X-ray signal increases substantially as multiplier voltage is increased from 2.5 kV (left) to 3.0 kV (right).

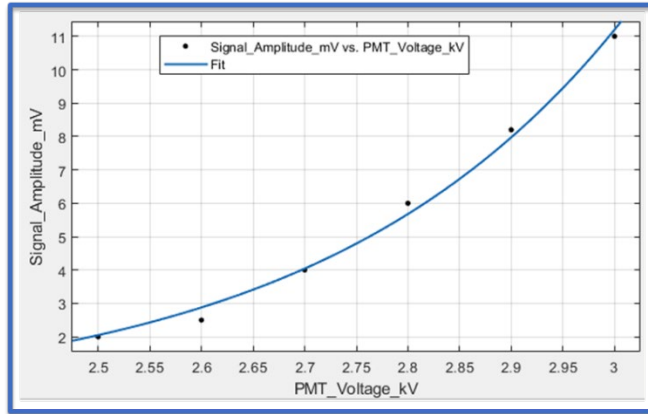


Figure 7. Plot of X-ray signal amplitude as a function of multiplier voltage, indicating nonlinear behavior.

### *Modulation frequency*

Although the MXS is specified to have a 1 ns rise time, we were unable to test this level of speed with the test equipment and SIPM detector at our disposal. We were, however, able to test the effects of changing the square wave modulation frequency on the X-ray signal, as shown in Fig. 8. In general, these studies indicated that the overall level of noise increases with increasing modulation frequency, and that at the highest frequencies we observe non-square wave transient effects, as shown in Fig. 9. These transient effects appear to be related to the combination of scintillation effects in the LYSO material with the SIPM detector, which is not inherently a high-speed detector. The “Fast Output” option for the SIPM has rise-times of several ns, and the “Standard Output” has fall-times of 10s of ns. Future studies should consider incorporation of faster X-ray detectors (PMT or other) to better characterize the rise time of the MXS and thus the bandwidth of the XCOM transmitter/receiver system.

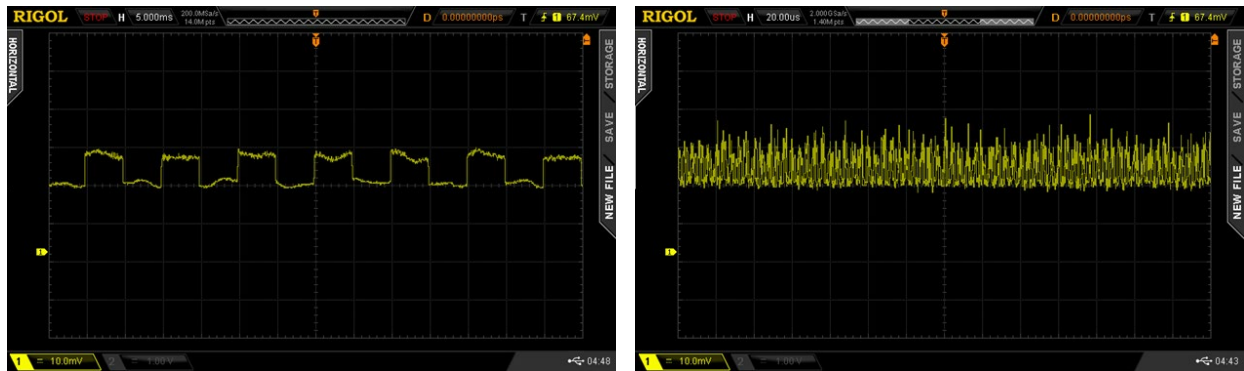


Figure 8. Increasing modulation frequency from 100 Hz (left) to 100 kHz (right) produces increased noise and illuminates presence of various transient effects.





Figure 9. X-ray signal modulated at 500 kHz (zoomed in) indicates fast rise time (few ns) and non-square wave temporal response due to scintillation and SIPM transient effects.

### *Beam size and divergence*

To test the intensity, shape, and divergence of the X-ray beam, we used a CMOS camera (provided by AAT) in conjunction with a ZnS scintillator screen to image the outgoing beam. The test setup for these measurements is shown in Fig. 10. Using fixed settings for the high voltage supplies and modulation frequency, we measured the diameter of the beam from the CMOS images at a variety of distances between the MXS and the scintillator screen. Fig. 11 shows examples of these images and measurements, and Fig. 12 shows a plot of beam radius vs. distance, indicating a beam divergence of  $\sim 67^\circ$  for the MXS.

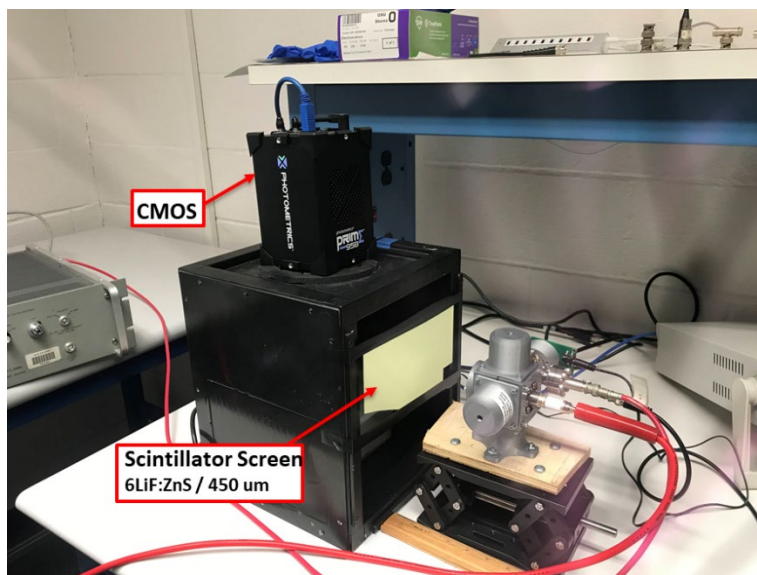


Figure 10. Test setup for beam size and divergence measurements, which allows for X-ray beam imaging using a scintillator screen and CMOS imager.



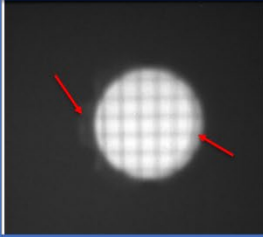
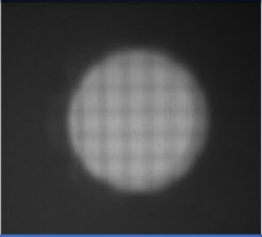
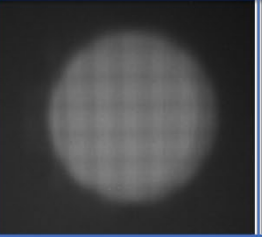
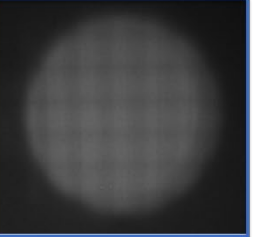
<b>X-ray Beam Radiograph</b>				
Source-to-detector distance	5cm + 0"	5cm + 1"	5cm + 2"	5cm + 3"
Beam diameter	~41.1 mm	~52.9 mm	~65.0 mm	~76.9 mm

Figure 11. Example X-ray beam profile images and beam diameter measurements for several distances between the MXS and scintillator screen.

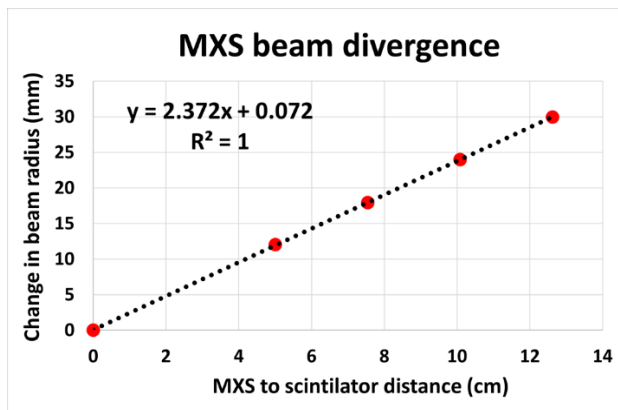


Figure 12. Plot of beam radius vs distance, indicating a beam divergence of  $\sim 67^\circ$  for the MXS.

### MATLAB Simulation Enhancements

In addition to the laboratory investigations, we also continued to upgrade and optimize the MATLAB simulation tool developed under 2021 CERF funding. Since last year, the MATLAB simulation has been updated by introducing a menu that facilitates calculations of link margin and beam width over a range of distance, noise, or transmitted signal power. As shown in Fig. 13, the user inputs minimum and maximum values for these independent variables, as well as the number of data points to calculate, and the MATLAB simulation creates an array and calculates the beam width or link margin over that array of values. As one of the parameters changes, the parameters that remain constant are still defined within a .json file. The menu then displays a graph with the data calculated with the user-inputted values. The next steps are to fully integrate the menu options for calculations of bit error rate and to validate all results with experimental data from the laboratory set up. Some small optimizations were also made to the code, especially when calculating the bits, and converting them to transmitted power.

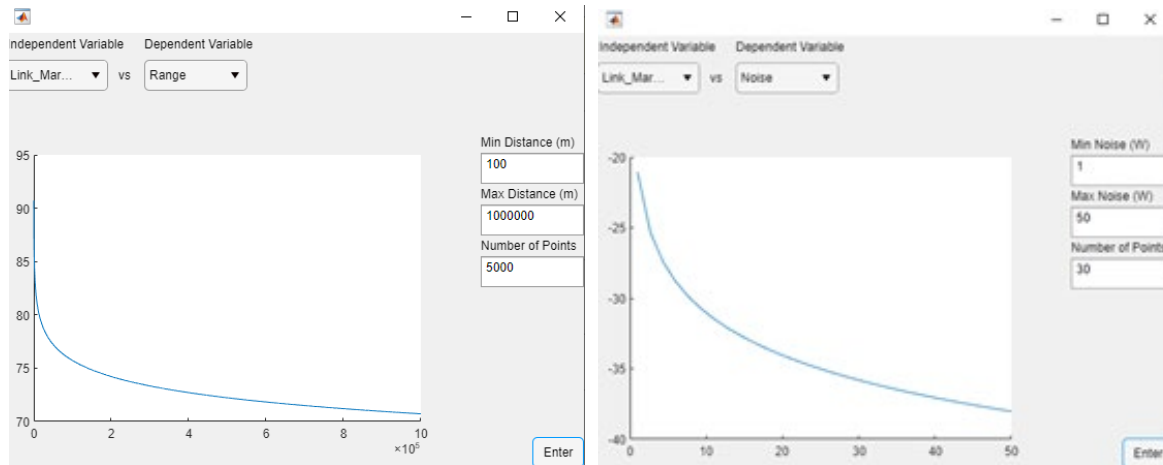


Figure 13. New MATLAB interface allows user to select parameters of interest (link margin, beam divergence) that are calculated as a function of various selectable dependent variables (range, noise, transmitter power) over specified data ranges.

### Next Steps

Based on the successes of this project to date, we are very confident that our XCOM approach is feasible, and that additional engineering should enable future integration onto a spaceborne platform. However, we have several issues related to X-ray signal intensity and speed to overcome, suggesting the following activities.

1. Replace the LED module with higher speed, shorter wavelength LEDs. The current LED module uses LEDs centered around 370 nm, however shorter wavelengths yield more energy per photon and therefore higher energy X-rays. In terms of speed, we have shown in the current project that the rise time limitations of the MXS currently are due to the speed of the LED module. We intend to revisit the LED circuit and selection of LED components to increase the switching speed to be faster than 1 ns.
2. Investigate alternative detector options. The current SIPM detector may be fast enough to detect the rising edge of the X-ray signal, but it has a very long decay time (10s of ns). Various silicon avalanche photodiodes may provide better switching speed on the detector side (~200 ps) and thus may improve receiver bandwidth. Also, we intend to find detector options that do not exhibit as much ringing and susceptibility to 60 Hz interference.
3. Upgrade high voltage supplies and cabling. The multiplier high voltage supply is nearly 30 years old and offers limited control for slow turn-on time (which is needed to help preserve the life of the MXS component). In addition, the target high voltage cable uses a spark plug wire, which we have found has unacceptably high resistance and is reducing the overall X-ray signal intensity.
4. Helium purge. Because the X-ray emission is of relatively low energy (5-10 keV), it is more susceptible to atmospheric constituents like Argon during propagation. Implementing a Helium purge will reduce transmission losses due to X-ray attenuation in air.

Once we have made these improvements and optimizations, the next step is to generate data that we can use to validate the MATLAB simulation tool. In addition, we can start to consider customized electronic solutions to reduce XCOM size and power consumption while increasing performance as we eye integration on spaceborne platforms.

## Conclusions

This project has successfully demonstrated the feasibility of an X-ray communication system based on NASA's MXS technology and standard amplitude modulation techniques. Guided by our previous simulations, we installed a laboratory system that successfully transmitted and received amplitude modulated X-ray signals. We have generated preliminary feasibility data, which should enable us to write strong proposals to NASA, Air Force, and other government agencies to mature the XCOM technology toward implementation in a space environment.

## Reference

1. Don M. Boroson, Bryan S. Robinson, Daniel V. Murphy, Dennis A. Burianek, Farzana Khatri, Joseph M. Kovalik, Zoran Sodnik, Donald M. Cornwell, "Overview and results of the Lunar Laser Communication Demonstration," Proc. SPIE 8971, Free-Space Laser Communication and Atmospheric Propagation XXVI, 89710S (6 March 2014); <https://doi.org/10.1117/12.2045508>
2. D. J. Israel, B. L. Edwards and J. W. Staren, "Laser Communications Relay Demonstration (LCRD) update and the path towards optical relay operations," 2017 IEEE Aerospace Conference, 2017, pp. 1-6, doi: 10.1109/AERO.2017.7943819.
3. Wenxuan Chen, Yunpeng Liu, Xiaobin Tang, Junxu Mu, and Sheng Lai, "Experimental evaluation of an OFDM-PWM-based X-ray communication system," Opt. Express 29, 3596-3608 (2021)
4. Miniaturized High-Speed Modulated X-Ray Source (MXS), NASA Datasheet. NP-2015-04-1643-HQ
5. Limin Jin, Wenbao Jia, Daqian Hei, Lei Zhao, Can Cheng, Feasibility study of the high frequency X-ray communication using selective characteristic X-rays, Optics Communications, Volume 484, 2021, 126697, <https://doi.org/10.1016/j.optcom.2020.126697>.
6. Gendreau et al., Miniaturized High-Speed Modulated X-Ray Source. US Patent 9,117,622. Aug 25, 2015.
7. Cao, L., Charge generating devices and methods of making and use thereof. US Patent 10,451,751. Oct 22, 2019.
8. Ball, C., Lavezzo, P., Cabrera, K., Nippa, D., "Development of advanced modulation techniques for spaceborne X-Ray communications," Final Report, CERF research project, 2021.

## Passive Radar Using L/S/X-Band Illuminators

### CERF 2022 Final Report

Christa McKelvey (PI), Jeff Blankenship

#### Background & Motivation:

Air Force Research Laboratory (AFRL) personnel have expressed an interest in passive radar measurements to detect moving ground targets, using signals in the L, S, and X bands. The ElectroScience Laboratory (ESL) has experience designing, integrating, and operating passive radar that exploits digital television (DTV) signals in the UHF band for airborne targets. Most recently, ESL developed two USRP-based passive radars (Figure 1), which use nearby digital television transmitters as their transmitters-of-opportunity (TOOs).

This project leverages ESL's experience with UHF passive radar to investigate the potential for development of an L/S/X-band passive radar.



(a) Passive radar on roof of ARC



(b) Passive radar on roof of ESL

*Figure 1: Outdoor components of the two OSU passive radar systems include the surveillance antenna array, the reference antenna, and the RF enclosure.*

#### Project:

As an information gathering project, three tasks were identified to learn key information about the feasibility of L/S/X-band passive radar development and operation at ESL. These were:

- 1) Perform a signal survey of the L-, S-, and X-band signals at ESL.
- 2) Develop a preliminary front-end L/S/X-band passive radar design.

Measurements were taken on the roof of the old ESL building. Figure 2 shows the location of the survey antenna relative to the edges of the building, the existing passive radar, and obstruction caused by the roof access.



Figure 3: Roof of ESL building

A wideband horn antenna covering L/S/X-bands and with an approximate 3-dB beamwidth of 50 degrees was mounted to a tripod and connected to a spectrum analyzer (Figure 5).

For each frequency segment identified, the antenna was rotated clockwise 360 degrees at a rate of approximately one revolution per minute. With the spectrum analyzer set to max hold, the azimuth sweep captured signals originating from all directions.

Because the horn antenna selected is of single polarization, the same measurements were repeated with the horn rotated by 90 degrees to capture the opposite polarization.



Figure 4: Survey equipment setup

### Results:

Of the frequency segments surveyed, there were potential transmitters-of-opportunity found in L-band and S-band, but none seen in X-band. Figures 5 through 8 show the signals found during the survey.

### L-Band

960 – 1215 MHz segment

- Center frequency (CF) near 1.09 GHz and bandwidth of approximately 4 MHz
- Potentially others with smaller bandwidth

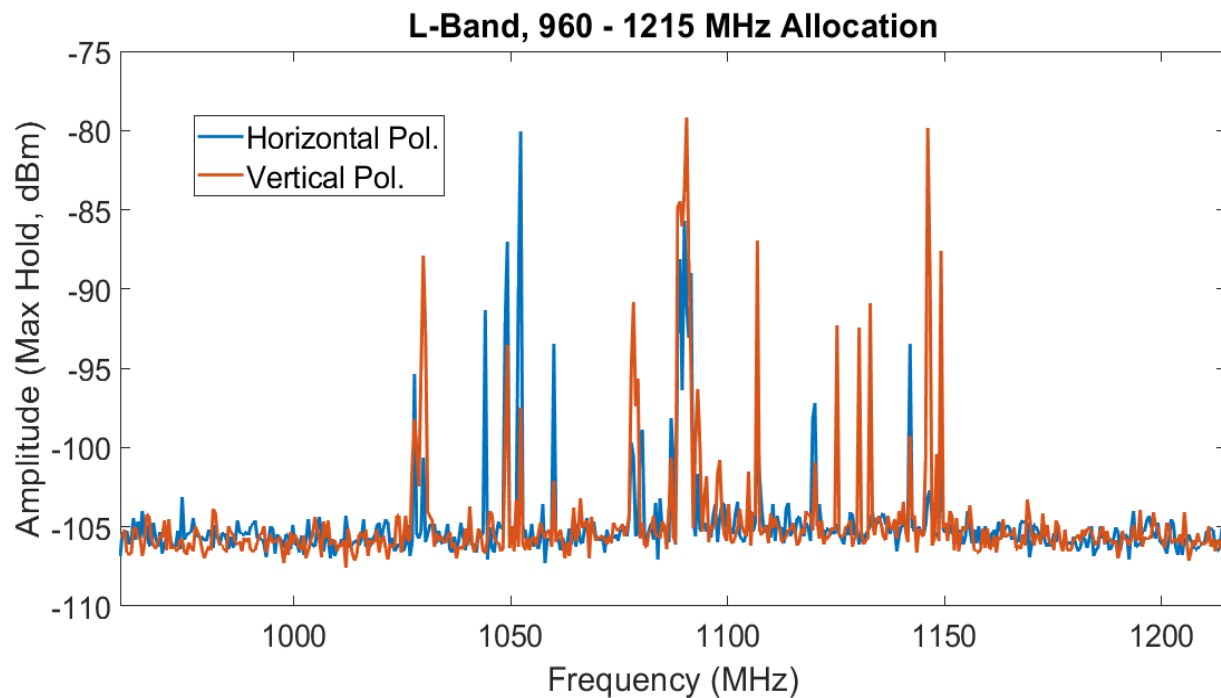


Figure 5: 960 to 1215 MHz portion of L-Band with prospective transmitters

1215 – 1390 MHz segment

- Appears to be a PM or FM signal with a CF  $\sim 1.2796$  GHz, H- and V-pol



- Similar signal lower in frequency seen only in H-pol, CF unknown

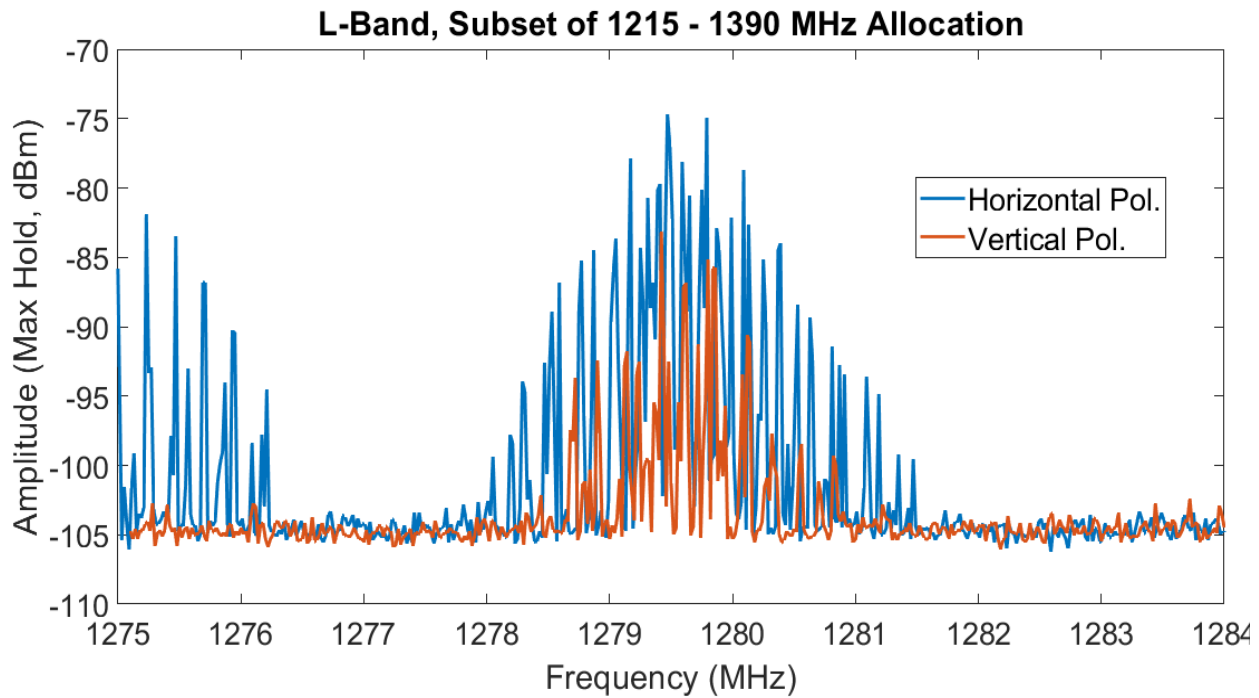


Figure 6: 1215 to 1390 MHz portion of L-Band with prospective transmitters

## S-Band

2305 - 2390 MHz

- CF ~2.32625 GHz, ~4 MHz bandwidth, V-pol
- CF ~2.33883 GHz, ~5 MHz bandwidth, V-pol
- CF ~2.355 GHz, ~10 MHz bandwidth, H-pol > V-pol

2700 – 2900 MHz

- CF ~2.77 GHz, V-pol > H-pol, PM or FM



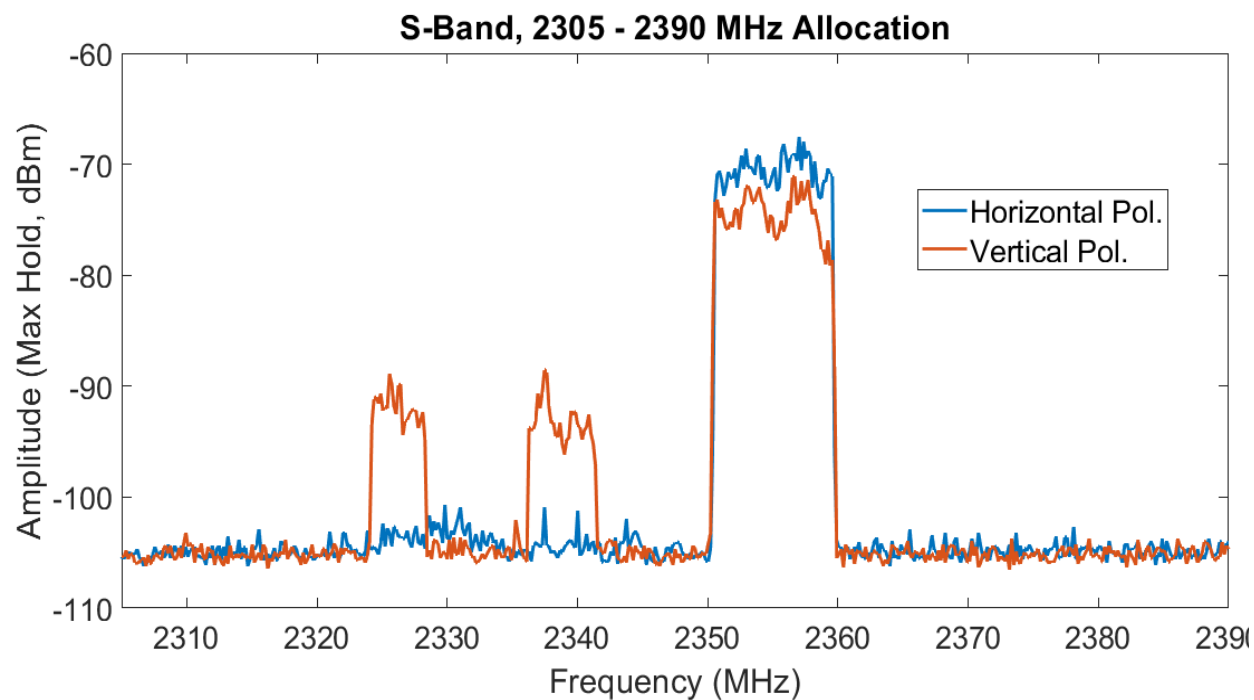


Figure 7: 2305 to 2390 MHz portion of S-Band with prospective transmitters

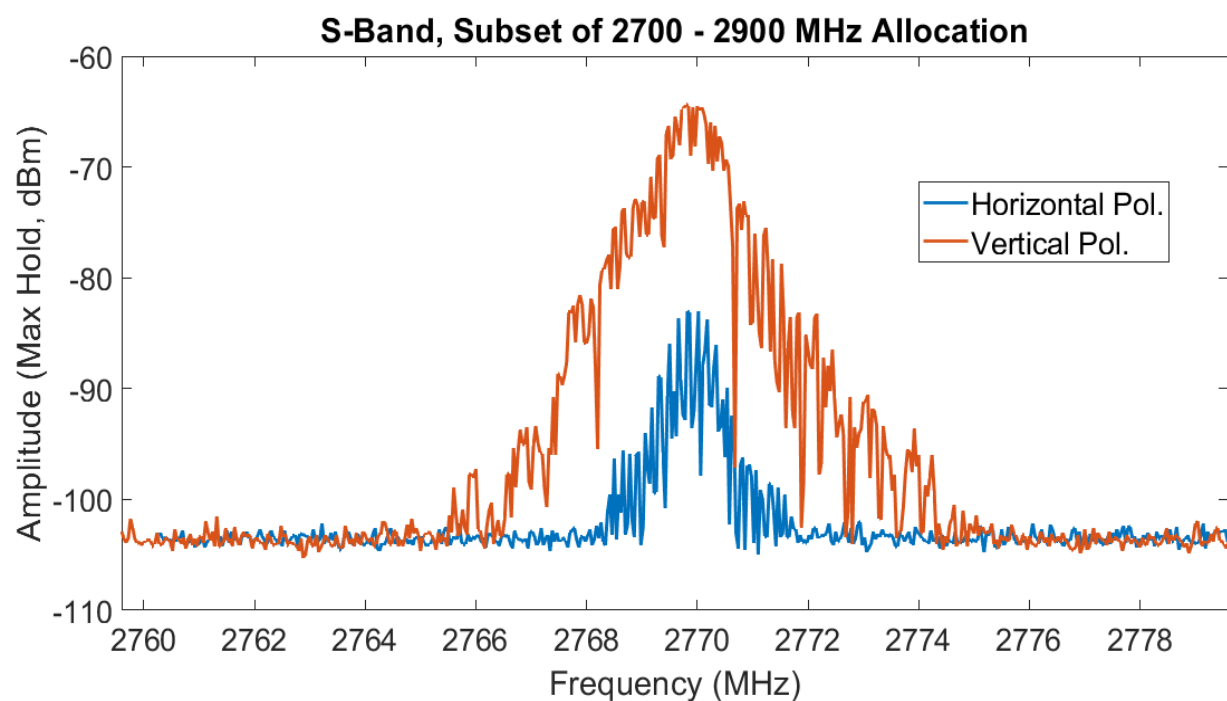


Figure 8: 2700 to 2900 MHz portion of S-Band with prospective transmitters

## Task 2: Preliminary Front-End Design

### Approach:

Starting with the DTV passive radar design, we identified what components could be repurposed for an L/S/X-band radar. With the assumption that the radar would be operated at the same location where the survey was conducted, the fact that no potential TOOs were found in X-band greatly simplifies hardware selection since the design will only need to support frequencies up to 3 GHz. Where components in the DTV radar design were not sufficient, appropriate components were selected.

### Results:

A block diagram of a preliminary L/S-band passive radar design is shown in Figure 9, with example part numbers for the RF components listed in Table 1.

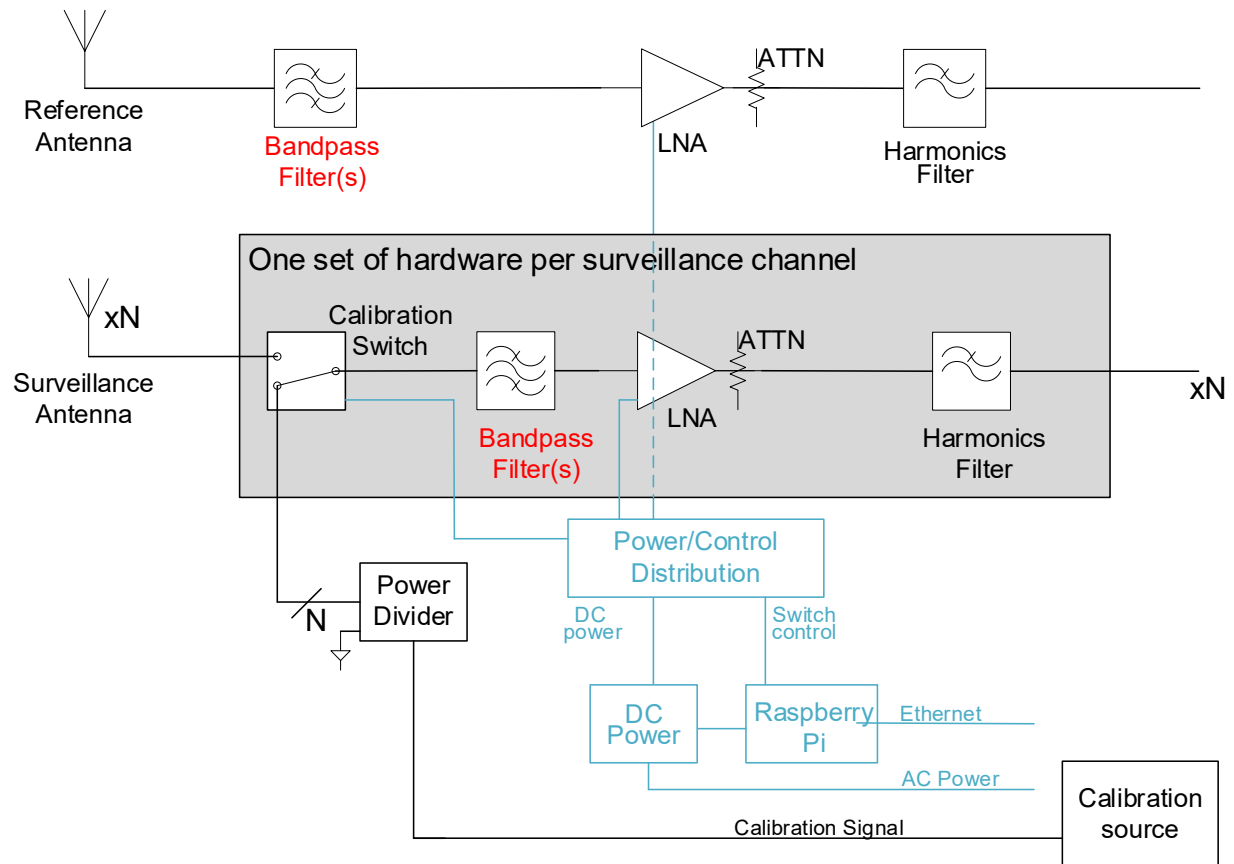


Figure 9: Passive radar block diagram

Table 1: Front-end parts for L/S-band passive radar

Quantity	Description	Manufacturer	Part Number	Freq Range
1	Calibration Source	Ettus	USRP B205MINI-I	DC - 6 GHz
1	Power divider	Mini-Circuits	ZN8PD1-53-S+	DC - 5 GHz
N	Calibration switch, SPDT	Mini-Circuits	ZX80-DR230-S+	DC - 3 GHz
N+1	LNA	Mini-Circuits	ZX60-P103LN+	DC - 3 GHz
N+1	Attenuator	Mini-Circuits	VAT+1	DC - 6 GHz
N+1	Harmonics filter	Mini-Circuits	ZLSS-A2R8G-S+	DC - 3 GHz
N+1	Bandpass filters	Mini-Circuits	ZX75BP-1062-S+	960 - 1164 MHz
		Mini-Circuits	ZX75BP-1307-S+	1215 - 1400 MHz
		TBD	custom*	2305 - 2390 MHz
		Mini-Circuits	VBF-2900+	2700 to 3100 MHz
N+1	Notch filter	Anatech	AE942N2242	925-960 MHz (GSM)
N+1	Tunable filter	Fairview Microwave	SBPF-1500-3000-05-N	1500 - 3000 MHz, tunable 5% BW
* No COTS filter was found for the desired frequency range, so may need to be custom ordered				

### Task 3: USRPs for L/S/X-band passive radar

As noted in task 2, because no X-band TOOs were observed during the survey, the radar need only support frequencies up to 3 GHz. This simplifies the backend hardware, allowing the Ettus x310 USRP with the TwinRx daughterboard, which operate up to 6 GHz, to be used directly with no additional receiver downconversion required.

Additionally, the Ettus B200mini USRP that is used in the DTV passive radar is suitable as a calibration source up to 6 GHz as well.

### Summary and notes:

This project shows that there is a potential for operation of an L/S-band passive radar located at ESL, with several prospective transmitters-of-opportunity to leverage. At the time of this study, no X-band TOOs were found. The design and parts selection for such a radar closely mimic that of the DTV passive radars that ESL operates, putting ESL in a good position to expand their passive radar capability to L- and S-band.

A challenge may be bandpass filter selection since at the time of radar installation TOO sources identified in the survey may no longer be present. With evolving technology and a demand for more civilian communication capacity, more interferers might be present in adjacent spectral allocations. Additional surveys and positive identification of signal sources would provide reassurance that the TOOs identified in this study are persistent and suitable for passive radar.

One option to investigate further is the possibility of using a filter bank in the front-end to enable on-the-fly selection of which transmitter-of-opportunity to use. This idea might also be expanded to combine the UHF and an L/S-band radar into one system.

# Discerning Target Altitude with a Passive Radar by Using Multiple DTV Transmitters

## CERF 2022 Final Report

Christa McKelvey

### Background & Motivation:

ESL recently built two USRB-based passive radar systems, installed at ESL and OSU's Aerospace Research Center (ARC) (Figure 1), for the purpose of aircraft detection and tracking. Each radar has a linear horizontal seven-element surveillance antenna array, which enables us to determine the azimuth of an airborne target along with its range (i.e. latitude-longitude localization). Since the antenna configuration limits us to 2-dimensional localization, target altitude is not able to be determined. We cannot distinguish air targets from ground targets, which results in a lot of clutter due to detection and tracking of true but unwanted targets (Figure 2 and Figure 3).



Figure 1: Passive radar at ARC showing horizontal linear surveillance array

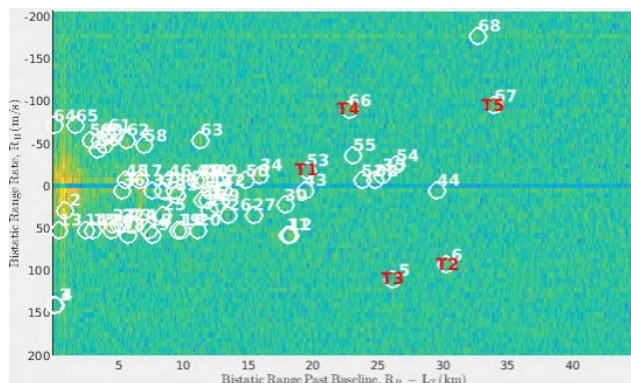


Figure 3: Range-Doppler Surface with Target Detection

This project aims to study the use of two transmitters that are separated vertically to gain information about target altitude. The ability to distinguish ground traffic from air targets using the existing configuration of the passive radar would greatly improve its performance with no impact to its hardware or software architecture.

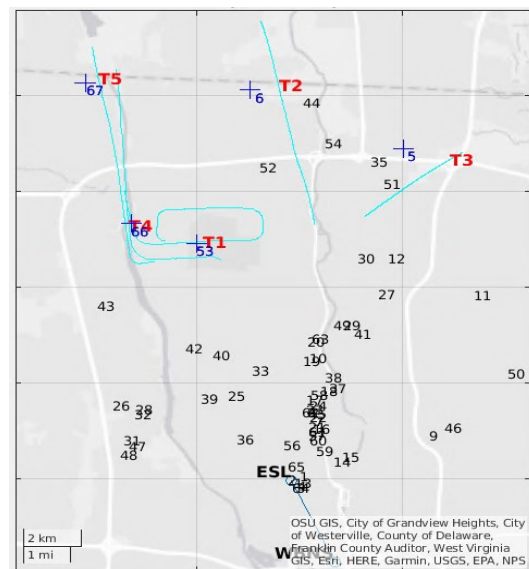


Figure 2: Map of Calculated Target Locations; with several targets presumed - but not known - to be on ground

## Approach:

Using ESL's DTV passive radar, the approach was to use two transmitters located at different elevations to simultaneously receive transmissions (Figure 4) into the 7-element horizontal array. This will potentially result in slight differences in received phase, calculated range, and calculated angle between the two transmitters, which will give insight into the altitude of the target. The greater the vertical separation, the more likely these differences would be apparent.

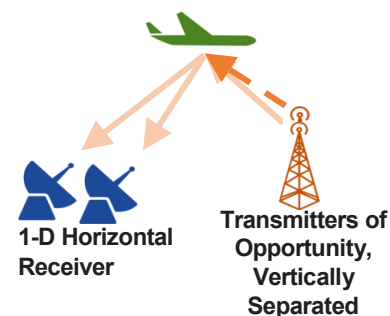


Figure 4: Two-transmitter conceptual diagram

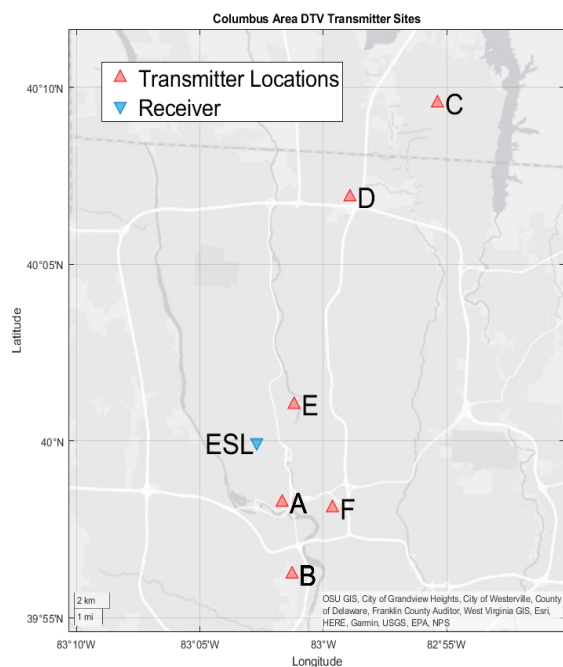


Figure 5: DTV Transmitter Sites

Transmitter pairs were selected based upon location (Figure 5), relative elevation, and spectral proximity to one another.

Transmitter criteria:

- In look direction of reference antenna (southeast of ESL)
- On same transmit tower
- Maximum possible separation in elevation
- Within the 50 MHz instantaneous bandwidth of USRP

Two pairs were chosen initially, but one transmitter in each pair performed poorly in generating a usable range-Doppler surface (RDS) (Figure 6). Notably, the two transmitters that produced inadequate results were both lower in elevation and lower in received power than the other two transmitters. This led to an extensive study on what transmitters are adequate for use with the passive radar at the ESL site.

## DTV Channel Survey and Analysis:

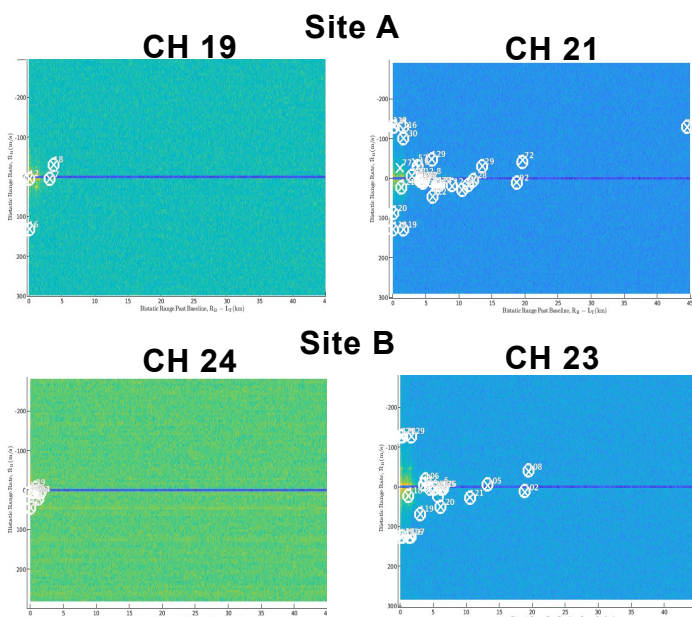


Figure 6: Range-Doppler results of the two pairs of transmit channels exploited

The information illustrated in Figure 7 is a summary of the results of investigating the usability and limitations of the DTV transmitters in the vicinity of the ESL passive radar.

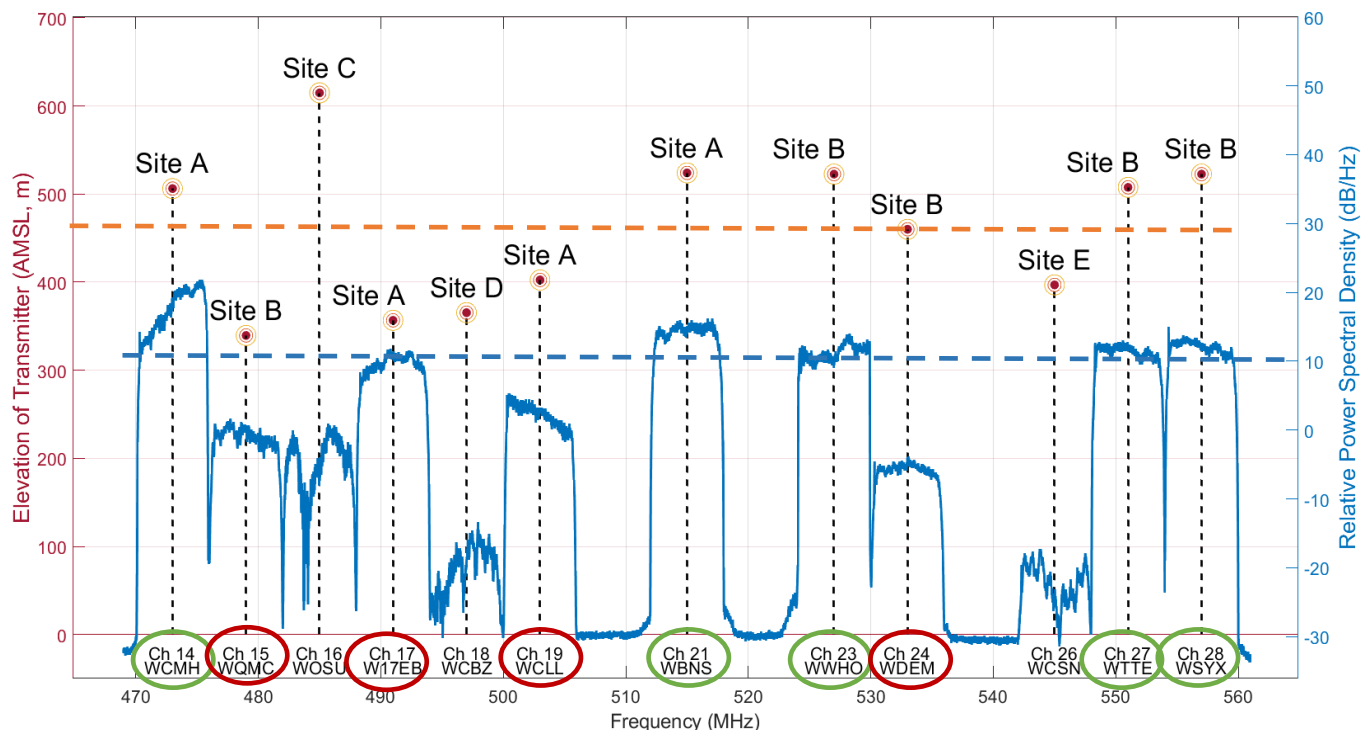


Figure 7: DTV Transmitter Spectrum and Elevations

The spectrum data in the figure was gathered using the passive radar through its reference antenna, which points southeast. For each 6 MHz channel, we see that those with a well-formed spectrum are positioned in the main beam of the antenna. The spectra with an unusual shape are lower in power and have an unusual shape due to the multipath of those signals coming from Sites C, D, and E (Figure 5).

For all of the transmitters at Sites A and B, measurements were taken to assess whether sufficient range-Doppler maps could be produced. Example range-Doppler images for each channel are located in the Appendix, with their summary shown on Figure 7. Channels that produced good results are denoted with green, while the channels with poor results are circled in red.

The dashed horizontal orange and blue lines indicate the transmitter elevation and signal levels, respectively, which seem to inform us of the likelihood of good performance. Any transmitter that lies below those lines performed poorly in this study.

An attempt was made to improve the performance of the lower power transmitters by increasing the gain settings in the USRP, but that approach did not improve the target detection results.



## Channel comparison on airborne vs. ground-based targets:

After the challenges of channel selection were better understood, channels 27 and 28 were ultimately the only pair available for comparison. However, no significant differences in were observed, possibly due to their transmitters being only 15 meters apart in elevation.

Figures 8 and 9 are the resulting target localization maps for simultaneous measurements using channels 27 and 28, respectively. Previously developed target detection code was used to perform the target localization. Figures 10 and 11 are the corresponding RDS images that produced the localization maps.

Circled in green is an airborne target – an aircraft that had recently taken off from the OSU airport – which is believed to be the only aircraft in the area at the time, based on real-time online flight tracker observations. Between the two channels, they match well in range and velocity. However, some slight difference in azimuth angle is noted.

In blue are targets that were detected in the RDS (presumably ground targets) that were mapped very closely between the two transmit channels in range, azimuth angle, and velocity.

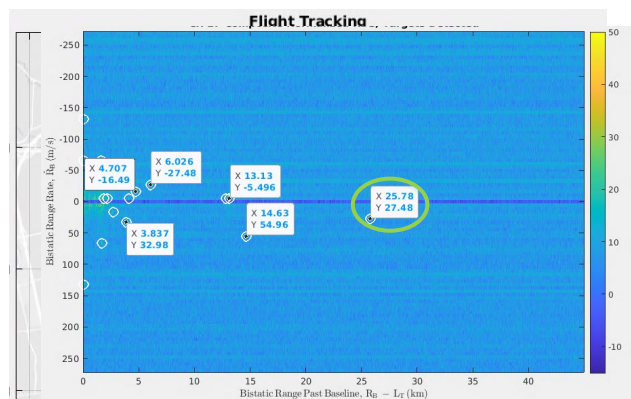


Figure 10: Channel 27 Range-Doppler Surface

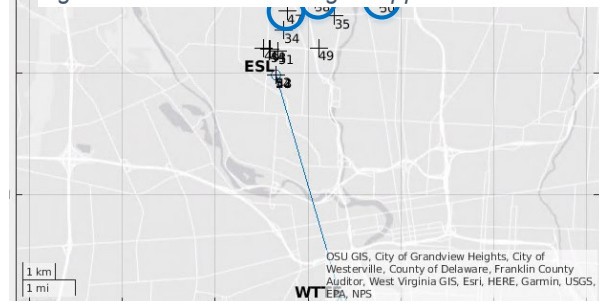


Figure 9: Channel 27 Target Localization Map

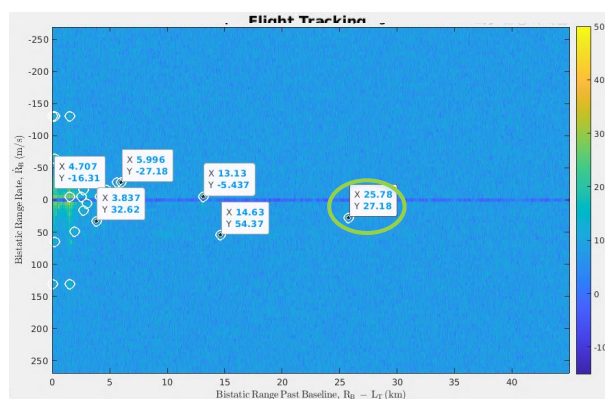


Figure 11: Channel 28 Range-Doppler Surface

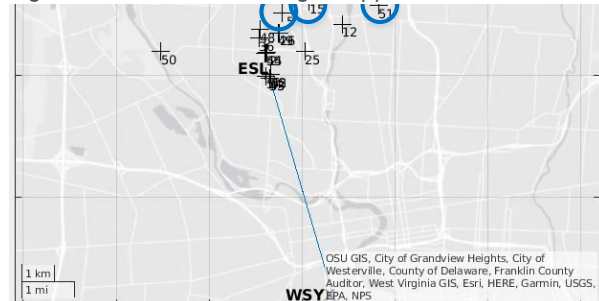


Figure 8: Channel 28 Target Localization Map



### **Conclusions and Future Work:**

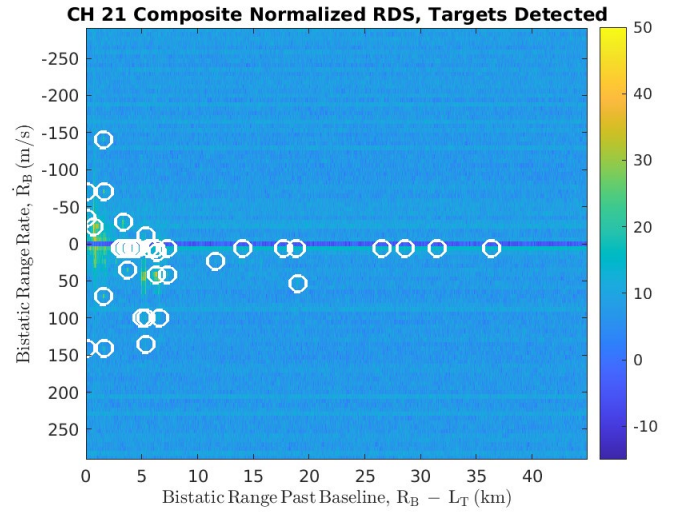
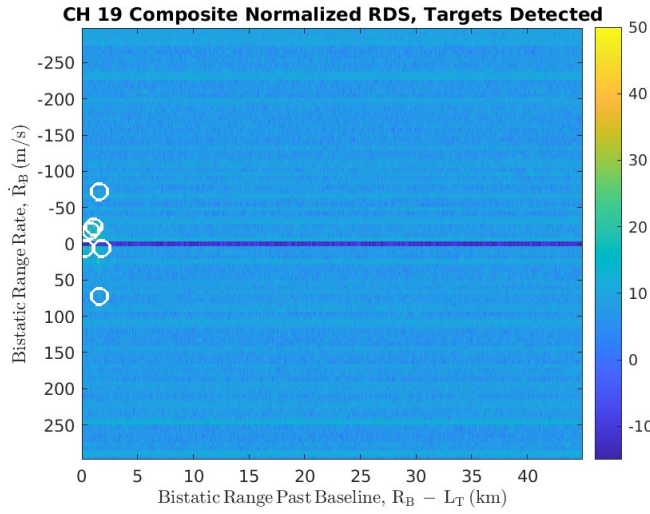
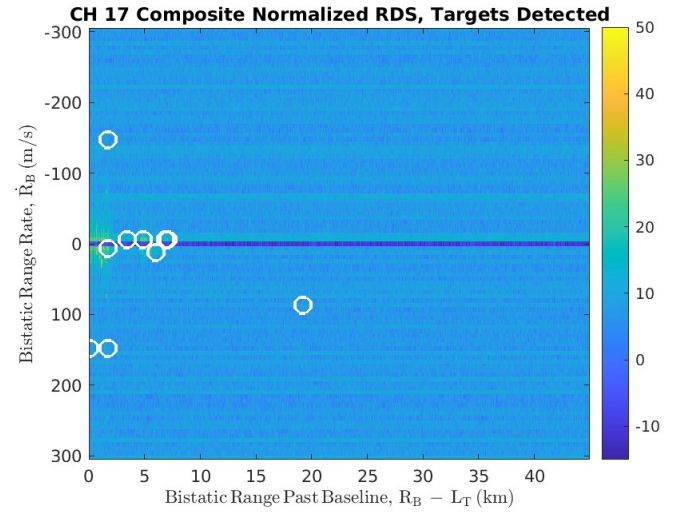
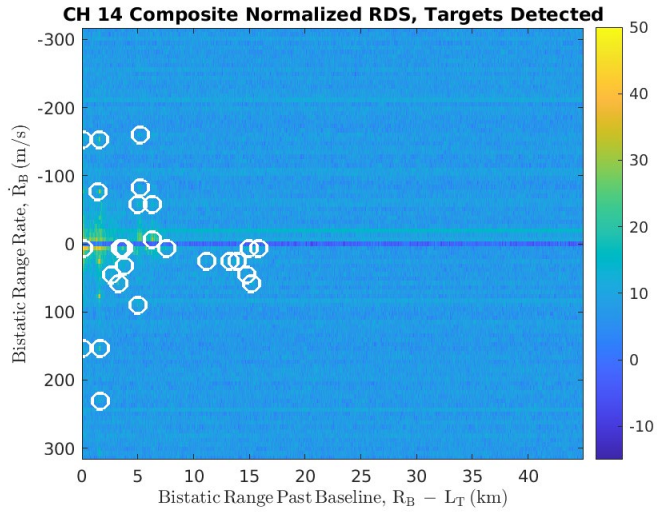
While the results of this study were inconclusive regarding whether vertically separated transmitters can help discern information about target altitude, we learned a lot about the character of ESL's passive radar.

We were able to show that two transmit channels measured simultaneously produce good agreement in target 2D localization, for both airborne and ground-based targets. The corroboration between channels for suspected ground targets indicates that they are true targets rather than due to noise or another data anomaly. More work could be done in this area, to compare the results using transmitters that are not co-located, and to investigate targets that are detected in one channel but not another.

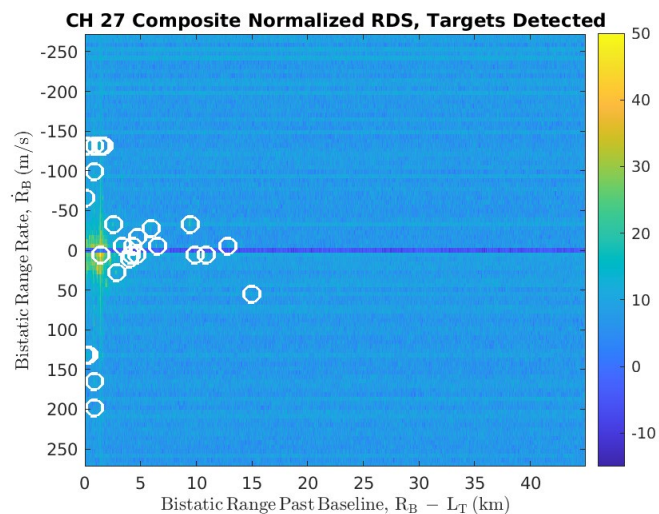
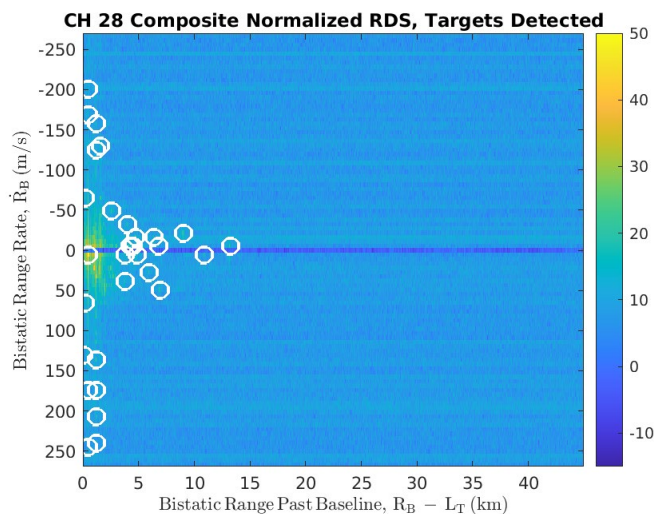
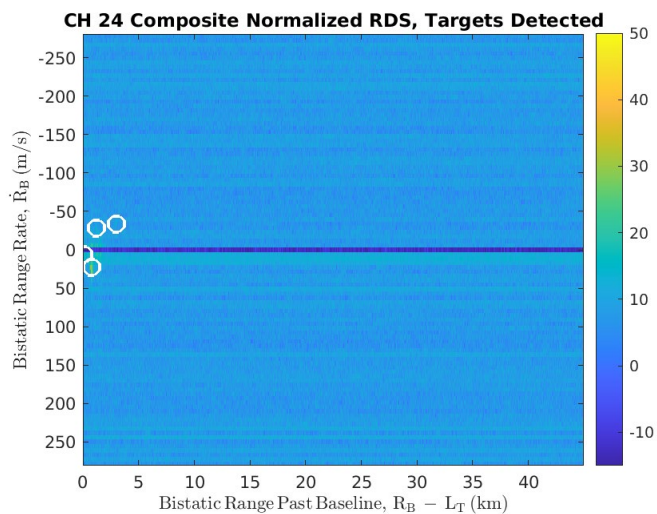
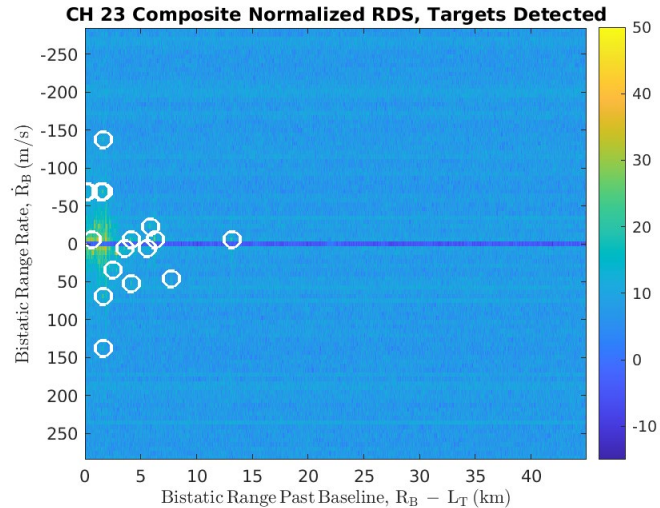
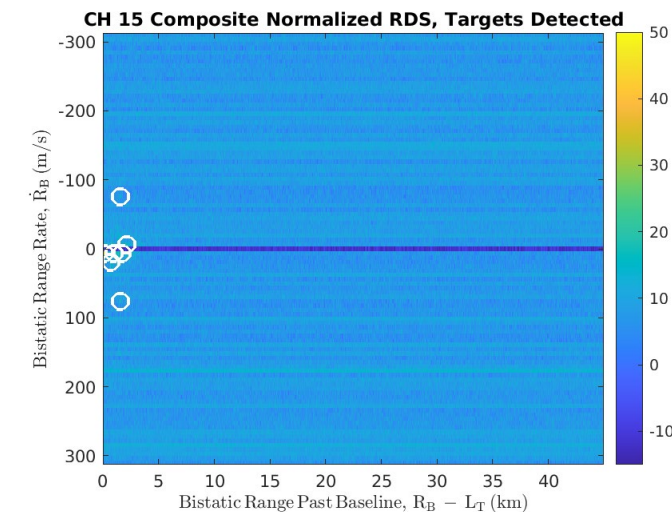
We discovered a limitation of using transmitters that are too low in power and/or too low in elevation, which results in poor target detection. Additional investigation into this phenomenon would be useful. For example, do these channels perform better with the ARC radar, where there is better line-of-sight compared to the ESL radar? Does raising the receive antenna at ESL or increasing the receive channel only help performance? If those channels are usable, a continuation of this study would be possible.

## Appendix

Range-Doppler surfaces using transmitters at Site A.



## Range-Doppler surfaces using transmitters at Site B.



# **Development of a laboratory testbed to measure gain-bandwidth product in avalanche photodiode detectors for next-generation lidar receivers**

Christopher Ball (PI), ElectroScience Laboratory  
TJ Ronningen, Sophie Mills, Electrical and Computer Engineering

## **Abstract**

ESL is currently collaborating with OSU's Dept. of Electrical and Computer Engineering (ECE) to develop short-wave infrared (SWIR) avalanche photodiode (APD) detectors to serve as receiver components for a variety of lidar applications. These APDs can detect SWIR radiation with similar signal-to-noise performance as current state-of-the-art detectors (e.g., HgCdTe) but without need for large, power-hungry cryogenic cooling systems, enabling development of future lidar systems on smaller air or space platforms, such as UAS vehicles or CubeSats. To be useful in a lidar system, these APD detectors must exhibit high bandwidth to enable accurate measurements of the time and duration of a received lidar pulse, thereby optimizing accuracy and precision of range measurements for a given target. This project has focused on the development of a testbed that can measure the gain-bandwidth product of APD detectors to ensure they meet stringent lidar system requirements. The overall testbed system design and identification of key components has been completed, and purchases of various system components have been initiated. Assembly and testing of the system are expected to be completed in early 2023, and the testbed will be used immediately for several APD development activities related to lidar technology.

## **Introduction**

Recently, ESL researchers participated on two funded proposals by Prof. Sanjay Krishna (OSU ECE) to support the development of novel infrared detector technologies to be used in scanning or imaging lidar systems operating at SWIR wavelengths. Dr. Christopher Ball (ESL) serves as a co-Investigator on a NASA Advanced Component Technology project (Bandstructure Engineered Type-II superlattice Antimonide Avalanche Photodiodes (BETA-APD) for space lidar instruments) and as Key Personnel on a project funded by the Ohio Federal Research Network (ALTITUDE: Affordable LIDAR Technologies for IntegraTion and Unmanned Deployment). For both projects, we proposed to develop lidar detectors using antimonide-based superlattices that are operated as Avalanche PhotoDiodes (APDs). These APDs can detect SWIR radiation with similar signal-to-noise performance as current state-of-the-art detectors (e.g., HgCdTe) but without need for large, power-hungry cryogenic cooling systems, enabling development of future lidar systems on smaller air or space platforms, such as UAS vehicles or CubeSats. The current research challenge is to figure out how to increase gain by increasing impact ionization within the APD, while also reducing the excess noise factor inherent in APD devices, to maximize detector sensitivity.

To be useful in a lidar system, APD detectors must exhibit sufficient bandwidth to enable accurate measurements of the time and duration of a received lidar pulse, thereby optimizing accuracy and precision of range measurements for a given target (Fig. 1). The lidar receiver bandwidth therefore must permit sufficiently accurate measurement of the pulse duration ( $t$ ) to maximize range resolution. Previous research has shown that efforts to reduce excess noise factor coincides with an increase in operating bandwidth.[1] Thus, an appropriate metric for characterizing the bandwidth performance of

an APD is the “gain-bandwidth” product.[2] Currently, OSU’s APD development team does not have an established capability to perform these measurements.

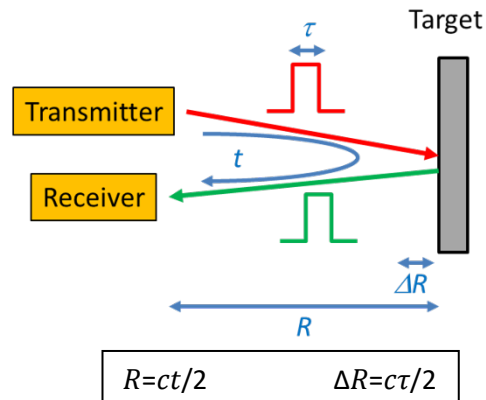


Figure 1. Accurate measurement of the range ( $R$ ) and range resolution ( $\Delta R$ ) requires precise measurement of the delay ( $t$ ) and duration ( $\tau$ ) of a received lidar pulse. Receiver bandwidth must therefore be well-characterized.

## Objectives

We propose to build up a capability that can measure gain-bandwidth product with accuracy similar to that previously described by Campbell’s group from the University of Virginia.[3] Key activities therefore include:

- Develop an approach for accurate measurement of gain-bandwidth in infrared APDs
- Design a high-level system (block diagram) that can implement the approach
- Identify specific key components that meet performance objectives
- Acquire components, assemble system, and perform diagnostic tests.

## Technical Approach

The approach summarized in the block diagram presented in Fig. 2 provides a viable capability for measuring gain-bandwidth product in infrared APDs. The basic concept is that a CW laser is modulated by an RF source (0.1-10 GHz) and then illuminates the device under test (DUT). The electronic response from the APD is then sent to a spectrum analyzer to determine the detector bandwidth. The system also includes DC bias for the APD, which can be varied to produce varying levels of gain.



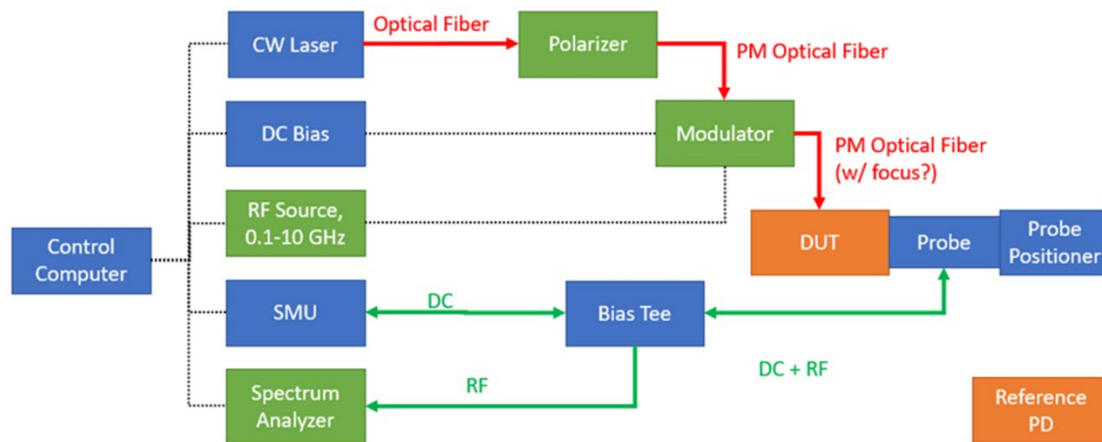


Figure 2. Block diagram of the gain-bandwidth measurement system.

The measurement sequence would include a calibration step to account for power losses separate from the DUT, followed by verification of the bandwidth of a reference photodetector. Then, the laser and probes would be aligned to the DUT. For a fixed APD bias voltage, the measurement of the gain vs. RF frequency would proceed until gain has decreased by at least an order of magnitude relative to the low frequency values. This procedure is then repeated for a series of APD bias voltages, thus enabling calculation of the gain-bandwidth product. Fig. 3 provides an example of the type of measurements acquired by this procedure.

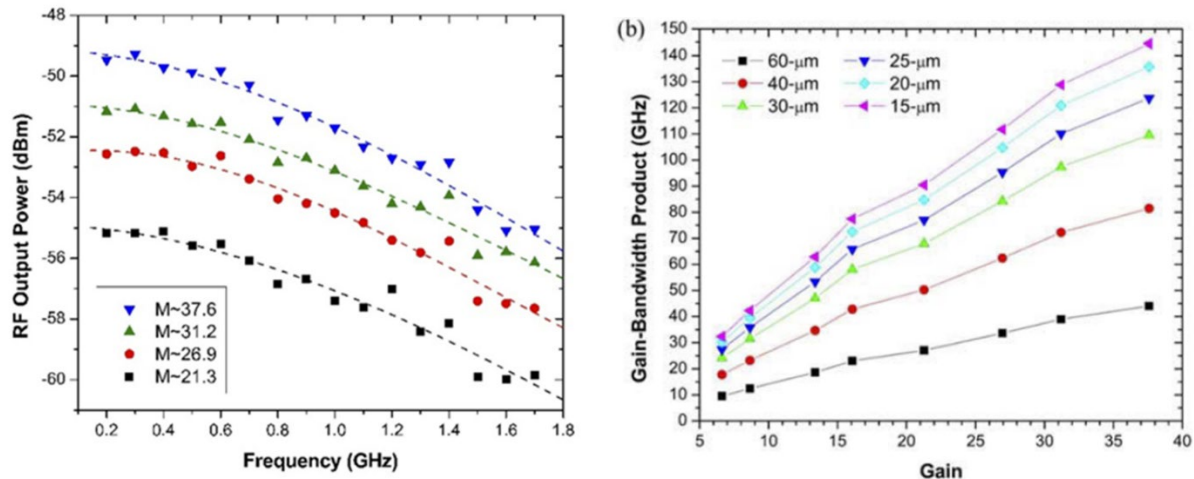


Figure 3. Example of APD response data as a function of RF modulation frequency (left) along with plot of gain-bandwidth product as a function of gain.[3]

### Component Selection

Based on the block diagram in Fig. 3, we have selected a variety of components for purchase that should meet the operational requirements necessary to provide gain-bandwidth measurements of sufficient accuracy. Table 1 summarizes the key components. Purchases of these components have been initiated and are expected to be delivered in December 2022 through January 2023.



Table 1. Key components and prices to implement the designed gain-bandwidth measurement system

Role	Component	Price	Freq. Limit	Notes
Modulated Source	OptiLab Laser Diode	\$1,295	20 GHz	New
RF Generator	Valunix	\$9,975	40 GHz	New
Spectrum Analyzer	Agilent 8566B	\$5,995	22 GHz	Used
Reference PD	ThorLabs DX20AF	\$2,200	20 GHz	New
Polarizer	n/a			
	TOTAL	\$19,456		

## Next Steps

After acquiring and assembling the gain-bandwidth test system, we plan to perform tests on recently fabricated devices to verify the accuracy of the approach. We intend to work with Prof. Campbell at U. Virginia to perform equivalent gain-bandwidth measurements on the same detector devices to ensure compatibility and consistency. Additional studies can then be conducted to understand the nature of the inherent bandwidth of the APD detector materials as well as limitations imposed by RC time constant in the fabricated devices. Once the capability has been established, it will be used immediately to support the APD development efforts funded by NASA and OFRN.

## Conclusions

This project has successfully designed a gain-bandwidth measurement system to support APD development efforts related to lidar technologies. Because the lidar receiver bandwidth is critical for accurate range and range resolution measurements, it is important to measure the fundamental bandwidth limitations imposed by the APD devices in the lidar receiver. This measurement system will be valuable for supporting current and future APD development efforts and will position OSU as a key developer of lidar receiver technologies.

## References

1. Emmons, J. Appl. Phys. 38, 3705 (1967).
2. Marshall, et al., Opt. Express 19, 23341 (2011).
3. Jones, et al., Opt. Express 29, 38939 (2021)

# Frozen-mode Enabled Photonic Sensing for Label-free Biosensors

PIs: Niru K. Nahar and Kubilay Sertel

Grad Student: Banaful Paul

## Abstract

We propose a SOI waveguide-based label-free photonic biosensors which can enable photonic sensing by taking advantage of frozen-mode. This novel approach improves the bio-sensing significantly compared to traditional approaches which utilize ring resonators, by increasing improved light-matter interaction over 600 times by taking advantage of the slow wave. This proposed device is ideal towards a next generation of integrated photonic biosensing.

## Introduction

Photonic biosensors are becoming increasingly important considering their sensitive and accurate measurement performance of biological systems and thereby advancing food and drug quality diagnostics, medical analyses, and monitoring of several environmental parameters [1, 2]. Integrating these sensors on Silicon compatible platform will be a step forward enabling the point-of-care applications making these sensing affordable and hassle free [3, 4]. The silicon-on-insulator (SOI)-technology is therefore considered as the ideal platform for integrated photonic sensors considering their monolithic integration with existing semiconductor components, i.e., lasers, detectors etc. which facilitates scalable mass production [5].

Conventional approaches for realizing SOI-based photonic biosensors can be broadly classified into either resonating or interferometric approaches [1]. Mach-Zehnder interferometers are used for interferometric structures which have high temperature stability but low sensitivity [1]. Ring resonators are the most common adaptation for implementation of resonant sensing devices. These resonators are simple to fabricate employing conventional CMOS fabrication process and have small

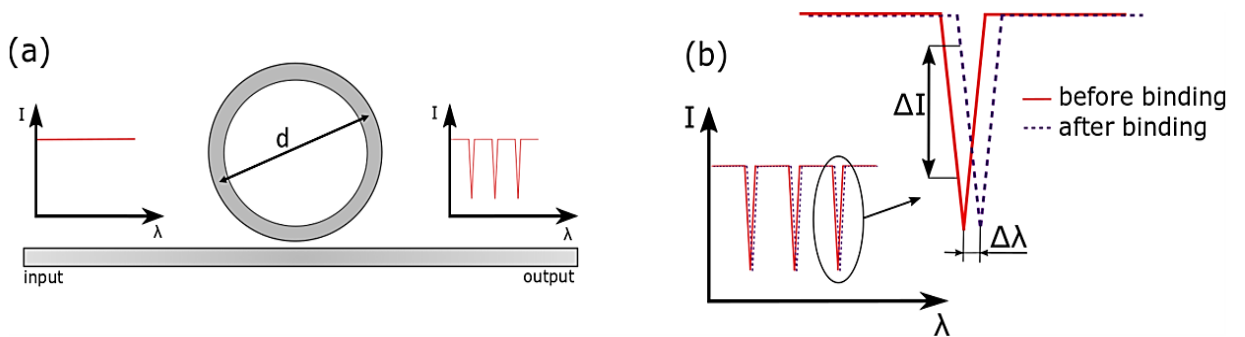


Fig. 1. (a) Schematic representation of a SOI ring resonator where according to the resonance condition, only selected wavelengths can propagate in the ring and distinct resonance peaks appear

in the output spectrum (b) Molecular binding takes place if a sample of the analyte gets in touch with the adsorbed layer on top of the silicon waveguide leading to a resonance wavelength shift  $\Delta\lambda$ . [1]

footprint and high sensitivity [6]. As depicted in Fig. 1(a), depending on the resonance condition, certain wavelengths are allowed to circulate in the ring which gives rise to resonance peaks in the output spectrum. The evanescent field which overlaps with the cladding of the waveguide, is responsible for this sensing mechanism. Therefore, change in the cladding materials (analytes in this case) will alter the resonance peaks, as shown in Fig. 1(b). Compared to rib or strip waveguide-based ring resonators, slot waveguide ones have higher sensitivity but suffer from high loss due to confinement of light in low refractive index materials. Therefore, it is imperative to devise a technique to improve the light-matter (cladding) interaction without introducing high loss.

We propose a novel idea here to solve this problem by taking advantage of a unique slow-wave photonic structure. A simple structure consisting of coupled Silicon ridge waveguides with periodic gaps is proposed here to achieve the stationary inflection point (SIP) dispersion leading to the frozen-mode. The shift of this SIP will be utilized here to detect the changes in the analytes. This can enable efficient and sensitive photonic bio-sensor on the SOI platform, making the fabrication process cheap and more streamlined.

### Proposal for Frozen-mode enabled Bio-sensor

Photonic band gaps appear in photonic waveguides due to interaction of the forward and backward propagating waves. Frequencies within the band gap are complex in nature, growing or decaying evanescently, and play a quintessential role in coupling of the modes. On the contrary, frequencies within

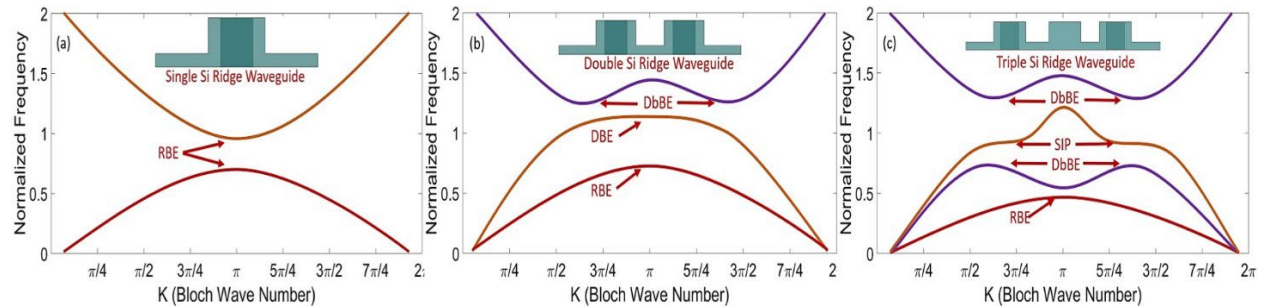


Fig. 2: Dispersion diagram of coupled Si ridge waveguides showing: (a) RBE using single ridge periodic undulations (b) DBE and DbBE with two-way coupled ridges (c) SIP with three-way coupled ridges.

the transmission band can have real wave numbers and represent the propagating modes within the waveguide. Starting from a single homogeneous dielectric waveguide, one can introduce periodic undulations (e.g., simple holes) to introduce band gaps that exhibit the conventional regular band edge (RBE), as shown in Fig. 2(a). With strongly coupled additional waveguides (e.g., two ridges that are broadside coupled), the dispersion diagram can be tuned to exhibit modes with degenerate band edge

(DBE) or double band edge (DbBE) [7] as shown in Fig. 2(b). Finally, the SIP or frozen mode, the band edge that we propose to utilize for our TTD photonic device, can be approximated by the equation  $\omega - \omega_0 \approx (k - k_0)^3$  and is shown in Fig. 2(c) due to interactions among three Si coupled ridges. After analyzing the structure with a full-wave electromagnetic solver (HFSS v19), we optimized the device with 23 unit cells. The details of the device dimensions and simulations can be found in [7]. Silicon-on-Insulator (SOI) material platform is utilized for the device fabrication where the coupled ridges are made of Silicon. As can be seen from Fig. 3 (a), a cavity is formed surrounding the ridges along which the periodic holes are perforated. This cavity will be filled with the analytes being analyzed. Our proposed device slows down light over 600 times compared to free space light which in turns increase the interaction of the electrolyte with the light 600 times, allowing significant light-matter interaction and thus increase sensitivity. The shift of the SIP with changing refractive index (R.I.) of the cladding/ analyses is depicted in Fig. 3(b).

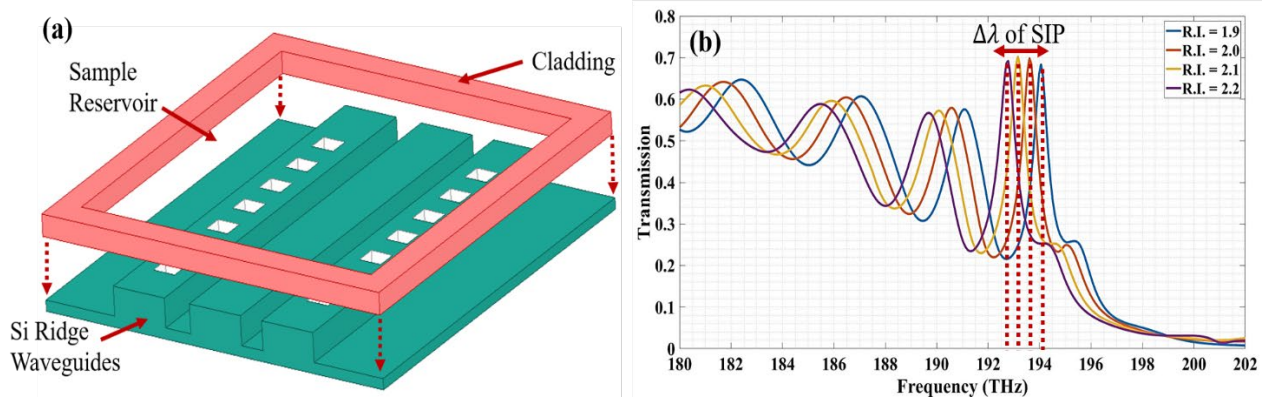


Fig. 3: (a) Frozen-mode enabled photonic sensor utilizing coupled Si ridge waveguides with a cavity to hold the analyses (b) Shift of SIP due to change of analyses of different refractive index (R.I.)

Here we present an important and practical application of this device for the detection of presence of Hemoglobin (Hb) molecules in blood sample in addition to its concentration in the measured sample. The refractive index of the blood sample varies with the Hb concentration and Fig. 4(a) from [8] depicts the experimentally measured values of blood samples for different wavelengths and different concentration of Hb. Multi-wavelength Abbe refractometer technique is utilized for measurement of samples with concentrations 65 g/l, 87 g/l, 173 g/l, and 260 g/l for several optical wavelengths. Sellmeier formula of the form in equation (1) is exploited to best fit the plotted lines in Fig. 4(a), where  $A_1$ ,  $A_2$ ,  $B_1$ , and  $B_2$  are empirical constants.

$$n^2(\lambda) = 1 + \frac{A_1 \times \lambda^2}{\lambda^2 - B_1} + \frac{A_2 \times \lambda^2}{\lambda^2 - B_2} \quad (1)$$

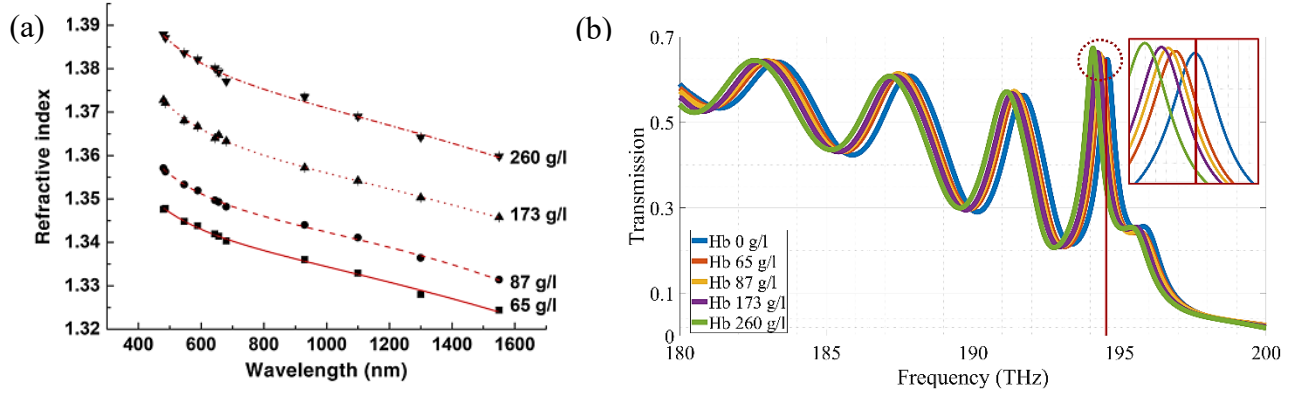


Fig. 4: (a) The dispersion curves for different Hb (g/l) solutions, measured at different optical wavelengths (b) Shift of SIP due to change of Hb concentration. The inset shows zoomed in view of this shift.

The cavity in Fig. 3(a) will be filled with blood samples with different concentrations of Hb. Then the transmission spectrum of light will be measured, reflecting the shift of SIP. This is depicted in Fig. 4(b). Fig. 4(b) depicts the shift of the SIP with varying concentration. If a vertical line is now drawn at the SIP for 0 g/l Hb concentration, the corresponding transmission at this frequency will change for different concentrations. This is depicted in the inset of Fig. 4(b). This change in transmission at about 1550 nm with variation of Hb concentration is depicted in Fig. 5. Now, to measure a solution of unknown Hb concentration, the cavity surrounding the ridges will be filled with the unknown solution. Measuring the corresponding transmission at 1550 nm for this solution will then enable to detect the concentration of Hb.

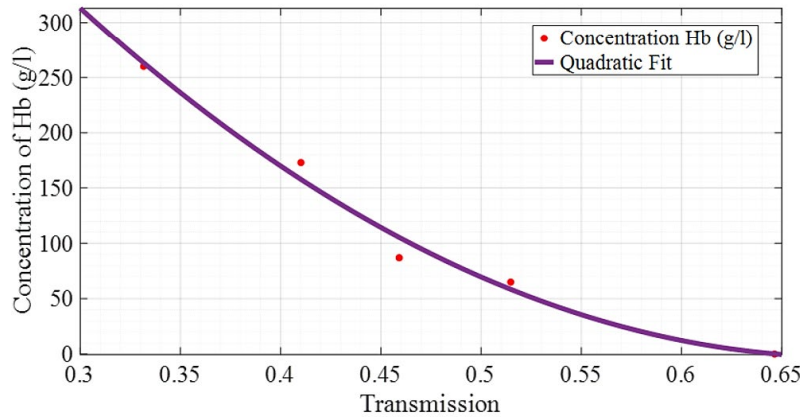


Fig. 5: Relation depicting the change in transmission at the SIP (about 1550 nm) as the concentration of Hb is varied

## Conclusion

The presented frozen-mode-enhanced label-free biosensing will be an important building block towards integrated photonic biosensing considering its sensitivity, simplicity, and compatibility with the conventional CMOS fabrication process. Here we presented the application of this sensor for detection of

concentration of Hb which could also be extended for similar applications. This novel approach could lead to low-cost, high-performance on-chip photonic sensor compatible with CMOS fabrication technology.

#### **Note**

We presented this work in Conference on Lasers and Electro-Optics, 2022.

B. Paul, K. Sertel, and N. K. Nahar, "Frozen-mode Enabled Photonic Sensing for Label-free Biosensors," in Conference on Lasers and Electro-Optics, Technical Digest Series (Optica Publishing Group, 2022), paper AM21.7

#### **REFERENCES:**

1. Steglich, P., Hülsemann, M., Dietzel, B., & Mai, A., "Optical Biosensors Based on Silicon-On-Insulator Ring Resonators: A Review," *Molecules* (Basel, Switzerland) 24(3), (2019).
2. Tom Claes, Wim Bogaerts, and Peter Bienstman, "Experimental characterization of a silicon photonic biosensor consisting of two cascaded ring resonators based on the Vernier-effect and introduction of a curve fitting method for an improved detection limit," *Opt. Express* 18, 22747-22761 (2010).
3. Boeuf, F., Cremer, S., Temporiti, E., Shaw, M., Vulliet, N., Ristoiu, D., Farcy, A., Pinguet, T., Mekis, A., Masini, G., et al., "Recent progress in silicon photonics R&D and manufacturing on 300 mm wafer platform," In *Proceedings of the Optical Fiber Communication Conference*, Los Angeles, CA, USA, 22–26 March 2015.
4. Laplatine, L., Luan, E., Cheung, K., Ratner, D.M., Dattner, Y., Chrostowski, L., "System-level integration of active silicon photonic biosensors using Fan-Out Wafer-Level-Packaging for low cost and multiplexed point-of-care diagnostic testing," *Sens. Actuators B Chem.* 2018, 273, 1610–1617.
5. Knoll, D., Lischke, S., Barth, R., Zimmermann, L., Heinemann, B., Rucker, H., Mai, C., Kroh, M., Peczek, A., Awany, A., et al., "High-performance photonic Bi-CMOS process for the fabrication of high-bandwidth electronic-photonic integrated circuits," In *Proceedings of the 2015 IEEE International Electron Devices Meeting (IEDM)*, Washington, DC, USA, 7–9 December 2015.
6. Rodriguez, G.A., Hu, S., Weiss, S.M., "Porous silicon ring resonator for compact, high sensitivity biosensing applications," *Opt. Express* 2015, 23, 7111–7119.
7. Banaful Paul, Niru K. Nahar, and Kubilay Sertel, "Frozen mode in coupled silicon ridge waveguides for optical true time delay applications," *J. Opt. Soc. Am. B* 38, 1435-1441 (2021).
8. E. N. Lazareva and V. V. Tuchin, "Measurement of refractive index of hemoglobin in the visible/NIR spectral range," *Journal of Biomedical Optics*, vol. 23, no. 3, p. 035004, 2018.



# ESL CERF 2022 – Project Final Report

## Low-Cost Passive Radar on a UAV for Flood Monitoring

Brandi N. Downs & Andrew O'Brien

### 1. Project Overview

**Summary:** Under this effort, we continued our work from a previous 2021 ESL CERF project in which we are seeking to demonstrate the feasibility of surveying flooding events using low-cost, lightweight passive radar from a small unmanned aerial vehicle (UAV). The key novelty is the use of reflected GPS signals from the water surface to detect the presence and precise height of flood waters. In this way, we use GPS signals as our illuminator of opportunity in a passive radar in a technique known as GNSS Reflectometry (GNSS-R). Last year, CERF funds were utilized to purchase a UAV (shown in the Figure below), a portable software-defined radio (SDR), two low-cost centimeter-level GNSS real-time kinematics (RTK) systems, and a Raspberry Pi4. This expended the entire amount of funds in the first CERF project. This year, student time was supported to perform extended work using the existing hardware.

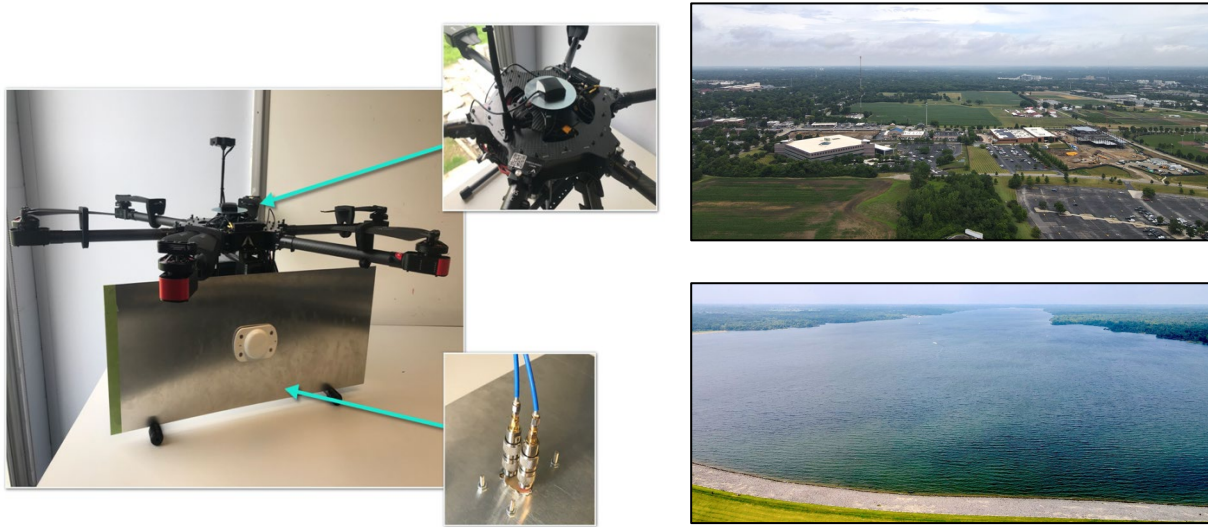
Brandi Downs is currently a graduate research associate at ESL and is in the PhD Program with an expected graduation date in 2023. Brandi will be working on this project, which could become a key component in her dissertation. Dr. Andrew O'Brien (PI) will serve as her mentor.



**Figure 1. UAV that was purchased using last year's CERF funds (left) and illustration of the the concept of using GPS reflections to measure flood waters (right)**

**Background:** Global Navigation Satellite System Reflectometry (GNSS-R) is a remote sensing technique that uses GNSS signals reflected off the Earth's surface to make measurements of geophysical properties. In this sense, the GNSS satellite is a transmitter of opportunity in a passive, bistatic radar, where a special GNSS receiver is used to track the reflected signals. Since this "radar" requires only a receiver, the remote sensing system becomes low-cost, low-power and lightweight. The significant roughness of typical ocean and land surfaces at L-band frequencies commonly results in diffusely scattered GNSS reflections. However, it has been observed that the surfaces of lakes, rivers, wetlands, and other inland water bodies are often sufficiently smooth to produce coherent reflections. Coherent reflections are of particular interest for remote sensing due to their high reflected power, fine spatial resolution, and phase information. Utilizing these reflections enables a unique capability to monitor the global surface water

distribution underneath rain, clouds, and dense vegetation. The precise nature of GNSS signals allows centimeter-scale height measurements from water surfaces.



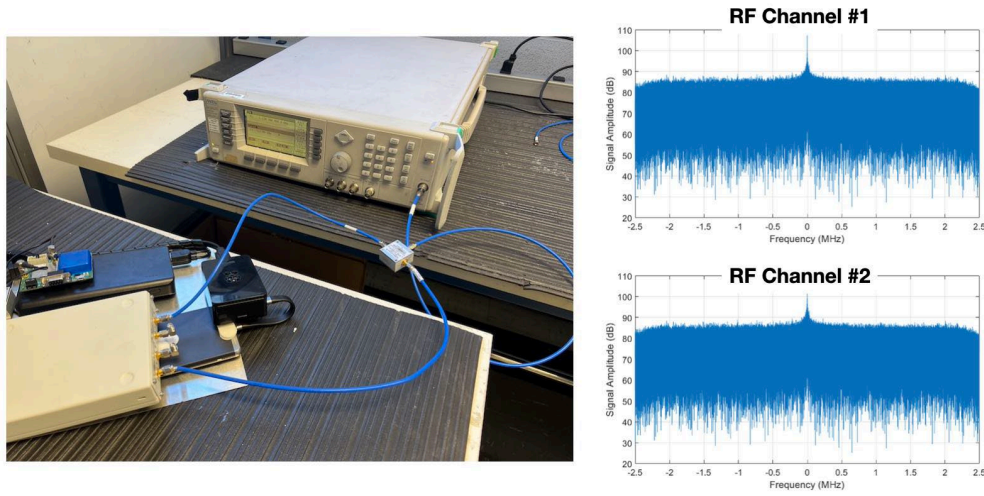
**Figure 2. Photos of the dual-polarized GNSS-R instrument antenna that is oriented to face the horizon (left), and photos captured from our UAV at 390 ft altitude (right).**

Figure 2 shows the actual instrument payload mounted on the UAV. An Ettus USRP B210 software defined radio (SDR) is used to receive 2 simultaneous, coherent channels recording 1-second snapshots of raw samples (16-bit I&Q at 5 MSPS at GNSS L1 bands). The SDR has a built-in GPS Disciplined Oscillator (GPSDO) that maintains clean time and frequency to signal post-processing. A single, dual-polarized GNSS antenna will be used to record direct and reflected GNSS signals in the SDR and separate them using polarization. The payload also contains a low-cost uBlox M8 GNSS receiver module capable of real-time kinematic (RTK) cm-level positioning. The uBlox on the UAV acts as the “rover” and communicates over its own communication antenna to a second uBlox receiver acting as a “base” nearby. A second GNSS antenna is mounted on top of the UAV and its signal is split into the uBlox receiver and the GPSDO of the SDR. The onboard computer is a Raspberry Pi 4 that runs Linux and will control the SDR data collection over USB as well as log uBlox GNSS receiver data. The photos in Figure 2 also capture the view from our UAV at its max altitude of nearly 400 ft. For reference, the first photo shows the view from above the ElectroScience Lab looking North. The second photo shows the view of Alum Creek in Northeast Columbus.

## 2. Project Results

**Calibration of the GNSS-R Payload** – Since there are two coherent SDR receiver channels that will need to be processed jointly for our application, it is necessary to do precise calibration of the RF hardware. Bench calibration was performed of the connectorized RF components and cables that are inbetween the antenna and the SDR. Additionally, the SDR was hooked up to a signal generator (Figure 3) and simple tones were injected while SDR data was collected. Data indicates that the two channels are coherent (as expected), but there are non-constant phase offsets created at each data collection. This is likely the result of each data collection being a new call the USRP data collection program that

initializes/tunes the RF front-end IC to the GPS L1 band. The unknown phase offset will need to be addressed during our experiments if the system is to be used as intended.



**Figure 3. Bench calibration of the coherence of both receiver channels in the SDR using an injected signal.**

On the UAV, we chose to utilize a single GNSS antenna that is dual-polarized and to orient it towards the horizon. A photo of the final design is shown in Figure 4. The antenna is a simple stacked patch and has a broad field of view (i.e. nearly 160 deg). A large thin aluminum groundplane is used with this type of antenna to achieve good performance.

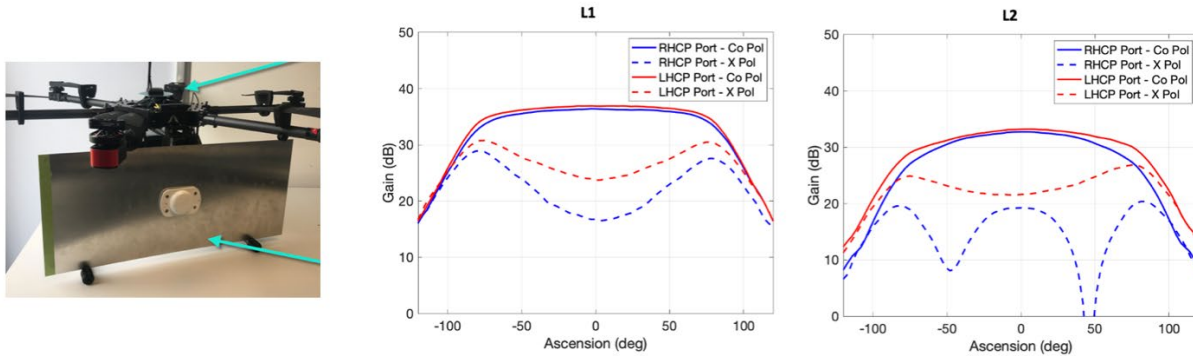


**Figure 4. Photo of the instrument payload and antenna mounted on the UAV (left) and measured antenna patterns from the ESL chamber showing the L1 and L2 GPS bands and co- and cross-pol components of both ports (right).**

The measured antenna patterns (on a large ground plane) are shown in Figure 4. Antenna has two ports (RHCP and LHCP). Each was measured separately with the other terminated with a matched load. 5V DC power was supplied to the antenna (0.16A). Measured gain includes the LNA. Boresight gain for both ports (Blue = RHCP port, Red = LHCP port), showing co-pol as solid line and cross-pol as dashed line. L1 and L2 band center frequencies, angle = 0 deg corresponds to boresight, and angle swept +/- 120 deg.

The SDR will coherently receive both ports of the antenna simultaneously. However, separation of the direct and reflected path signals over all incidence angles will require an optimal synthesis and/or decomposition of the polarization of received signals. If (1) coherence is maintained in the SDR between the non-ideal RHCP and LHCP channels coming from the antenna on the UAV and (2) we have precise antenna and RF channel calibration information, and (3) the RHCP and LHCP antenna channels are sufficiently orthogonal (which they are), then we can theoretically synthesize any polarization digitally (with a hit in SNR). This synthesis can occur at the complex delay-Doppler Map (DDM) level, not raw RF signals. Therefore, we can overcome the poor cross-pol performance of the standard UAV-observed GNSS-R scenario. Figure 5 shows an example of transforming the original co- and cross-pol patterns into the synthesized patterns in software.

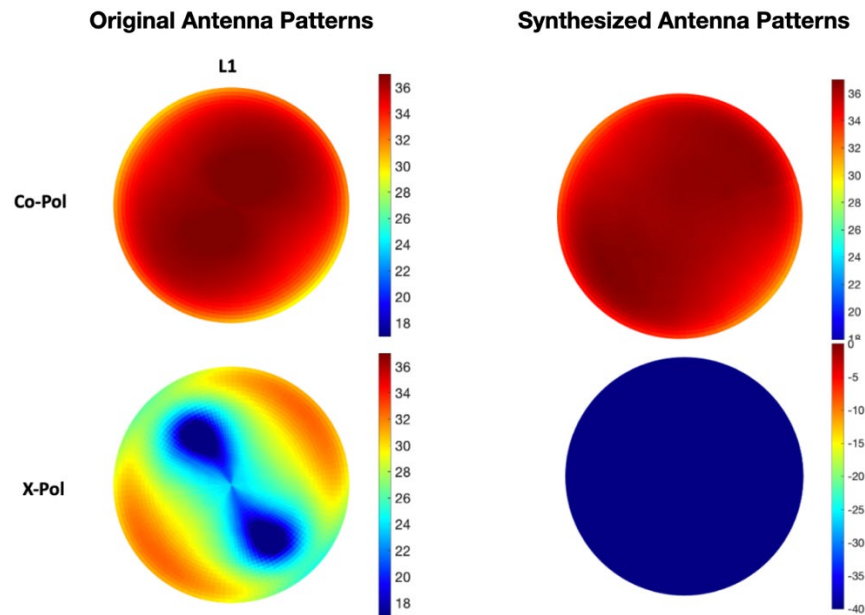


**Figure 5. Upper-hemisphere plots of GNSS antenna gain pattern showing the (left) original co- and cross-pol antenna patterns for a single port and (right) the synthesized co- and cross-pol patterns after transforming the coherent channels**

**Development of the Post-Processing Software** – While last year we focused on procuring and assembling the hardware, this year we worked to prepare the needed post-processing software. As a reminder, a hardware diagram for the GNSS-R UAV payload is shown in Figure 6. The two antenna ports are connected to RX1 and RX2 ports on the SDR. We will configure the SDR to record periodic snapshots of RF signals to memory (USB thumb drive), which we will later post-process on the ground using existing codes we have that are able to track direct and reflected GPS signals. Figure 7 shows a diagram of the post-processing software design. Timestamps from the recorded signal files are combined with GNSS receiver logs to predict the GNSS signals in view and their Doppler offsets. These are used to produce a reference signal that is cross-correlated between both channels IF signals. The delay and Doppler offsets of the reference signal are swept over a range of values to yield a delay-Doppler Map (DDM) with complex values output at 1 kHz rate. The DDMs corresponding to the RHCP direct-path channel are non-coherently integrated and a peak of the signal in delay-Doppler space is found. This is used to select the time-varying peak pixel in the original 1 kHz DDM data. The result is a 1 kHz complex I&Q time series, coherent between both

channels. This data is fed into a simple matrix transformation that mixes the components together to produce a desired polarization components that separate out the direct and reflect path components completely. The presence of clean differential phase between the direct and reflected components detects water while the amount of phase difference measures the water height.

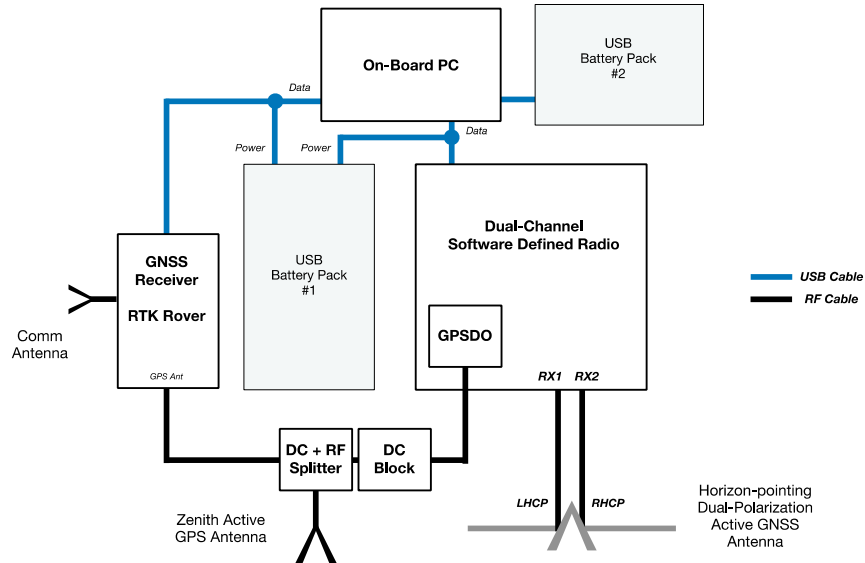


Figure 6. Diagram showing the components of the UAV GNSS-R payload (review from last year)

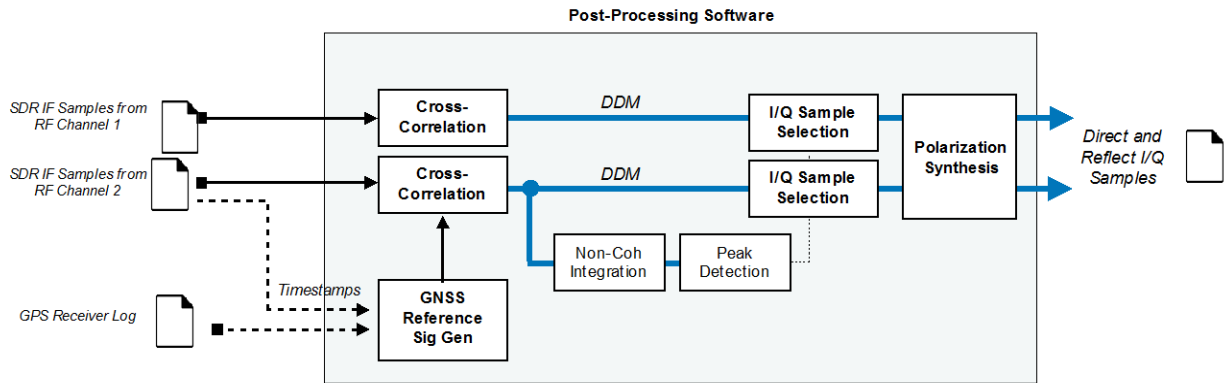
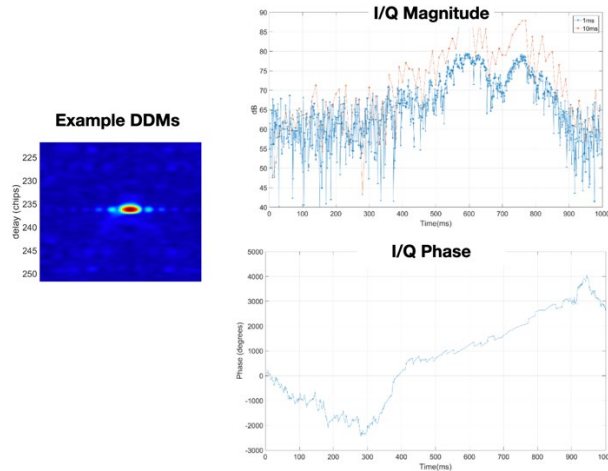


Figure 7. Diagram showing the components of the post-processing code under development to generate measurements from the recorded raw files of the UAV GNSS-R payload

A portion of this code has been reused from previous project work for NASA. This code processes raw-IF samples from a spaceborne GNSS receiver. It similarly produces high-rate complex DDM waveforms, whose peak is found and used to isolate a single delay-Doppler pixel from which magnitude and phase (I&Q) data time series is produced. Figure 8 shows an example of this code applied to real GNSS data.





**Figure 8. Example DDM produced by GNSS-R processing software from an example IF sample data signal.**

**Simulating Dynamics of Received Signals** – Prior to experiments with the hardware, it is necessary to understand when reflections will be present at incident angles of interest. This requires simulations to know what time of day GPS satellites will be in the sky at different angles and if those angles lead to reflections at angles that occur over water. A simple Matlab program was developed to simulate the GPS constellation for different dates and the surface of the Alum Creek area was mapped into delay and Doppler space to determine the presence of reflections, assuming the nominal 390 ft altitude of the UAV at the center of Dinnan Field. Figure 8 shows a few example figures from these simulations.

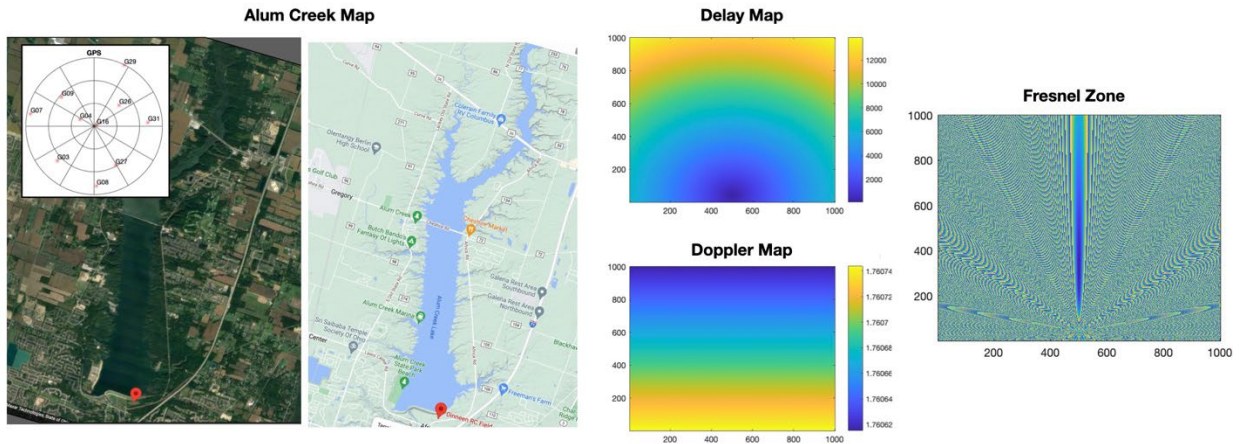


**Figure 8. Example DDM waveform produced by GNSS-R processing software from an example IF sample data signal.**

**Conclusions & Future Work:** Future work will entail more outdoor experiments now that hardware calibration and software development has progressed this year. This project will benefit our student by becoming part of her PhD dissertation and expand her research experience with the use of drones and her own passive radar hardware. The software and hardware developed in this work will likely be incorporated into future proposals in the area of GNSS and radar remote sensing.